# Role of sulfur in vibration spectra and bonding and electronic structure of GeSi surfaces and interfaces

by

Mark Christopher Hartnett


Thesis submitted for the degree of

Doctor of Philosophy

from the

Department of Physics

National University of Ireland, Cork

November 28, 2016

Supervisors: Professor Stephen Fahy

Head of Department: Professor John McInerney

Dedicated to my parents and Danielle

# Abstract

A quantum mechanical density functional theory approach was used to investigate the structural atomic configuration, vibration mode frequencies and electronic structure of surfaces and interfaces using germanium. Initially, we investigated the $H_2S$ and $H_2O$-passivated germanium surfaces. A supercell approach is used with the local density (LDA), generalized gradient (GGA) approximations and van der Waals (vdW) interactions. The frozen phonon method was used to calculate the vibrational mode frequencies of these surfaces. For both the $H_2S$ and $H_2O$-passivated surfaces, the calculated frequencies in LDA and GGA produce a SH and OH stretch mode, a SH and OH bond bending mode, a Ge-S and Ge-O stretch mode and a SH and OH wag mode. The $H_2O$ passivated surface shows other modes that are not present in the $H_2S$ passivated surface, these are the Ge-H stretch mode and the Ge-H bending mode. The differences between the functionals including vdW terms and the LDA or GGA are less than the differences between LDA and GGA for the vibrational mode frequencies. These calculated localized mode frequencies, particularly the Ge-S and Ge-O stretch modes, provide useful vibrational signatures of bonding of both sulfur and oxygen on Ge(001)-(2x1) surface, which may be compared with vibrational spectroscopy measurements. The Ge-H stretch and bending modes are characteristic in identifying the difference between the two $H_2O$ to the Ge(001)-$(2 \times 1)$ surfaces.

A bare germanium surface is bonded to a bare silicon surface to form a Ge-Si interface. As germanium has a 4% larger lattice constant than silicon this implies there are regions on the interface where the germanium and silicon match perfectly and are completely mismatched. These regions of lattice match are referred to as aligned and the regions of lattice mismatch are referred to as misaligned. The atomic structure of the GeSi aligned interface shows the original crystal structure and the projected band

structure shows no interface states in the band gap as expected. The GeSi misaligned structure forms a $(2 \times 1)$ configuration with Ge-Ge and Si-Si dimers alternating with five fold and seven fold rings. The electronic projected band structure shows many interface states in the band gap.

In order to remove the interface states that were seen in the GeSi interface, sulfur with its six valence electrons and its flexible chemical bonds is suggested to improve the interface bonding and remove such interface states. In both regions of aligned and misaligned GeSSi interfaces, we see different $(2 \times 1)$ atomic configurations respectively. The projected band structure in both alignment and misalignment cases shows interface states around the germanium and silicon interface atomic layers and also a charge density localised around the sulfur interface atoms.

Since the inclusion of sulphur at the interface did not remove electronic traps such as interface states, we suggested the use of hydrogen on the interfaces. A sulfur terminated germanium surface results in a $(1 \times 1)$ configuration with surface states present in the band gap. However, a $H_2S$ terminated germanium surface results in a $(2 \times 1)$ configuration with symmetric Ge-Ge dimers and pushes the surface states into the bulk region. This implies the presence of hydrogen results in no surface states. When we include hydrogen on our GeSSi aligned and misaligned interfaces, the atomic configuration remains the same with the hydrogen molecule in the channels and with one Ge-S bond less in the misaligned case. However, upon looking at the projected band structures, states are clearly visible in the band gap and when we investigate the charge density contour plots, interface states do exist. Therefore, the presence of hydrogen here does not influence the interfaces. We also investigated whether or not moving the hydrogen in the channels at the interface would cause a bonding of the hydrogen to either a germanium, silicon or sulfur atom. This did not happen and the hydrogen molecule always remained in the channels.

# Acknowledgements

I would like to give my warmest thanks to my supervisor Stephen Fahy for his continious encouragement, knowledge and inspiration over the past few years. I would like to thank Felipe Murphy for his discussions and expertise throughtout all of this work and also to Martin Vaughan and John Buckeridge for all the help with my programming initially. I would like to thank all the members of the Material Systems Group in Tyndall along with Mary O'Regan for helping with all my administration questions over the years. A big thank you to Dave Goulding for his help with everything.

For the extradionary amount of love, compassion, wisdom and support I thank my amazing and wonderful girlfriend Danielle. I like to thank my wonderful parents, Christy and Theresa for all the support and for listening to me. I could not have done this without you three.

Thanks to PiFAS for making this work possible.

# Publications

- M. Hartnett and S. Fahy, "Vibrational mode frequencies of $H_2S$ and $H_2O$ adsorbed on Ge(001)-($2 \times 1$) surfaces, *Applied Surface Science*, vol. 329, page 363-370, 2015.

# Conferences

- M. Hartnett and S. Fahy, "Vibrational Mode Frequencies of a $H_2S$ Passivated Ge($2 \times 1$)-(001) Surface, *Photonics Ireland (Dublin)*, 2011.

# Contents

# List of Figures

# List of Tables

CHAPTER 1

# Introduction

This theoretical study, in which we investigate various aspects of the bonding, vibrational modes and electronic structure of GeSi surfaces and interfaces, was originally stimulated by the possibilities for development of GeSi avalanche photodiodes using wafer-bonding techniques to create the GeSi interface.

Avalanche photodiodes (APD) are p-n junction photodiodies made to operate at high electric fields in order to achieve an internal gain [4]. A p-n junction is formed by joining p-type (high hole concentration) and n-type (high electron concentration) semiconductor materials. Electrons diffuse from the n-type side to the p-type side and similarly holes flow by diffusion from the p-type side to the n-type side. In a p-n junction, when the electrons and holes move to the other side of the junction, they leave behind exposed charges on dopant atom sites, which are fixed in the crystal lattice and are unable to move. On the n-type side, positive ion cores are exposed and on the p-type side, negative ion cores are exposed thus forming an electric field between the positive ion cores in the n-type material and negative ion cores in the p-type material. This region is called the depletion region since the electric field quickly sweeps free carriers out, hence the region is depleted of free carriers. A built in potential is formed at the junction due to the electric field.

APD's are strongly reverse biased photodiode [4]. In such reverse biased photodiodes, the electric field increases as the applied voltage is increased causing the kinetic

energy of the charge carriers injected into the depletion region to increase [5]. By doing so an electron (or hole) can reach an energy high enough to break a bond when colliding with lattice atoms, thus generating a new electron-hole (e-h) pair, and losing part of the energy in the process. This is known as impact ionization.

In APD's the absorption of an incident photon first produces an e-h pair. The large electric field in the depletion region causes the charges to accelerate rapidly. Such charges propagating at high velocities can give part of their energy in the valence band and excite it to the conduction band, resulting in an additional e-h pair that can in turn further accelerate and create more e-h pairs. This process leads to an avalanche multiplication of the carriers [6], [7] and [8].

APD's are widely used in the fibre-optic communications where high sensitivity is required. Recent research [9] is focusing on using silicon as the multiplication material for APD's but a major disadvantage is the optical absorption of silicon which cuts off at a wavelength of $1.1\mu$. This is too short for the optimum window required for fibre-optic communications at 1.3 or $1.5\mu$. The use of germanium [10] with its smaller bandgap energy (0.74 eV compared to 1.17 eV for silicon) overcomes this problem. While the wavelength sensitivity of the material is very important, another parameter that can have a major impact on the performance of the APD is the level of noise that is produced. The main problem with noise [11] in APD arises in the amplification of shot-noise. Shot-noise is produced due to the random quantum effects such as the random arrival of photons and thermally excited e-h pairs. Amplification of shot-noise leads to a degradation of the signal to noise ratio (SNR), which is a measure of how a signal has been corrupted by noise. SNR is proportional to what is called the excess noise factor, which is the noise due to the multiplication process and is dependent on the ratio of the e-h ionization coefficients for impact ionization. The greater this ratio the lower the excess noise factor will be. Silicon detects in the visible and near infrared, with low excess noise, while germanium will detect out into the infrared but

with high multiplication noise.

The ideal solution is to have an APD with the optical properties of germanium and the noise properties of silicon [12], thus proposing a GeSi APD seems promising. Recent experimental work demonstrates the germanium growth on epitaxial silicon layer on silicon substrates [13] and [14]. An alternative approach which avoids the epitaxial relationship and could be done with low thermal budget is direct wafer bonding [15] and [16]. However, looking at the process of wafer-bonding of the two materials, which is the pressing together of a wafer of silicon to a wafer of germanium using force to create a bond between the wafers, the interface of the two poses problems. One such problem is the 4 % mismatch in the lattice constant, which may result in a high concentration of interface traps [17] and dislocations. However, recent research by Kang *et al.* [9] has shown that careful processing and device design can minimize the impact of dislocations. The fabrication of GeSi heterojunction photodiodes are described in detail in the work by Gity *et al.* [18] and [19]. Even in an idealized picture of bonding between the materials, if the germanium and silicon lattices align well in some regions of the interface, then they will align poorly in neighbouring regions. ("Aligning regions" imply the silicon atoms lie in the same vertical plane as the germanium atoms.) We expect the regions of poor alignment may result in broken bonds and interface states, thus leading to the poor mechanical contact and electrical transmission characteristics. Thus, one of the goals of our study of the interface is to understand the (idealized) bonding of Si and Ge across a poorly aligned region of the interface. We will examine whether reconstruction of the interface can eliminate dangling bonds and avoid interface states that could be harmful to the electronic transmission across the interface.

The bare germanium surface undergoes extensive surface reconstruction, in which the surface atomic geometry differs significantly from that of the bulk [20],[21]. The Ge(001) surface reconstructs to form germanium dimers, thereby reducing the number

of dangling bonds per surface germanium atom from two to one. Locally, the surface structure of reconstructed Ge(001) is similar to that of Si(001) in that both exhibit dimer rows with similar geometrical arrangement.

Clean, idealized Si and Ge surfaces are highly reactive and are usually passivated in a controlled manner by the adsorption of species that cap the dangling bonds of the surface. Hydrogen is typically used to passivate the Si surface, giving rise to a passive reconstructed surface geometry, and hydrogen sulfide has been proposed for the passivation of Ge surfaces [22]. The possibilities for wafer bonding of two such surfaces (clean Si with $H_2S$-passivated Ge) are interesting: the two surfaces would be non-reactive and inert prior to bonding; Sulfur, with its preference for two-fold chemical coordination might provide a flexible link between the Si and Ge surfaces, both in well-aligned and poorly aligned regions, and molecular H, desorbed from the initial Si and Ge surfaces during the formation of bonds in the interface, could provide an atom that would be both relatively mobile within the interface and capable of passivating dangling bonds and their associated interface states. This thesis will examine this scenario in detail, calculating equilibrium bonding geometries for interfaces formed from clean Si and HS-terminated and S-terminated Ge. We will also explore the interface electronic structure, to understand if the above, chemically plausible scenario might be realized in practice. We will also examine the vibrational properties of the HS-terminated Ge surface, as infra-red vibrational spectroscopy of adsorbed species at surfaces [23] can be used as a probe of the condition of the surface prior to wafer bonding.

Termination of the Ge(001) surface by $H_2S$ has been suggested [20] in order to electrically passivate the surface. Sulfur is an atom with flexible chemical bonds preferring a two-fold coordinated geometry and thus is expected to make two bonds with the Ge(001)-$(2 \times 1)$ surface. An experimental study [22] of a Ge(001) surface exposed to $H_2S$ in the gas phase showed 1 monolayer of sulfur coverage with $(2 \times 1)$ surface

reconstruction. The amount of sulfur on the germanium surface and the observed periodicity is explained by formation of disulfide bridges between Ge-Ge dimers on the surface. A first-principles molecular dynamics study [22] confirmed that the $(2 \times 1)$ symmetry is preserved after adsorption of the $H_2S$ molecules on the Ge(001)-$(2 \times 1)$ surface and also predicts formation of (S-H)-(S-H) inter germanium dimer bridges i.e. disulfide bridges interacting via hydrogen bonding. The computed energy band gap of this atomic configuration is shown to be free of surface states, a very important finding for the potential application of germanium in future high performance integrated circuits [24], [25] and [26]. For comparison, using elemental sulfur the surface reconstruction is a $(1 \times 1)$ structure and the computed density of states clearly shows a state in the germanium energy band gap [27]. This surface state is attributed to a lone pair $3p_z$ orbital on the sulfur atom. $H_2S$ treatment of the surface results in it being electrically passivated with the lone pair $3p_z$ orbital on sulfur atoms being pushed into the valence bands of the $H_2S$ passivated surface [22].

Considering the bonding of Si(001) to a S-terminated Ge(001) or $H_2S$-terminated Ge(001) might be a promising approach to forming a strong, electrically passivated wafer-bonded GeSi interface. The flexibility of S bonds may allow the S-H sandwich at the interface to adjust its bonding both in the interface regions where the silicon and germanium lattices align and misalign.

This work will apply first principles electronic structure theory methods to calculate the structural and vibrational characteristics of a $H_2S$ and $H_2O$-terminated germanium surface. Vibrational mode frequencies will be calculated for the germanium, sulfur and hydrogen atoms at the surface. This will be used as the signature of particular bonding geometries which can be compared to infrared spectroscopy results. We will investigate the GeSi interface in regions where the germanium and silicon lattice align and misalign across the interface, along with the relaxed atomic positions. Sulfur and $H_2S$ will be sandwiched between the germanium silicon interface and the

interface will be investigated. The calculation of the electronic band structure will be determined to see whether the sulfur or $H_2S$ mediated bonding would be effective in the removal of interface electronic trap states i.e. interface states lying in the semiconductor gap.

In Chapter 2 of this thesis, we review the methods used to calculate vibrational mode frequencies and projected band structures in germanium and silicon. These methods of Density Functional Theory (DFT) allow us in principle to map a many body interacting electron gas problem into a single particle moving in an effective potential. In reviewing electronic structure methods, we also discuss structural relaxation, the use of plane-waves to represent the single-particle eigenstates that arise in the DFT formalism and the associated use of pseudopotentials to represent the electron-ion interaction, and the form of various, approximate exchange-correlation potentials that will be used in our calculations. The harmonic approximation and dynamical matrix are the ingredients for determining the vibrational mode frequencies using the frozen-phonon method. Band structure calculations around certain paths in the Brillouin zone are described here also to derive the 2D projected surface and interface band structures.

In Chapter 3, we begin our study by testing the theoretical methods described in Chapter 3 against already known theoretical results in the published literature. Our test is a density functional theory approach of a germanium surface. A surface calculation for Ge(001) was done, to reproduce the Ge(001)-$(2 \times 1)$ surface reconstruction using the local density approximation (LDA). Here we show the surface reconstructs to form asymmetric dimers that are arranged in rows, while in the electronic structure of this surface, two dangling-bond bands occur within the energy region of the fundamental gap.

After the theoretical methods have been tested and resulted in good agreement with the published literature, Chapter 4 is the beginning of our study. Chapter 4 looks

at the vibrational mode frequencies of $H_2S$ and $H_2O$-terminated Ge(001)-$(2 \times 1)$ surfaces. As both $H_2S$ and $H_2O$-terminated Ge(001)-$(2 \times 1)$ surfaces remove the electronic states at the surface, and having confirmed the presence and bonding of $H_2S$ and $H_2O$ on the Ge(001) surface, a calculation of the vibrational mode frequencies may provide a useful signature of particular bonding geometries, which can be detected by infrared spectroscopy. Using our first principles, density functional theory, supercell approach, the vibrational mode frequencies are obtained using the frozen-phonon method, which involves the calculation of the structural energy and atomic forces as functions of atomic displacement from equilibrium using different exchange-correlation functionals. This allows a dynamical matrix to be obtained. Diagonalization of the dynamical matrix gives the vibrational mode frequencies and corresponding atomic motions for the $H_2S$ and $H_2O$ adsorbed on a Ge(001)-(2x1) surface. These vibrational mode frequencies can then be compared to those of the isolated molecules. We also report the various bond lengths at the surface, along with the bond breaking energies of both H and SH on the $H_2S$-terminated Ge(001) surface and H and OH on the $H_2O$-terminated Ge(001) surface.

The GeSi interface is presented in Chapter 5. Due to the lattice constant of germanium being 4% greater than that of silicon, we investigate the regions where the lattice of germanium align with silicon and also the regions of misalignment. We calculate the relaxed geometries of both regions. From our structural relaxation calculations, strain of the lattices is an important factor and we include a full analysis of the interfaces with strain. We use self-consistent calculations to determine the band lineups of the germanium and silicon band structures and we produce the projected band structure plots to see if interface states exist in the band gap.

In Chapter 6 we investigate the bonding and electronic states of interfaces formed from Si and SH-terminated Ge surface. As we initially expected that interface states may exist in the misaligned GeSi interface, we propose the use of both sulfur and

$H_2S$ to remove such interface states. We investigate the regions of alignment and misalignment with the presence of sulfur and $H_2S$ sandwiched between the GeSi interface, providing structural relaxations, bond lengths at the interface, along with the corresponding electronic structure such as band lineups and projected band structures. Here in all the interfaces studied, interface states do exist in the band gap, thus providing the evidence that a GeSi clean interface is electronically more suitable than the interface involving HS.

CHAPTER 2

# Electronic Structure Methods

In this chapter, we review the theoretical approaches used in first-principles calculations to solve the many-body problem. The starting point is the Hamiltonian for a system of electrons and nuclei,

$$\hat{H} = -\frac{\hbar^2}{2m_e}\sum_i \nabla_i^2 - \sum_{i,I}\frac{Z_I e^2}{|\mathbf{r_i}-\mathbf{R_I}|} + \frac{1}{2}\sum_{i\neq j}\frac{e^2}{|\mathbf{r_i}-\mathbf{r_j}|} - \sum_I \frac{\hbar^2}{2M_I}\nabla_I^2 + \frac{1}{2}\sum_{I\neq J}\frac{Z_I Z_J e^2}{\mathbf{R_I}-\mathbf{R_J}}, \quad (2.1)$$

where the coordinates $\mathbf{r_i}$, mass $m_e$ and charge $e$ represent the electrons, and the nuclei are denoted by the coordinates $\mathbf{R_I}$, mass $M_I$ and charge $eZ_I$. The first term in the Hamiltonian is the electron kinetic energy operator, the second term is the electron-nuclei interaction and the third term is the electron-electron interaction. The last two terms represent the nuclear kinetic energy and the nuclei-nuclei interaction respectively. The only term that is considered small in the Hamiltonian is the one with the inverse mass of nuclei $\frac{1}{M_I}$. Setting the mass of the nuclei to be infinitely heavier than the electrons then this kinetic energy of the nuclei can be ignored. This is more commonly known as the Born-Oppenheimer or adiabatic approximation [28]. The interaction of the nuclei with one another does contribute to the total energy of the system but is not relevant to the problem of describing the electrons. Thus the Hamiltonian reduces to

$$\hat{H} = \hat{T} + \hat{V}_{ext} + \hat{V}_{int}. \quad (2.2)$$

If we adopt Hartree atomic units $\hbar = m_e = e = \frac{1}{4\pi\varepsilon_0} = 1$, then the terms may be written in the simplest form. The kinetic energy operator for the electrons $\hat{T}$ is

$$\hat{T} = -\frac{1}{2}\sum_i \nabla_i^2, \tag{2.3}$$

$\hat{V}_{ext}$ is the fixed external potential acting on the electrons due to the nuclei

$$\hat{V}_{ext} = -\sum_{i,I} \frac{Z_I}{|\mathbf{r_i} - \mathbf{R_I}|}, \tag{2.4}$$

and $\hat{V}_{int}$ is the electron-electron interaction

$$\hat{V}_{int} = \frac{1}{2}\sum_{i \neq j} \frac{1}{|\mathbf{r_i} - \mathbf{r_j}|}. \tag{2.5}$$

The Hamiltonian must satisfy the time-independent Schrödinger equation

$$\hat{H}\,|\Psi\rangle = E\,|\Psi\rangle\,, \tag{2.6}$$

where $E$ is the energy eigenvalue of the many-body wavefunction for the electrons $\Psi = \Psi(\mathbf{r_i})$, that depends on the position of the electrons and their spin (both included in the coordinate $\mathbf{r_i}$). There are many sophisticated methods for solving the many-body Schrödinger equation based upon the expansion of the wavefunction. However, calculating the electronic density is a far less demanding problem computationally. Density functional theory (DFT) provides [29] a framework that uses the electronic charge density as the principal variable, which can be used to calculate the ground state properties of the system. This chapter describes the basis of DFT, and the way it is used to solve the problem for periodic crystals using plane waves and pseudopotentials. An introduction to structural relaxations and exchange-correlation functionals is also given, as well as theory behind the frozen phonon method and projected band structure calculations.

## 2.1 Density Functional Theory

Density functional theory (DFT) allows one to map a many-body interacting electron system onto a single particle moving in an effective potential problem. This theory was put on a firm theoretical footing by the two Hohenberg-Kohn [30] theorems:

- Theorem I: For any system of interacting particles in an external potential $V_{ext}(\mathbf{r})$, the potential $V_{ext}(\mathbf{r})$ is uniquely determined by the ground state particle density $n_0(\mathbf{r})$, except for a constant.

- Theorem II: For any external potential $V_{ext}(\mathbf{r})$, there exists a universal functional for the energy $E[n]$ in terms of the density $n(\mathbf{r})$. For any particular $V_{ext}(\mathbf{r})$, the exact ground state energy of the system is the global minimum value of this functional.

A more general alternative formulation of these theorems has been given by Levy [31, 32, 33] and Lieb [34, 35, 36].

Since all properties such as kinetic energy, are uniquely determined if the density $n(\mathbf{r})$ is specified then each such property can be viewed as a functional of $n(\mathbf{r})$. The total energy functional is

$$E_{HK}[n] = T[n] + E_{int}[n] + \int d^3r\, V_{ext}(\mathbf{r})n(\mathbf{r}) + E_{II}, \tag{2.7}$$

where $E_{II}$ is the nuclei interaction energy. We define the functional $F_{HK}[n]$ as all internal energies of the interacting electron system

$$F_{HK}[n] = T[n] + E_{int}[n], \tag{2.8}$$

which must be universal by construction as the kinetic energy and interaction energy of particles are functionals only of density.

From the Hohenberg-Kohn theorems, all properties of the system can be determined from the ground state density and the functional $E[n]$ determines the ground state energy and density. However, we are still faced with the fact that no method has been given to find the functional other than the original definition in terms of many-body wave-functions. An approach was proposed by Kohn and Sham [37] to replace the difficult interacting many-body problem obeying the Hamiltonian (see Eq. 3.1 in [29]) with an auxiliary problem that can be more easily solved. They assume that the ground state density of the original interacting system is equal to that of some chosen non-interacting system. This leads to the independent-particle equations for such a non-interacting system which can be considered to be exactly soluble with all the difficult many-body terms incorporated into an exchange-correlation functional of the density. Solving such equations gives the ground state density and energy of the original interacting system bounded by the accuracy limited to the exchange-correlation functional approximation.

The approach of Kohn and Sham is based upon two assumptions:

- 1. The exact ground state density can be represented by the ground state density of an auxiliary system of non-interacting particles
- 2. The auxiliary Hamiltonian is chosen to have the usual kinetic energy operator and an effective local potential $V_{eff}(\mathbf{r})$ acting on an electron at $\mathbf{r}$

The auxiliary Hamiltonian for this non-interacting system is

$$\hat{H}_{aux} = -\frac{1}{2}\nabla^2 + V_s(\mathbf{r}), \tag{2.9}$$

where $V_s$ is the effective one particle potential. The single particle orbitals $\psi_i$ satisfy

$$\hat{H}_{aux}\psi_i(\mathbf{r}) = \varepsilon_i\psi_i(\mathbf{r}), \tag{2.10}$$

and the density

$$n(\mathbf{r}) = \sum_{i=1}^{N} |\psi_i(\mathbf{r})|^2 , \tag{2.11}$$

where $\varepsilon_i$ are the Kohn-Sham energy eigenvalues (in order of increasing energy) and $N$ is the total number of electrons. The non-interacting kinetic energy is given by

$$T_s = \frac{1}{2}\sum_{i=1}^{N} \langle \psi_i | \nabla^2 | \psi_i \rangle = \frac{1}{2}\sum_{i=1}^{N} \int d^3 r \, |\nabla \psi_i(\mathbf{r})|^2 . \tag{2.12}$$

We define the classical Coulomb interaction energy of the electron density $n(\mathbf{r})$ interacting with itself

$$E_{Hartree}[n] = \frac{1}{2}\int d^3 r \, d^3 r' \frac{n(\mathbf{r}) n(\mathbf{r}')}{|\mathbf{r} - \mathbf{r}'|}. \tag{2.13}$$

The Kohn-Sham approach is to rewrite the total energy functional of an interacting system in the form

$$E_{KS}[n] = T_S[n] + \int d^3 r V_{ext}(\mathbf{r}) n(\mathbf{r}) + E_{Hartree}[n] + E_{II} + E_{XC}[n], \tag{2.14}$$

where here $V_{ext}$ is the external potential due to the nuclei, $E_{II}$ is the interaction between nuclei and all the many-body effects of exchange and correlation are grouped into the exchange-correlation energy $E_{XC}$. Comparing the Hohenberg-Kohn and Kohn-Sham expressions for the total energy, the exchange-correlation can be written as

$$E_{XC}[n] = \langle \hat{T} \rangle - T_S[n] + \langle \hat{V}_{int} \rangle - E_{Hartree}[n], \tag{2.15}$$

which shows that $E_{XC}$ is the difference of the kinetic and internal interaction energies of the interacting many-body problem from those of the independent-particle system

with the electron-electron interaction replaced by the Hartree energy. Thus, if $E_{XC}$ were known, the exact ground state energy and density of the many-body problem could be found upon solving the Kohn-Sham equations for independent particles.

Minimisation of the energy with respect to the wave-functions gives the following equation

$$\frac{\delta E_{KS}}{\delta \psi_i(\mathbf{r})} = \frac{\delta T_S}{\delta \psi_i(\mathbf{r})} + [\frac{\delta E_{ext}}{\delta n(\mathbf{r})} + \frac{\delta E_{Hartree}}{\delta n(\mathbf{r})} + \frac{\delta E_{XC}}{\delta n(\mathbf{r})}]\frac{\delta n(\mathbf{r})}{\delta \psi_i(\mathbf{r})} = 0, \tag{2.16}$$

which is explained in detail in page 139 of Martin [29]. This results in an expression for $V_s(\mathbf{r})$, the potential of non-interacting electrons

$$V_s(\mathbf{r}) = V_{ext}(\mathbf{r}) + \int d^3r' \frac{n(\mathbf{r})}{|\mathbf{r}-\mathbf{r}'|} + V_{XC}(\mathbf{r}), \tag{2.17}$$

where $V_{XC}(\mathbf{r}) = \frac{\delta E_{XC}}{\delta n(\mathbf{r})}$. As $E_{XC}[n]$ is still not known, the genius of the Kohn-Sham approach is that by explicitly separating the independent particle kinetic energy and the Hartree terms, the remaining $E_{XC}[n]$ can be approximated as a local functional of the density

$$E_{XC}[n] = \int d^3r\, n(\mathbf{r})\varepsilon_{XC}([n],\mathbf{r}), \tag{2.18}$$

where $\varepsilon_{XC}([n],\mathbf{r})$ is an energy per electron at point $\mathbf{r}$ that depends upon the density $n(\mathbf{r})$ in some neighbourhood of $n(\mathbf{r})$. It is possible to make simple approximations for the exchange-correlation energy which work well, and the simplest of these is the local desity approximation (LDA). In the LDA, the contribution to $E_{XC}$ from each infinitesimal volume in space, $d\mathbf{r}$, is taken to be the value it would have if the space were filled with a homogeneous electron gas with the same density as is found in $d\mathbf{r}$. The exchange-correlation energy for the homogeneous electron gas has been calcu-

lated by Ceperley and Alder [38] using Monte Carlo methods. The most common parametrisation for the LDA is that of Perdew and Wang [39].

An initial guess of the density $n(\mathbf{r})$ is used to calculate the effective potential $V_s$. The Kohn-Sham equation is then solved, producing a new wave-function, that gives a new density, which in turn will yield a new potential. This method continues until the input density coincides with the density resulting from the solution of $\hat{H}_{aux}$.

## 2.2 Structural Relaxations

The calculation of the total energy with respect to atomic positions will allow us to find the equilibrium configuration of the crystal structure. The Hellmann-Feymann theorem [40], which relates the derivative of the total energy with respect to a parameter, to the expectation value of the derivative of the Hamiltonian with respect to the same parameter. Using the atomic coordinates $\mathbf{R_I}$ as the parameter, the force $F_I$ on atom $I$ can be calculated as

$$\mathbf{F_I} = -\frac{\delta E}{\delta \mathbf{R_I}} = -\langle \psi \left| \frac{\delta H}{\delta \mathbf{R_I}} \right| \psi \rangle. \tag{2.19}$$

All the forces vanish at equilibrium and thus we can find the equilibrium geometry of the cell and the position of the atoms within it.

## 2.3 Plane Waves

Plane waves provide solutions of differential equations such as the Schrödinger equation. As we are concerned with periodic crystals, plane waves are especially appropriate for such periodic solids where they provide intuitive understanding as well as simple algorithms for practical applications. Using Bloch's theorem, which states that

the wave-function of a periodic solid is composed of a plane wave and a periodic part $u_{i,\mathbf{k}}(\mathbf{r})$,

$$\psi_{i,\mathbf{k}}(\mathbf{r}) = \frac{1}{\sqrt{N_{cell}}} e^{i\mathbf{k}.\mathbf{r}} u_{i,\mathbf{k}}(\mathbf{r}), \tag{2.20}$$

where $N_{cell}$ is the number of primitive cells, the index $i$ denotes the eigenstate for each wave vector $\mathbf{k}$ and $u_{i,\mathbf{k}}(\mathbf{r})$ satisfies

$$u_{i,\mathbf{k}}(\mathbf{r}+\mathbf{a}) = u_{i,\mathbf{k}}(\mathbf{r}), \tag{2.21}$$

where $\mathbf{a}$ is a lattice vector. The periodic part of the wave-function can be written in terms of the reciprocal lattice vectors $\mathbf{G_n}$ using a Fourier transform,

$$u_{i,\mathbf{k}}(\mathbf{r}) = \frac{1}{\sqrt{\Omega_{cell}}} \sum_n c_{i,n}(\mathbf{k}) e^{i\mathbf{G_n}.\mathbf{r}}, \tag{2.22}$$

where $\Omega_{cell}$ is the volume of the primitive cell. The reciprocal lattice vectors are defined to satisfy the condition

$$\mathbf{G}.\mathbf{a} = 2\pi\delta_{ij}. \tag{2.23}$$

The wave-function can now be rewritten as

$$\psi_{i,\mathbf{k}}(\mathbf{r}) = \frac{1}{\sqrt{\Omega}} \sum_n c_{i,n}(\mathbf{k}) e^{i(\mathbf{k}+\mathbf{G_n}).\mathbf{r}}, \tag{2.24}$$

where $\Omega = N_{cell}\Omega_{cell}$. We rewrite the Kohn-Sham equation in terms of plane waves

$$\sum_{n'} [\frac{1}{2} |\mathbf{k}+\mathbf{G_n}|^2 \delta_{n,n'} + V_s(\mathbf{G_n}-\mathbf{G_{n'}}) c_{i,n'}(\mathbf{k}) = \varepsilon_i(\mathbf{k}) c_{i,n}, \tag{2.25}$$

where the Fourier transform of the effective potential is

$$V_s(\mathbf{G}) = \frac{1}{\Omega_{cell}} \int_{\Omega_{cell}} V_s(\mathbf{r}) e^{-i\mathbf{G}.\mathbf{r}}\, d\mathbf{r}. \tag{2.26}$$

Since the Schrödinger equation is defined for each **k**, each state can be labelled by the wavevector **k** and the eigenvalues and eigenvectors for each **k** are independent unless they differ by a reciprocal lattice vector. In the limit of large volume Ω, the **k**-points become a dense continuum and the eigenvalues $\varepsilon_{\mathbf{k}}$ become continuous bands.

All possible eigenstates are specified by the wavevector **k** within any one primitive cell of the periodic lattice in reciprocal space. The best possible cell is the first Brillouin zone as it is the most compact cell possible with its boundaries being the bisecting planes of the **G** vectors. Inside the Brillouin zone the bands must be continuous.

For a periodic system, integrals over the first Brillouin zone in reciprocal space, are performed by summing the function values of the integrand (for instance the charge density) at a finite number of points in the Brillouin zone, called the **k**-point mesh. Choosing a sufficiently dense mesh of integration points is crucial for the convergence of the results, and is therefore one of the major objectives when performing convergence tests. It should be noted that there is no variational principle governing the convergence with respect to the **k**-point mesh. This means that the total energy does not necessarily show a monotonous behaviour when the density of the **k**-point mesh is increased. The **k**-points are chosen according to the scheme proposed by Monkhorst and Pack [41].

## 2.4 Pseudopotentials

A solution to the Kohn-Sham equations is possible upon careful selection of a **k**-point mesh and using a plane wave energy cut-off in the Fourier expansion of the

wavefunctions. However, the use of plane-waves as a basis for the wave-functions does not work so well, as a very large number of plane-waves are required to describe the wavefunctions of electrons in the core region. Most physical properties of solids are dependent on the valence electrons to a greater extent than the non-valence tightly bound core electrons.

Thus a pseudopotential approximation is used in order to attempt to replace the strong Coulomb potential and core electrons by an effective pseudopotential which is much weaker. The valence electron wave-functions, which oscillate rapidly in the core region, are then replaced by pseudo-wave-functions, which vary smoothly in the core region, as shown in Fig. 2.1.

The valence wavefunctions oscillate rapidly in the core electron region in order to maintain orthogonality with the core electrons. The pseudopotential is constructed so that there are no radial nodes in the pseudo wavefunction in the core region and that the pseudo wavefunctions and potential are identical to the all electron wavefunction and the potential outside a cut-off radius, $r_c$. The pseudopotential is also constructed so that the scattering properties of the pseudo wavefunctions are identical to the scattering properties of the ion and core electrons, which will be different for each angular momentum component of the valence wavefunction. Thus the pseudopotential is dependent on the angular momentum and is referred to as non-local pseudopotential. In general, the pseudopotential is formed with local and non-local parts,

$$V_{ps}(r) = V_{local}(r) + \sum_{l,m} V_l(r) \left|Y_{lm}\right\rangle \left\langle Y_{lm}\right| , \tag{2.27}$$

where $|Y_{lm}\rangle$ are the spherical harmonics and $V_l(r)$ is the pseudopotential for angular momentum $l$.

Norm-conserving pseudopotentials are one of the most common type of pseudopotentials used in modern plane-wave ab initio codes. We use the pseudopotentials of

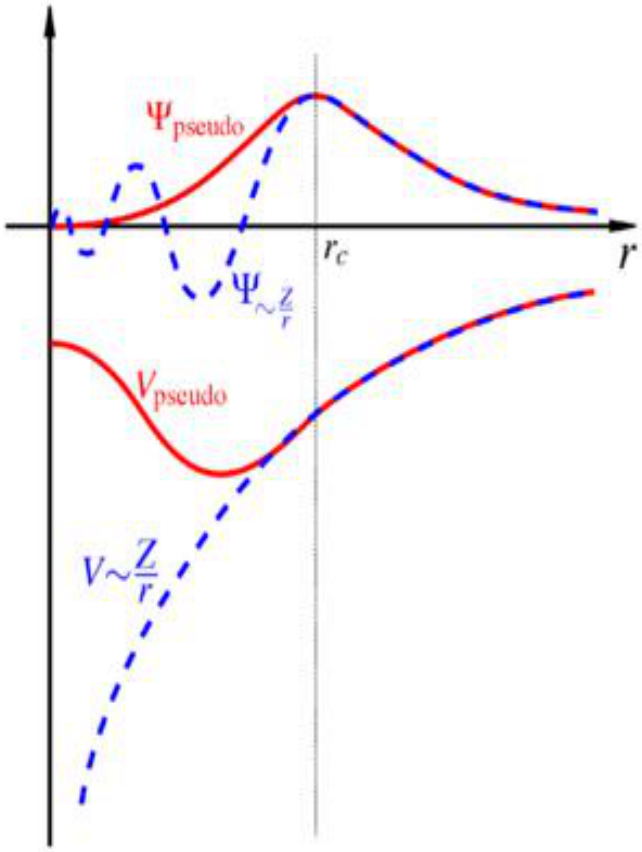


Figure 2.1: The all electron wavefunction $\Psi$ and potential (dashed lines) plotted against distance $r$, from the nucleus. The pseudo wavefunction $\Psi_{pseudo}$ and potential is plotted (solid line). Outside the cut-off radius $r_c$, the all electron and pseudo electron values are identical.

Hartwigsen, Goedecker and Hutter [42] and Troullier and Martins [43] in this work.

## 2.5 Exchange-Correlation Functionals

As already mentioned in Section 2.1, the simplest approximation to calculating the exchange-correlation functional is to assume the density can be treated as an uniform electron gas. The exchange-correlation energy at each point in the system is the same as that of an uniform electron gas of the same density. This approximation which was originally introduced by Kohn and Sham, which is called the local density approxi-

mation (LDA) [39] is given by

$$E_{XC}^{LDA}[n] = \int d^3r\, n(\mathbf{r})\varepsilon_{XC}([n],\mathbf{r}) \tag{2.28}$$

where $\varepsilon_{XC}(n)$ is the exchange-correlation energy per particle of an uniform electron gas of density $n$. The exchange-correlation potential is given as

$$V_{XC}^{LDA}[n(\mathbf{r})] = \frac{\delta E_{XC}^{LDA}}{\delta n(\mathbf{r})} = \varepsilon_{XC}([n],\mathbf{r}) + n(\mathbf{r})\frac{\partial \varepsilon_{XC}([n],\mathbf{r})}{\partial n} \tag{2.29}$$

This can then be inserted into the equation for $V_s(r)$.

As LDA approximates the energy of the true density by the energy of a local constant density, it fails in situations where the density undergoes rapid changes such as in molecules. An improvement to this can be made by considering the gradient of the electron density called the generalized gradient approximation (GGA) [44], written as

$$E_{XC}^{GGA} = E_{XC}[n(\mathbf{r}), \nabla n(\mathbf{r})]. \tag{2.30}$$

There are several different parameterizations of the generalized gradient approximation, some of which are semi-empirical, in that experimental data (e.g. atomization energies) is used in their derivation.

Methods for calculating the van der Waals (vdW) interactions are important in understanding bulk solids and surface phenomena. For homogeneous systems such as simple metals and semiconductors, LDA is appropriate for the interaction effects. For inhomogeneous systems such as transition metals and ionic crystals, GGA works very well. Thus the local density and generalized gradient approximations are quite accurate in hard materials and covalently bonded molecules, in which they depend on the density in local and semi-local ways. Today DFT describes cohesion, bonds,

structure and other properties very well for dense molecules and materials as shown in recent studies [45] and [46]. However, these approximations give no account of the fully nonlocal vdW interaction. Spares systems, including soft matter and van der Waals complexes are at least as abundant. They have inter-particle separations, for which nonlocal, long-ranged interactions such as van der Waals forces, are influential.

First-principles approaches for how vdW can be treated in DFT were first proposed for the asymptotic interaction between fragments [47, 48, 49]. These ultimately evolved into the van der Waals density functional for arbitrary geometries [50, 51, 52, 53]. In the work by Dion *et al.* [50], they develop and apply a van der Waal density functional (vdW-DF) for general geometries to supplement the planar vdW-DF that was applied to several layered materials [54]. Despite its success for describing dispersion in a breadth of systems better than any other non-empirical method [55], vdW overestimates equilibrium separations [50, 51, 55] and underestimates hydrogen-bond strengths. [56, 57]

In the further work proposed by Lee *et al.* [58], they propose a second version of the vdW-DF of Dion *et al.* [50]. They propose a more accurate semi-local exchange-correlation functional [59, 60] with the use of a large-$N$ asymptote gradient correction in determining the vdW kernel [50]. Lee shows that the vdW-DF2 substantially improves the equilibrium separations, hydrogen-bond strengths and vdW interactions at intermediate separations longer than the equilibrium ones.

The key to the vdW-DF method is the inclusion of a long-range piece of the correlation energy $E_{XC}^{nl}[n]$, a fully nonlocal functional of the density $n$. This piece is evaluated using a plasmon pole approximation for the inverse dielectric function [50]. A single parameter model for the pole position was used, with the pole residue set by the law of charge-current continuity, and the pole position at the large wave vector set by the constraint that there be no self-Coulomb interaction. The single parameter is determined locally from electron-gas input via gradient corrected LDA [50]. The

non-local correction of the correlation energy is of the form

$$E_{XC}^{nl}[n] = \int d^3r\, d^3r' n(\mathbf{r})\phi(\mathbf{r},\mathbf{r}')n(\mathbf{r}'), \tag{2.31}$$

where the kernel $\phi$ is given as a function of $Rf(\mathbf{r})$ and $Rf(\mathbf{r}')$ and $R = |\mathbf{r}-\mathbf{r}'|$ and $f(\mathbf{r})$ is a function of $n(\mathbf{r})$ and its gradient. The function $f(\mathbf{r})$ in fact is proportional to the exchange-correlation energy density $\varepsilon_{XC}$ of a gradient corrected LDA at the point $\mathbf{r}$. A full analysis of this vdW-DF2 method is explained in greater detail in the work by Lee *et al.* [58].

## 2.6 Harmonic Approximation

In this thesis we are concerned with using density functional theory to calculate vibrational mode frequencies of adsorbed species on a germanium surface. Here we review the relevant theory of lattice dynamics within the harmonic approximation that are used in this work.

Consider a system of $N$ atoms, let $M_i$ be the mass of atom $i$ and $d_\alpha(i)$ be the displacement from equilibrium in the direction $\alpha(x,y,or\ z)$. The total energy $E$ of the crystal structure is a function of atomic position, assuming an adiabatic approximation, stating that the electrons are in their ground state for any particular atomic arrangement [61] and using a Taylor series, we expand the total energy about the equilibrium structure.

$$E = E_0 + \sum_{i,\alpha}\phi^1_\alpha(i)d_\alpha(i) + \frac{1}{2}\sum_{i,j,\alpha,\beta}\phi^2_{\alpha\beta}(i,j)d_\alpha(i)d_\beta(j) + \frac{1}{6}\sum_{i,j,k,\alpha,\beta,\gamma}\phi^3_{\alpha\beta\gamma}(i,j,k)d_\alpha(i)d_\beta(j)d_\gamma(k) + ...., \tag{2.32}$$

where $E_0$ is the total energy when the atoms are in the equilibrium position. The coefficients $\phi^1_\alpha(i)$, $\phi^2_{\alpha\beta}(i,j)$ and $\phi^3_{\alpha\beta\gamma}(i,j,k)$ are the derivatives of the total energy with respect to displacement evaluated at equilibrium. As the forces on all atoms are zero at equilibrium,

$$F_\alpha(i) = -\left(\frac{\delta E}{\delta d_\alpha(i)}\right)\Big|_{equilib} = -\phi^1_\alpha(i), \tag{2.33}$$

the coefficient $\phi^1_\alpha(i)$ vanishes and the remaining coefficients are given by

$$\phi^2_{\alpha\beta}(i,j) = \left(\frac{\delta^2 E}{\delta d_\alpha(i)\delta d_\beta(j)}\right)\Big|_{equilib}, \tag{2.34}$$

and

$$\phi^3_{\alpha\beta\gamma}(i,j,k) = \left(\frac{\delta^3 E}{\delta d_\alpha(i)\delta d_\beta(j)\delta d_\gamma(j)}\right)\Big|_{equilib}. \tag{2.35}$$

Within the harmonic approximation we neglect terms beyond the quadratic one. As the equilibrium energy $E_0$ can be set to zero and the second term of Eq. 2.32 is equal to zero, we therefore obtain

$$E \approx \frac{1}{2}\sum_{i,j,\alpha\beta} \phi^2_{\alpha\beta}(i,j)\delta d_\alpha(i)\delta d_\beta(j) \tag{2.36}$$

## 2.7 Dynamical Matrix

The dynamical properties of a crystal structure are described by its dynamical matrix containing the second partial derivatives of the total energy $E$ with respect to the displacement of the atoms about their equilibrium position. Upon substitution of a mass weighted displacement,

$$e_\alpha(i) = \sqrt{M_i} d_\alpha(i) \tag{2.37}$$

yields the energy from Eq. 2.36 as

$$E = \frac{1}{2} \sum_{i,j,\alpha,\beta} (M_i M_j)^{-\frac{1}{2}} \phi^2_{\alpha\beta}(i,j) e_\alpha(i) e_\beta(j). \tag{2.38}$$

The dynamical matrix $D$ is defined as

$$D_{\alpha,\beta}(i,j) = (M_i M_j)^{-\frac{1}{2}} \phi^2_{\alpha\beta}(i,j). \tag{2.39}$$

To calculate the dynamical matrix, the force constant matrix, defined as the second partial derivative of the total energy with respect to the atomic displacement must be known. The matrix elements are found upon calculating the forces on atom $i$ in the direction $\alpha$, $F_\alpha(i)$, due to the displacement of atom $j$ the direction in $\beta$, $d_\beta(j)$,

$$F_\alpha(i) = -\phi_{\alpha\beta}(i,j) d_\beta(j) \tag{2.40}$$

This matrix describes the forces on each atom due to small displacements of the system from the equilibrium. The dynamical matrix has the following properties (a) the matrix is symmetric of order $3N$ and (b) all the matrix elements are real.

Upon diagonalization of the dynamical matrix we obtain the eigenvalues $\lambda_k = \omega_k^2$ and the normalized eigenvectors $|u_k\rangle$, where

$$\langle i,\alpha \rangle u_k = u_k(i,\alpha) = \sqrt{M_i} s_k(i,\alpha) \tag{2.41}$$

where $s_k$ is the amplitude of motion of atom $i$ in the direction $\alpha$ for the vibrational mode $k$.

## 2.8 Projected Band Structure

In this thesis we are interested in the electronic structure of interfaces, particularly if such interface states exist in the band gap. At the beginning of Chapter 3, we show a germanium surface that has two dangling bonds. These dangling bonds are referred to as surface states and appear in the band gap of a projected band structure calculation. Surface states are electronic states found at the surface of materials. They are formed due to the sharp transition from solid material that ends with a surface and are found only at the atom layers closest to the surface. The termination of a material with a surface leads to a change of the electronic band structure from the bulk material to the vacuum. In the weakened potential at the surface, new electronic states can be formed, so called surface states. Here we provide the background into how we visualise such states using a projected band structure calculation.

Bulk crystals are three-dimensional and the wavevectors **k** and the Brillouin zone are three-dimensional vectors and objects, respectively. A surface breaks the lattice periodicity in one direction and the three-dimensional lattice-periodic translational symmetry reduces to two directions parallel to the surface. The unit cell for the atoms is semi-infinite in the direction normal to the surface, thus reducing the symmetry of the underlying crystal. For example, in a cubic crystal when the symmetry is lowered, the wavevector $\mathbf{k}=(k_{\perp},\mathbf{k}_{\parallel})$ is no longer a good quantum number, whereas the two-dimensional parallel component $\mathbf{k}_{\parallel}$ remains a good quantum number. Thus electronic states are described by two-dimensional wavevector $\mathbf{k}_{\parallel}$ and by two-dimensional Brillouin zones called surface Brillouin zones.

An ideal surface is obtained by slicing through the crystal with an infinite two-dimensional plane along crystal planes. The band structure of this semi-infinite space is obtained by projecting the three-dimensional band structure on the two-dimensional surface Brillouin zone, thus

$$\varepsilon_{\mathbf{k}} = \varepsilon_{(\mathbf{k}_{\parallel},k_{\perp})} = \varepsilon_{\mathbf{k}_{\parallel}(k_{\perp})} \tag{2.42}$$

The resulting band structure is called the projected band structure. From Fig. 2.2 it is clear that in the case of the (001) surface all states of $k_{\perp}$ between $\Gamma$ and $X$ contribute to the two-dimensional $\mathbf{k}_{\parallel}$-point $\bar{\Gamma}$.

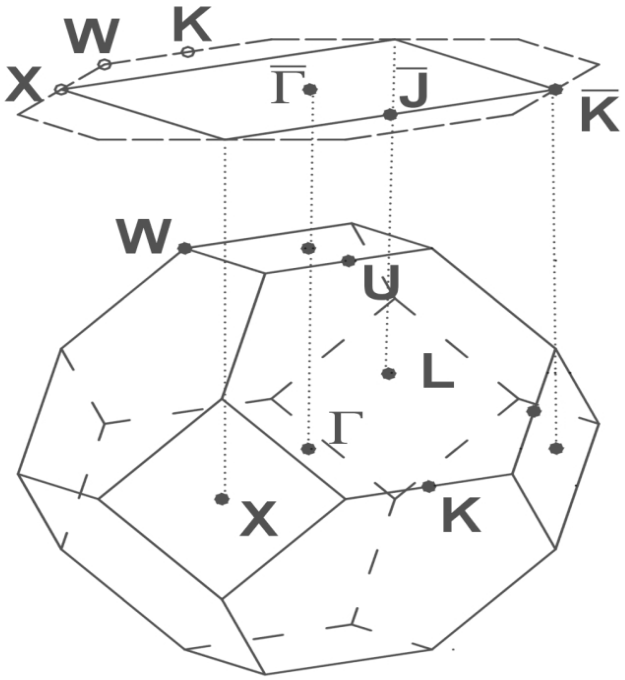


Figure 2.2: High symmetry points of a face centred cubic three-dimensional Brillouin zone projected onto a surface Brillouin zone.

First we consider a surface slab model to calculate a band structure around a surface Brillouin zone path which is two-dimensional. Then, using the bulk structure for the material (i.e, a small primitive cell), we run many conventional band structure calculations around a path that is equivalent to the surface Brillouin zone path but offset along $k_{\perp}$ by an increasing value. The difficulty is translating the path from the surface

Brillouin zone back to the equivalent path in the bulk Brillouin zone. We then take that same set of k-points and add a constant $k_\perp$ for increasing values of $k_\perp$ until you reach the Brillouin zone boundary. Once this is done for a sufficient number of $k_\perp$ values, plotting the bandstructures overlaying each other it is easy to see which regions are forbidden and so on. The projected band structure is generally shaded and we then overlay the actual surface slab band structure to see which surface states exist.

CHAPTER 3

# Germanium (001)-$(2 \times 1)$ Surface

---

*The structural and electronical characteristics of a Ge(001)-$(2 \times 1)$ surface are calculated in a supercell approach using first-principles density functional theory in the local density approximation (LDA). Self-consistent calculations determine the atomic structure and the projected band structure calculation shows that surface states do exist in the band gap. These states are described as dangling bond states due to the up atom and down atom of the Ge-Ge dimer.*

## 3.1 Introduction

In this chapter we begin with reproducing the work by Rohlfing *et al.* [27] of a clean Ge(001) surface using the density functional theory methods that have been described in detail in Chapter 2. This is a benchmarking exercise to show that our DFT calculations of a germanium surface produce the same results as published in the literature. This then provides us with the correct foundations using DFT, to investigate theoretically the vibrational mode frequencies of adsorbed species on a germanium surfaces in Chapter 4, the GeSi interfaces in Chapter 5 and finally the presence of both sulfur and hydrogen on the GeSi interface in Chapter 6.

Clean Ge(001) surfaces have been studied intensively in both experiment [62, 63] and theory [64, 65, 66, 67]. This surface is an interesting example of a system that

possesses both a strong short-range interaction as well as an energetically weaker, longer-range ordering. The basic $(2 \times 1)$ reconstruction is generally accepted to entail the formation of dimers, created through pairing of nearest neighbor surface atoms [68, 69]. However, Chadi [70, 71, 72] introduced a symmetry reducing distortion in a model of the Si(001) surface by using asymmetrical rather than symmetrical dimers. In this empirical tight-binding total-energy calculation, the optimal $(2 \times 2)$ and $(4 \times 2)$ [73, 74, 75, 76] surface reconstructions correspond to different arrangements of buckled asymmetric dimers with partially ionic bonds between dimer atoms.

Detailed studies of the surface electronic structure of Ge(001)-$(2 \times 1)$ [77] have been performed with angle-resolved photoemission [78], whereby surface states or resonances, i.e. the dangling-bond state and two different back-bond resonances are observed [79]. A full analysis of these surface states are found in Ref [80, 81, 82, 83].

In the work produced by Rohlfing *et al.* [27], on the clean Ge(001)-$(2 \times 1)$ surface, asymmetric dimers are formed that are arranged in rows, while in the electronic structure of this surface, two dangling-bond bands occur within the energy region of the fundamental gap.

The theoretical work for this surface has been carried out using density functional theory in the local density approximation (LDA) as the exchange-correlation functional. This allows for a very accurate analysis of the atomic structure by total-energy minimization. LDA has proven in a large range of bulk and surface systems to yield geometrical structures in excellent agreement with experimental data. However agreement is not so good with the band structure calculations. The energy band gap between occupied and unoccupied electronic states of a semiconductor system is underestimated by using LDA.

For surface states the problem becomes even more complicated. As stated in [27], for many systems the LDA error in the surface gap is different from that in the bulk gap. Furthermore, the LDA energy of occupied surface states may not be reliable in

some cases [84].

## 3.2 Method of Calculation

We use the Teter-Pade parameterization [39] of the local density approximation (LDA) for the exchange-correlation functional, which allows for an accurate analysis of the atomic structure by total energy minimisation. We use the ABINIT [85] code to calculate the ground state energies and Hellmann-Feymann(HF) forces. [40] We use the pseudopotentials of Hartwigsen, Goedecker and Hutter for germanium [42] and Troullier and Martins [43] for hydrogen. The plane-wave cutoff energy was set at 10 Ha. The method of special k-point generation is based on the Monkhorst-Pack [41] scheme. We have used an $(4 \times 4 \times 4)$ k-point mesh for all supercells considered. Structures are optimised until the residual HF forces are less than 0.026 eV/Åand the surface is relaxed with atomic forces using the Broyden method [86].

The germanium surface is modelled using a nine-layer periodic slab of germanium atoms with a vacuum layer of 11 Å in a $(2 \times 1)$ supercell geometry, as shown in Fig. 3.1(a). Each germanium atomic layer has 2 atoms per layer. The bottom surface is terminated with hydrogen atoms to represent the underlying bulk, giving a total of 22 atoms (18 germanium and 4 hydrogen). The lattice constant is held fixed at the calculated equilibrium value of 5.58 Å for bulk germanium, which is about 1% smaller than the experimental value of 5.65 Å.

## 3.3 Results

On relaxation, the germanium surface results in a Ge(001)-$(2 \times 1)$ reconstructed surface, with Ge-Ge asymmetric dimers arranged in rows as shown in Fig. 3.1(b). The Ge-Ge buckled dimer has a bond length of 2.43 Å and a buckling angle of 19° which

is in agreement with the work by Rohlfing *et al.* Ref. [27].

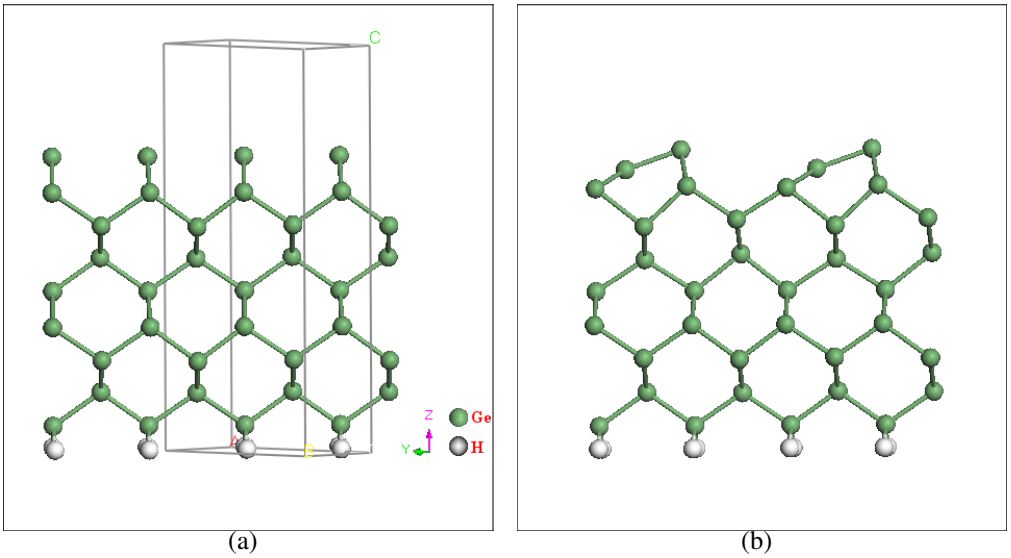


(a) (b)

Figure 3.1: A nine layer slab of germanium atoms, terminated with H on the bottom surface. (a) Is the initial atomic configuration before structural relaxation. The grey line represents the $(2 \times 1)$ supercell geometry. (b) The final relaxed geometry of the Ge(001)-$(2 \times 1)$ surface.

The more important features of the electronic structure are presented in the projected band structure in Fig. 3.2(a). The projected band structure for the Ge(001)-$(2 \times 1)$ surface shows a band gap of 0.26 eV which is consistent with [77]. This value is much less that the experimental band gap of 0.66 eV [87], which is typical of the LDA calculation. Two distinct dangling-bond states $D_{up}$ which is occupied and $D_{down}$ which is unoccupied are shown in Fig. 3.2(a). They are mainly formed by the $4p_z$ orbitals of the germanium dimer atoms. These states throughout the surface Brillouin zone are localized at the up or down atoms of the asymmetric dimer, respectively, as shown in the charge density plots in Fig. 3.2(b) and Fig. 3.2(c) and consistent with the work presented in [77] and [27]. Both the $D_{up}$ and $D_{down}$ charge density contour plots in Fig. 3.2(b) and Fig. 3.2(c) are calculated at the $\overline{K}$-point. The back bond state $B$ which is an occupied state induced by the surface is shown in Fig. 3.2(d).

It is important to note the following. The formation of dimers using chemical

bonding arguments: each Ge atom carries four valence electrons. The outermost surface atoms accommodate two valence electrons each in bonding orbitals with the layer of atoms underneath, while the remaining two electrons occupy one surface dangling bond each. This leads to four half-filled orbitals for each pair of surface Ge atoms. In these conditions it is energetically more favourable for the structure to rearrange to have only three orbitals occupied, two dangling ones and a third one in between the two atoms of a dimer. The dangling bonds will be singly occupied while the dimer bond will be doubly occupied. The double occupation of a dimer bond instead of two dangling bonds is energetically favourable. In Ge(001)-$(2 \times 1)$ reconstruction each dimer carries two identical half occupied dangling bonds and it is possible to reduce the total energy by tilting the dimer in such a way as to make these orbitals inequivalent. In the tilted configuration which we see in Fig. 3.1(b) called the asymmetric dimer model (ADM), since the two dangling bonds are inequivalent they must have different energies, hence the two electrons will both occupy the orbital with the lowest energy. The calculation shows the four electrons localised around the higher Ge atom of the dimer while only three electrons approximately localise around the lower Ge atom. This is an example of a broken symmetry leading to a stabilisation of the structure. This is the reason why the dangling bond state $D_{up}$ in Fig. 3.2(b) is fully occupied and the $D_{down}$ in Fig. 3.2(c) is unoccupied.

## 3.4 Conclusion

In conclusion we have reproduced the theoretical results of [27] for a Ge(001)-$(2 \times 1)$ surface using density functional theory methods. The asymmetric dimer is produced at the Ge(001)-$(2 \times 1)$ surface. The projected band structure shows two distinct states in the band gap, which are dangling-bond states on the surface germanium atoms.

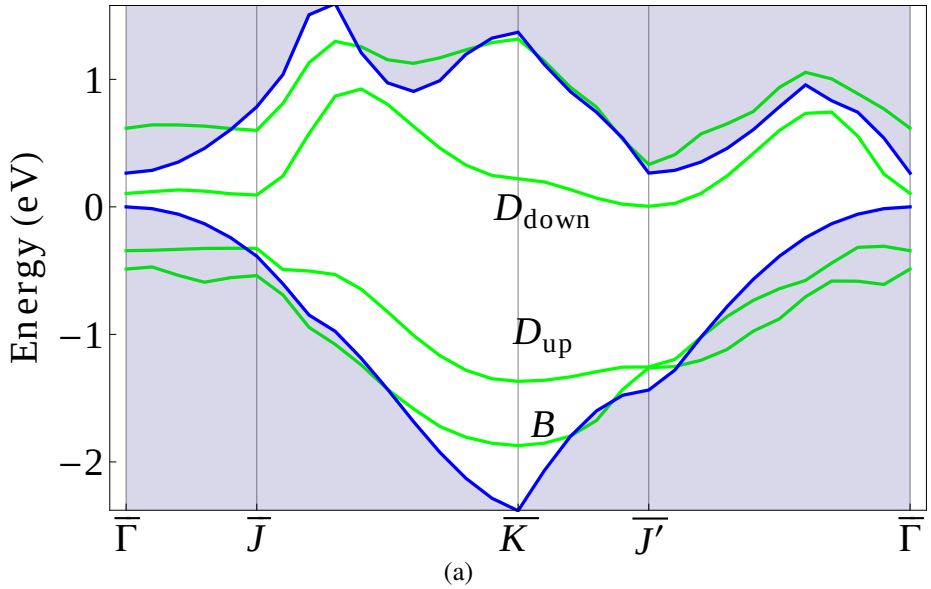


(a)

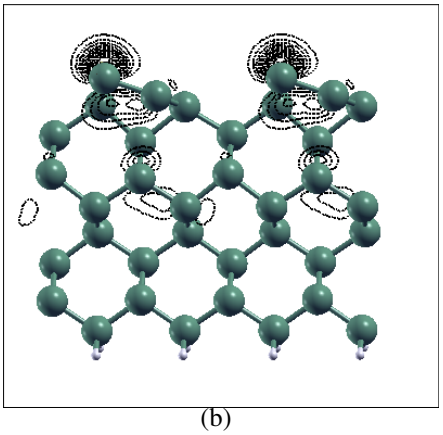

(b)

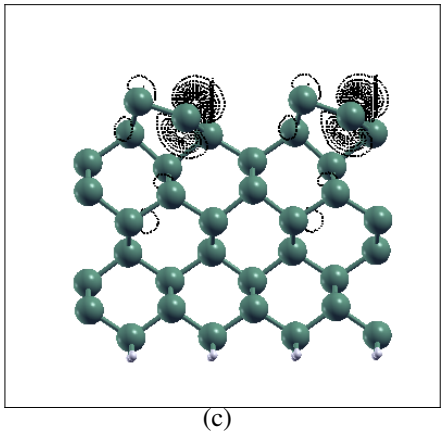

(c)

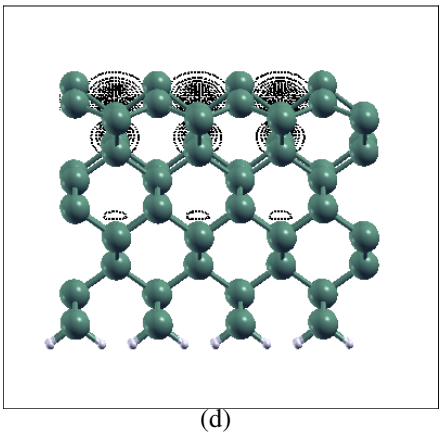

(d)

Figure 3.2: (a) Projected band structure of the clean Ge(001)-(2 × 1). The shaded area denotes the projected bulk band structure. Two distinct dangling-bond states $D_{up}$ and $D_{down}$ and a back bond state $B$ are shown in green. Calculated charge density at the $\overline{K}$-point for the dangling-bond states (b) $D_{up}$ and (c) $D_{down}$ and the back bond state (d) $B$.

CHAPTER 4

# Vibrational Mode Frequencies of Adsorbed Species on Ge Surfaces

---

*The equilibrium geometry and vibrational modes of $H_2S$ and $H_2O$-terminated Ge(001)-($2 \times 1$) surfaces are calculated in a supercell approach using first-principles density functional theory in the local density (LDA), generalized gradient (GGA) approximations and van der Waals (vdW) interactions. Mode frequencies are found using the frozen phonon method.*

## 4.1 Introduction

Clean and adsorbed Ge(001) surfaces have been studied both in theory and experiment. [20, 27] The bare Ge(001) surface undergoes reconstruction, forming buckled dimers arranged in rows and reducing the number of dangling bonds from two to one. This germanium surface exhibits dangling-bond states in the fundamental energy gap, [27] making it reactive and unsuitable for electronic applications. To reduce such surface states on the Ge(001) surface, a passivation process is required to saturate the dangling bonds.

Hydrogen, sulphur and water have been studied as absorbates on the Ge surface. [27, 88] An absorbed monolayer of hydrogen completely passivates the Ge surface,

with Ge-H bonding states lying far below the fundamental energy gap [27] in a $(2 \times 1)$ symmetric dimer structure. A monolayer of sulfur causes the bare $(2 \times 1)$ Ge surface to reconstruct, restoring the $(1 \times 1)$ bulk-like geometry but leaving surface electronic states in the fundamental gap. [27]

To further passivate the sulfur-terminated surface, termination of the Ge(001) surface by $H_2S$ has been studied, [22] showing that the terminated surface forms a $(2 \times 1)$ reconstruction with (S-H) bonded on each of the Ge dimer atoms. The computed energy band gap of this configuration is free of surface states, which is of relevance to the future application of germanium in high performance integrated circuits.

Water, a contaminant in many growth and fabrication processes, also passivates the Ge(001) surface. [88] Lee *et al.* [88] showed that terminating the Ge(001) surface with $-$OH and $-$H removes the surface states and thus proposed that $H_2O$ might be used at low temperature for surface passivation. Besides the practical interest in passivation by both molecules in their own right, given the chemical similarities between $H_2O$ and $H_2S$, it is of interest to compare their bonding with the Ge surface.

Infrared spectroscopy is often used to confirm or investigate proposed bonding geometries at surfaces, as pioneered in work of Chabal. [23] In this chapter, having confirmed previously proposed bonding geometries of both $H_2S$, [22] and $H_2O$, [89] on the Ge(001) surface using density functional theory, we calculate and compare the vibrational mode frequencies for these structures for different exchange-correlation functionals, with and without van der Waals interactions, providing useful vibrational signatures of particular bonding geometries. Our results may be used in combination with infrared spectroscopy to confirm the surface geometries proposed in Refs. [22] and [89].

Van der Waals (vdW) interactions [90] or dispersive forces between two atoms or two molecules arise from the interaction of induced dipole moments, because the charge fluctuations in one part of the system are electrodynamically correlated with

charge fluctuations of another. These dispersive forces at one point therefore depends on charge events at another. Thus, this quantum mechanical phenomenon is a nonlocal correlation effect.

## 4.2 Method of Calculation

In our calculations the surfaces are represented in a supercell geometry [29]. Structural total energies and atomic forces are calculated using first-principles density functional theory [91] in both the local density (LDA) and generalized gradient (GGA) approximations [91]. Vibrational mode frequencies are obtained using the frozen phonon method [92], in which the dynamical matrix is calculated from the fitted restoring forces in the harmonic limit. Diagonalization of the dynamical matrix gives the vibrational mode frequencies and corresponding atomic motions for the $H_2S$ and $H_2O$ adsorbed on a Ge(001)-(2 $\times$ 1) surface. We also report the equilibrium bond lengths and angles at the surface and the energies required for breaking these surface bonds.

We use local density approximation (LDA) of Perdew-Wang [39] and the generalized gradient approximation (GGA) proposed by Perdew-Burke-Ernzerhof [44], as provided in the *ab initio* codes used which we will discuss later. Both exchange-correlation functionals allow for an accurate analysis of the atomic structure by total energy minimisation. We calculate results with both to give an indication of the uncertainties arising from the specific form of the exchange-correlation functional used. We use the QUANTUM ESPRESSO [91] code to calculate the ground state energies and Hellmann-Feymann(HF) forces. [40] The *ab initio* separable pseudopotentials used by QUANTUM ESPRESSO have been computed in both LDA and GGA with the code of the Fritz-Haber-Institute (FHI) [93] implementing the scheme of Troullier-Martins [43], so that the *3d* states of Ge have been fully treated as valence states. The plane-wave cutoff energy was set at 10 Ha and 20 Ha for calculations involving sul-

fur and oxygen, respectively. The method of special k-point generation is based on the Monkhorst-Pack [41] scheme. We have used an 8 k-point mesh for all supercells considered.

The germanium surface is modelled using a nine-layer periodic slab of germanium atoms with a vacuum layer of 11 Å, as shown in Fig. 4.1(a). The bottom surface is terminated with hydrogen atoms to represent the underlying bulk. The lattice constant is held fixed at the calculated equilibrium value of 5.57 Å for bulk germanium, which is about 1% smaller than the experimental value of 5.65 Å. On relaxation, the Ge surface results in a Ge(001)-$(2 \times 1)$ reconstructed surface, with a Ge-Ge buckled dimer bond length of 2.43 Å and a buckling angle of 19°, in agreement with Ref. [27] where the dimer bond length is 2.42 Å and the buckling angle is 19°.

Two $H_2S$ molecules are then positioned above the calculated equilibrium Ge(001)-$(2 \times 1)$ surface containing the Ge-Ge buckled dimers, as shown in Fig. 4.1(b) [22] and the structure is relaxed with atomic forces using the Broyden quasi-Newton algorithm [86]. One of the two $H_2S$ molecules is adsorbed onto the surface, by bonding of the S atom to one of the Ge dimers (forming a Ge-S-H bond) while the other H atom is adsorbed onto one of the Ge dimers from the neighbouring dimer row, forming a Ge-H bond, as shown in Fig. 4.1(c). The Ge-H bond has been reported to break, with desorption of H from the surface at temperatures in the range of $200 - 250$ °C, [94] and since the temperature used for $H_2S$ exposure is 330 °C, [22] breaking of the Ge-H bond should occur. As we cannot simulate such a scenario directly with our molecular dynamics, we artificially cause the H desorption by breaking the Ge-H bond and moving the H atom away from the surface. With the Ge-H bond broken, another $H_2S$ molecule adsorbs onto the surface. The equilibrium geometry after structural relaxation produces Ge-S-H bonds on a $(2 \times 1)$ reconstructed surface, as shown in Fig. 4.1(d).

Weak van der Waals (vdW) interactions during the adsorption process might ap-

pear to be a concern when some species are neither entirely desorbed nor adsorbed. In order to investigate if such vdW interactions do occur, we complete an analysis with a larger unit cell (vacuum layer $\approx 30$ Å) to ensure negligible interaction of the desorbed species with the surface, as is physically required. First-principles approaches for how vdW can be treated in DFT were proposed by Lee *et al.* [58], where they propose a second version of the vdW density functional of Dion *et al.* [50]. The structures Fig. 4.1(c) and Fig. 4.1(d) are re-relaxed as before with this larger unit cell and the vdW density functional as described in Ref. [58]. In LDA, the $H_2S$ molecule in Fig. 4.1(c) is located $\approx 0.4$ Å above its initial position due to vdW as shown in Fig. 4.2(a) and with an energy gain of $\approx 36$ eV per supercell. While in GGA the molecule is closer to the surface by $\approx 0.1$ Å as shown in Fig. 4.2(a) and with an energy gain of $\approx 28$ eV per supercell. The $H_2$ molecule in Fig. 4.1(d) for LDA is $\approx 2.1$ Å further away due to vdW as shown in Fig. 4.2(b) and with an energy gain of $\approx 36$ eV per supercell. While again GGA predicts the $H_2$ molecule closer to the surface by $\approx 0.3$ Å as shown in Fig. 4.2(b) and with an energy gain of $\approx 28$ per supercell. A full list of the total energies per supercell is given in the Appendix in Table A.1

However, it should be noted that in the initial and final physical geometries, all chemical species are considered to be either covalently bonded to the surface or are completely desorbed and far from the surface. Thus, we expect the weak vdW interactions will not be relevant to the final results presented. The differences between functionals including vdW terms and the LDA or GGA are expected to be substantially less than the differences between LDA and GGA.

The dissociation of the $H_2S$ molecule should this occur results in a equilibrium surface geometry as shown in Fig. 4.1(d). The total energy gain after dissociative adsorption from Fig. 4.1(c) to Fig. 4.1(d) is 0.25 eV (0.25) in LDA (GGA). This confirms that the $H_2S$-terminated Ge(001)-$(2 \times 1)$ surface in Fig. 4.1(d) is the most stable bonding geometry. Using vdW interactions in our geometry relaxation calculations,

the total energy gain after dissociative adsorption from Fig. 4.1(c) to Fig. 4.1(d) is 0.30 eV (0.31) in LDA (GGA), thus confirming Fig. 4.1(d) as the most stable structure. The calculated equilibrium lengths of the surface bonds are shown in Table 4.1. (This relaxed geometry is used as the initial atomic structure to calculate the GGA relaxed surface as shown also in Fig. 4.1(d))

## 4.3 Results and Discussion

A comparison of the bond lengths for LDA, GGA, vdW, experimental values and calculated covalent radii are presented in Table 4.1. The LDA Ge-Ge dimer bond length of 2.49 Å is in good agreement with the experimental value of $2.45 \pm 0.06$ Å measured using the grazing incidence x-ray diffraction from the clean Ge(001)-$(2 \times 1)$ surface [2]. The Ge-S bond lengths we calculated using LDA and LDA vdW and the H-S bond length using LDA provide better approximations when compared to the sum of their corresponding covalent radii [1].

Table 4.1: Calculated bond lengths (in Å) for $H_2S$ on a Ge(001) surface for the LDA, GGA and vdW relaxed structures shown in Fig. 4.1(d). Experimental bond lengths and calculated covalent radii from [a]Ref. [1] and [b]Ref. [2] are given. Note that the error bar associated with the bonding length in [b]Ref. [2] is in the order of 0.6 Å due to the limited data set.

| | | LDA | LDA vdW | GGA | GGA vdW | Expt | Cov Radii |
|---|---|---|---|---|---|---|---|
| Ge-S | Fig 4.1(d) | 2.22 | 2.23 | 2.27 | 2.29 | | 2.24[a] |
| Ge-Ge dimer | Fig 4.1(d) | 2.49 | 2.51 | 2.52 | 2.56 | 2.45[b] | 2.44[a] |
| H-S | Fig 4.1(d) | 1.38 | 1.36 | 1.37 | 1.36 | | 1.39[a] |
| H-H molecule | Fig 4.1(d) | 0.78 | 0.73 | 0.75 | 0.73 | | 0.74[a] |

The vibrational mode frequencies and atomic vibration amplitudes are determined upon diagonalization of the dynamical matrix. Within the harmonic approximation, the displacement $d_\beta(j)$ of atom j in the direction $\beta$ creates a force on atom i in the direction $\alpha$:

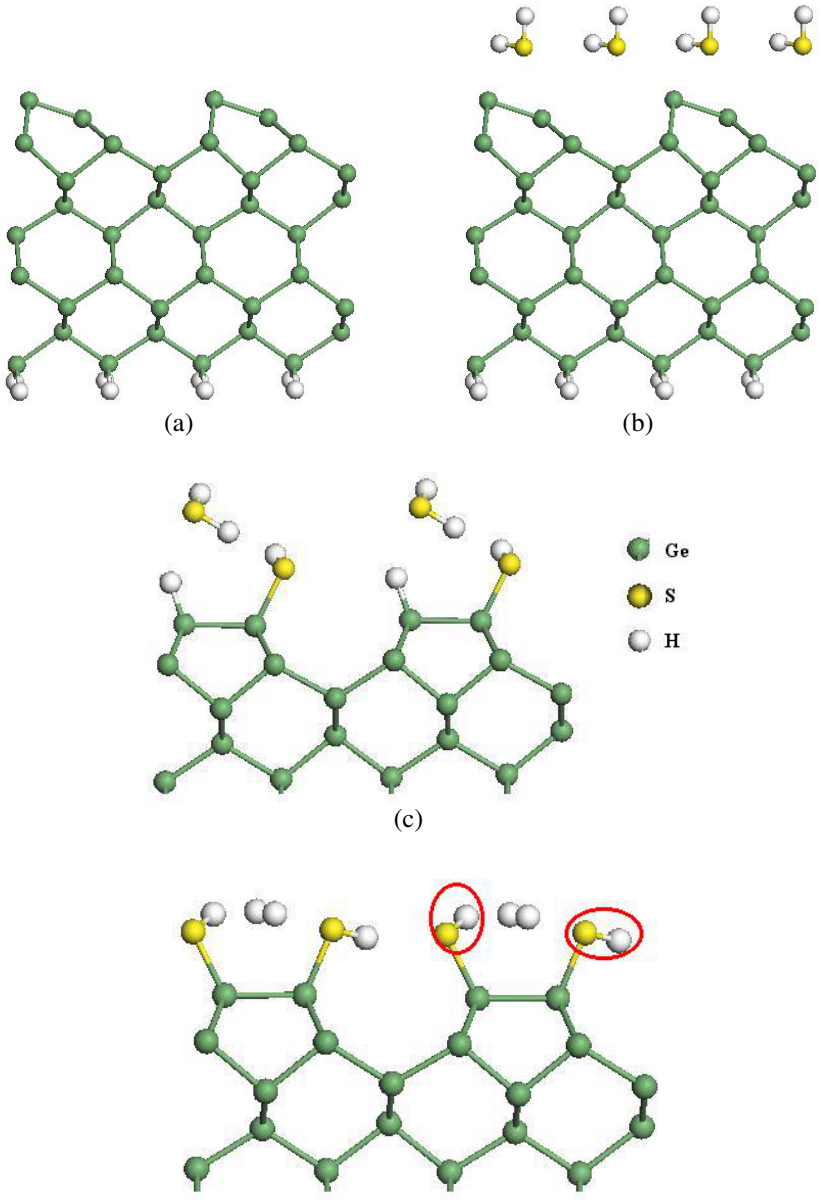


Figure 4.1: (a) A nine layer periodic slab of Ge atoms, terminated with H on the bottom surface. (b) Initial atomic configuration of the Ge(001)-(2 × 1) surface exposed to $H_2S$. (c) After structural relaxation one $H_2S$ is adsorbed onto the surface with the formation of Ge-S-H and Ge-H bonds. (d) Artificial breaking of the Ge-H bond allows another $H_2S$ molecule to be adsorbed onto the surface, producing a more stable equilibrium geometry. Two distinct surface sites on the Ge(001)-(2 × 1) surface are illustrated in red.

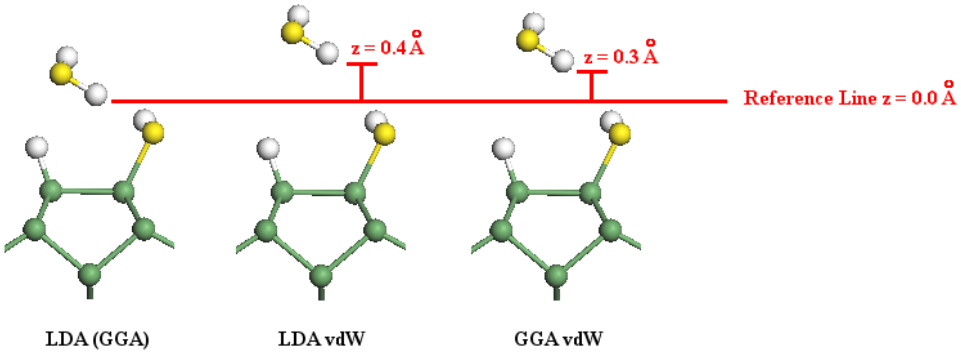


(a)

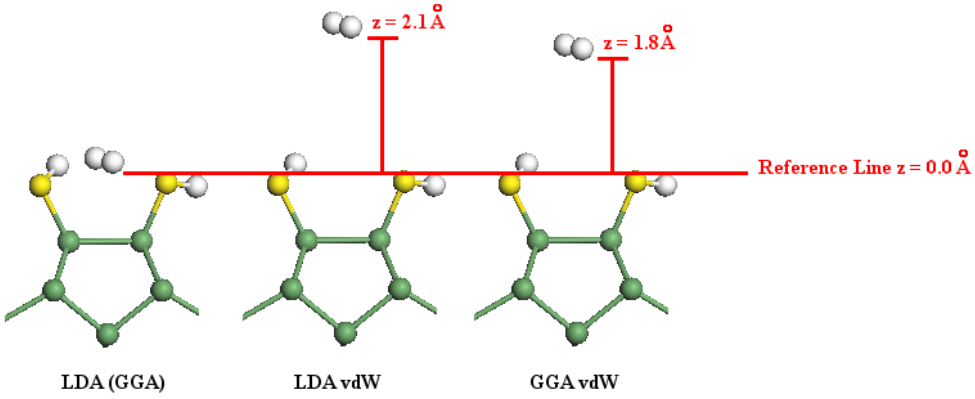


(b)

Figure 4.2: The (a) $H_2S$ and (b) $H_2$ molecule in LDA (GGA) are positioned above the Ge(001)-(2 × 1) surface from Fig. 4.1(c) and Fig. 4.1(d), respectively. A reference line is shown in red. Upon re-relaxing the equilibrium geometry using van der Waals interactions, the $H_2S$ molecule in (a) and the $H_2$ molecule in (b) moves further from the surface in LDA (GGA).

$$F_\alpha(i) = -\Phi_{\alpha\beta}(i,j)d_\beta(j). \tag{4.1}$$

Once the fully relaxed structure (Fig. 4.1(d)) has been obtained for the $H_2S$ on the Ge(001)-$(2\times1)$ surface, we compute the force constant matrix $\Phi_{\alpha\beta}(i,j)$, calculating the Hellman-Feynman forces $F_\alpha(i)$ induced by making a displacement $d_\beta(j)$ of each surface atom in the three orthogonal directions. Displacements at intervals of 0.01 Å from equilibrium were used, up to a maximum of 0.04 Å. A good fit was obtained when the force on each atom $i$ was fitted with a polynomial of order two in the displacement $d_\beta(j)$ and the corresponding element of the force constant matrix $\Phi(i,j)$ was taken as minus the derivative of the fitted force at zero displacement. Diagonalization of the dynamical matrix, $D(i,j) = \Phi(i,j)/\sqrt{m_i m_j}$, where $m_i$ is the mass of atom $i$, results in the eigenvalues $\lambda_k = \omega_k^2$ and the eigenvectors $|u_k\rangle$, which give the relative direction and amplitude of the displacement (scaled by $\sqrt{m_i}$) of each atom $i$ for each vibrational mode. Because we are concerned only with the calculation of localized vibration modes, whose frequency is above the range of the bulk germanium phonon bands, it is not necessary to calculate the full dynamical matrix including all atomic displacements; only motion of the H, S and O atoms and their nearest neighbour Ge atoms are considered. [95] (We find the corrections to the localized mode frequencies due to the nearest neighbour Ge atom recoil are small and corrections [95] for the motion of Ge atoms further into the bulk are negligible.)

We did an initial calculation of the recoil effect with the ABINIT code [85] using the Teter-Pade parameterization [39] of the local density approximation and the pseudopotentials of of Hartwigsen, Goedecker and Hutter for germanium [42] and Troullier and Martins [43] for hydrogen and sulfur. Here we displaced the hydrogen atoms only bonded to the sulfur atoms on the surface and calculated the vibrational mode frequencies as reported in Table 4.2. We repeated the calculation moving the

hydrogen and sulfur surface atoms only and also moving the hydrogen, sulfur and germanium surface atoms only as shown in Table 4.2. We see the S-H stretch mode only varies by 36 $cm^{-1}$ in these three different calculations, the S-H bending mode by 12 $cm^{-1}$, the Ge-S stretch mode by 63 $cm^{-1}$ and the S-H wag mode by 6 $cm^{-1}$. The largest variation here is in the Ge-S stretch, however the correction is still small and all these modes are around the 350 $cm^{-1}$. This provides the evidence that the mode frequencies due to the nearest neighbours recoil are small, thus we are confident that calculating the vibration mode frequencies for the germanium atoms in the bulk is unnecessary.

Table 4.2: Calculated vibrational mode frequencies (in $cm^{-1}$) for $H_2S$ on a Ge(001) surface for the relaxed structures shown in Fig. 4.1(d)

| | | S-H Stretch | S-H Bend | Ge-S Stretch | S-H Wag |
|---|---|---|---|---|---|
| Fig. 4.1(d) | LDA | 2381 | 697 | | 292 |
| (Displace H) | | 2345 | 684 | | |
| Fig. 4.1(d) | LDA | 2417 | 707 | 323 | 295 |
| (Displace H & S) | | 2380 | 695 | 308 | |
| Fig. 4.1(d) | LDA | 2417 | 709 | 393 | 298 |
| (Displace H, S & Ge) | | 2380 | 697 | 384 | |
| | | | | 359 | |

We report the localized vibrational mode frequencies of structures in Fig. 4.1(d) for LDA and GGA, with and without vdW in Table 4.3. For reference, a calculation was carried out to determine the vibrational mode frequencies of an isolated $H_2S$ molecule and compared to the experimental data. [3] The $H_2S$ molecule was placed in a large cubic cell (20 Bohr) and after relaxation using LDA (GGA), produced a S-H bond length of 1.36 Å (1.36 Å) and a bond angle of 91° (91.6°). The calculated bond length is 2% (2%) greater than the experimental value. Upon relaxation, using the vdW correction, LDA (GGA) produced a S-H bond length of 1.35 Å (1.36 Å) and a bond angle of 92.5° (92.6°), which is 1% (2%) greater than the experimental value. The vibrational mode frequencies, given in Table 4.3, were found to be 2545 $cm^{-1}$ (2547) and 2562 $cm^{-1}$ (2565) for the S-H symmetric and anti-symmetric stretch, re-

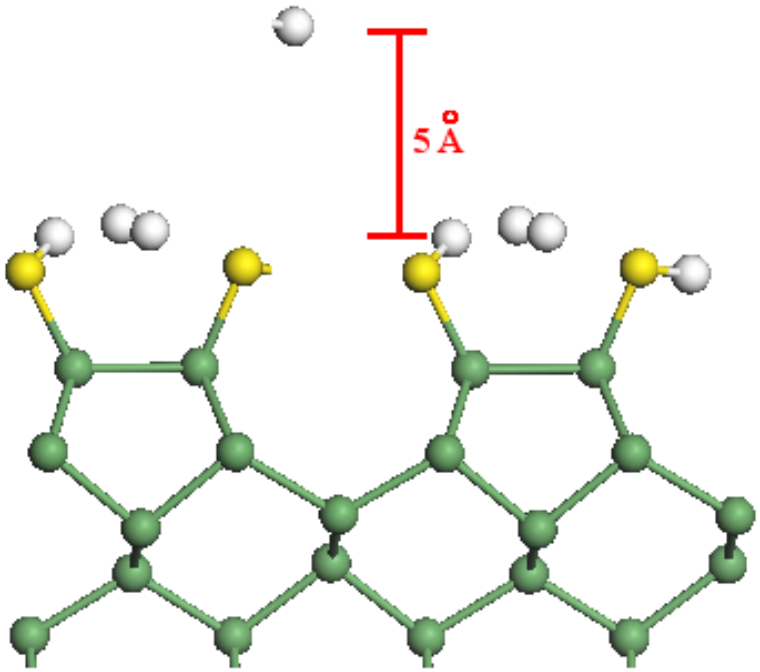


(a)

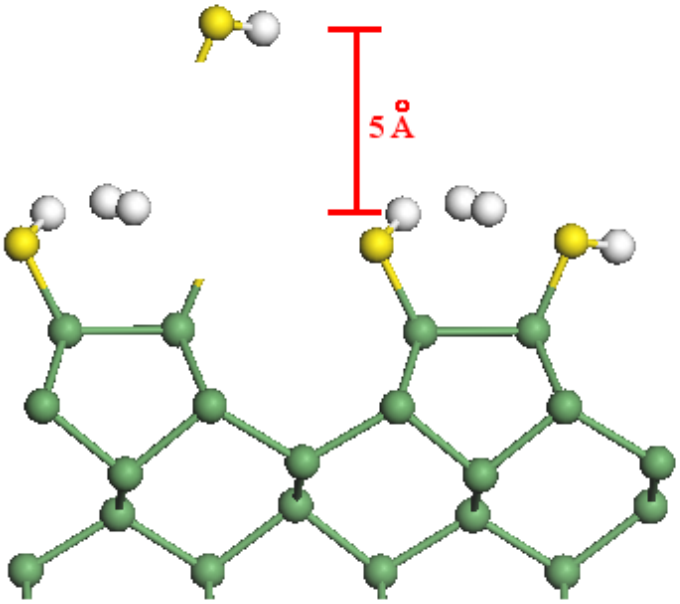


(b)

Figure 4.3: (a) A GeS−H and (b) a Ge−SH bond is broken on the surface and the H and SH atoms are moved respectively, 5 Å from the germanium surface.

Table 4.3: Calculated vibrational mode frequencies (in $cm^{-1}$) for $H_2S$ adsorbed on a Ge(001) surface for the relaxed structure shown in Fig. 4.1(d) and the isolated molecule using both LDA and GGA. Experimental frequencies for $H_2S$ molecule from Ref. [3] are also shown.

| | | S-H Stretch | S-H Bend | Ge-S Stretch | S-H Wag |
|---|---|---|---|---|---|
| Fig. 4.1(d) | LDA | 2438 | 718 | 396 | 328 |
| | | 2419 | 706 | 374 | |
| Fig. 4.1(d) | LDA vdW | 2492 | 748 | 364 | 333 |
| | | 2473 | 736 | 346 | |
| Fig. 4.1(d) | GGA | 2495 | 708 | 373 | 337 |
| | | 2484 | 704 | 353 | |
| Fig. 4.1(d) | GGA vdW | 2481 | 729 | 352 | 315 |
| | | 2469 | 719 | 332 | |
| Molecule | LDA | 2562 | 1117 | | |
| | | 2545 | | | |
| Molecule | LDA vdW | 2541 | 1187 | | |
| | | 2524 | | | |
| Molecule | GGA | 2565 | 1140 | | |
| | | 2547 | | | |
| Molecule | GGA vdW | 2525 | 1179 | | |
| | | 2508 | | | |
| Molecule | Experiment | 2733.4 | 1214.5 | | |
| | | 2721.9 | | | |

spectively, and 1117 $cm^{-1}$ (1140) for the bond bending mode. For LDA (GGA) with vdW interactions, the symmetric and anti-symmetric stretch are 2524 $cm^{-1}$ (2508) and 2541 $cm^{-1}$ (2525) respectively, and a bond bending mode of 1187 $cm^{-1}$ (1179). We see from Table 4.3 that LDA produces stretch and bond bending modes to within 6% and 8% respectively, of experimental values for the $H_2S$ only, while GGA provides a slightly better approximation, with both stretch and bending mode within 6% of experiment. With the vdW interaction, LDA produces a stretch to within 7% of experiment but the bending mode is much improved to be within 2%. Similarly GGA with vdW, overestimates the stretch to 8%, while the bending is closer to the experimental value by 3%. Given that the calculated equilibrium bond lengths are larger than the experimental value in LDA, GGA and vdW cases, it is not surprising that our calculated mode frequencies for the molecule using both LDA and GGA are somewhat less than experiment.

Two different surface sites exist on the $H_2S$ passivated Ge(001)-$(2 \times 1)$ as seen in Fig. 4.1(d), with the frequency difference of 19 $cm^{-1}$ (11) between S-H stretch modes on these two sites. As the modes on the two sites are similar, we averaged the vibrational frequencies. The LDA (GGA) calculated average S-H stretch mode frequency of 2429 $cm^{-1}$ (2490) in the $H_2S$ passivated Ge(001)-$(2 \times 1)$ surface is approximately 125 $cm^{-1}$ (66) less than the stretch mode in isolated $H_2S$ molecule. Thus, bonding to germanium weakens the S-H bond and reduces the mode frequency, consistent with the slightly longer S-H bond 1.38 Å (1.37) following adsorption. In this calculation GGA results in a S-H stretch mode of 61 $cm^{-1}$ greater than LDA, as expected from the smaller S-H bond length in GGA. A comparison of these results with those produced with the vdW interaction, we see a difference in the LDA (GGA) S-H averaged stretch of 54 $cm^{-1}$ (15), which is somewhat less than the difference between LDA and GGA without vdW.

The LDA (GGA) averaged S-H bond bending mode of 712 $cm^{-1}$ (706), is signif-

icantly less than the bond bending mode frequency of 1117 $cm^{-1}$ (1140), calculated for the $H_2S$ molecule. In the isolated molecule, the bond-bending mode involves a symmetric oscillation of both H atoms, resulting in a frequency

$$\omega = \sqrt{\frac{k}{m_{red}}} = \sqrt{\frac{2k}{m_H}} \tag{4.2}$$

where $k$ is the force constant associated with the bond-bending motion and $m_{red} = m_H/2$ is the reduced mass of the two H atoms. When S-H is bonded to Ge on the surface, the bond bending mode involves primarily the motion of the H atom, the amplitude of motion of the heavy Ge atom being much smaller, and the mode frequency is approximately

$$\omega = \sqrt{\frac{k}{m_H}} \tag{4.3}$$

Thus, if the Ge-S-H bonding bending force constant were the same as the H-S-H bending force constant, the bending mode frequency would be a factor of $\sqrt{2}$ smaller for the adsorbed species than for the free $H_2S$ molecule. A reduction of the LDA (GGA) calculated molecular frequency by $\sqrt{2}$ results in a frequency of 790 $cm^{-1}$ (806), 78 $cm^{-1}$ (100) greater than the calculated Ge-S-H bond bending frequency. This indicates slightly softer bond-bending forces for the Ge-S-H bond, compared to the H-S-H, again consistent with the longer S-H bond for the adsorbed species. Both LDA and GGA produce very similar frequencies for the bending mode, despite the fact that GGA produces a better bending mode frequency in the isolated molecule. VdW with LDA (GGA) produces a larger bending mode frequency of 742 $cm^{-1}$ (724), which is consistent with the smaller S-H bond length.

The Ge-S stretch mode at 377 $cm^{-1}$ (363) in LDA (GGA), characterizes the bonding of S to Ge. Since this value lies above the maximum germanium bulk vibration frequency of about 301 $cm^{-1}$ [96], this localized Ge-S stretch mode may be observ-

able in infrared spectroscopy. The inclusion of vdW interactions with LDA (GGA) increases the Ge-S bond length and as expected reduces the stretch mode to 355 $cm^{-1}$ (342). There is no great difference in the vibrational results for LDA, GGA and vdW.

A S-H wag mode of 328 $cm^{-1}$ (337) in LDA (GGA) may also be visible, despite the fact that this mode is near the germanium bulk vibration frequency of about 301 $cm^{-1}$. Similarly in vdW with LDA (GGA), we see such a mode at 333 $cm^{-1}$ (315).

We calculated the localized vibrational mode frequencies also for the structure in Fig. 4.1(c) for LDA and GGA, with and without vdW. We also calculated the vibrational mode frequencies for the structures in Fig. 4.1(c) and Fig. 4.1(d) without the desorbed molecules and all the results are reported in Table A.2 in Appendix A.

To calculate the energies to break the Ge−SH and GeS−H bonds in the relaxed structure (Fig. 4.1(d)), we artificially move the SH and H, respectively, 5 Å from the germanium surface as shown in Fig. 4.3(a) and Fig. 4.3(b). The energy difference between this relaxed structure and the bonded structure in Fig. 4.1(d) is the bond breaking energy for LDA (GGA) calculations. A bond breaking energy of 3.59 eV (3.03) and 4.27 eV (4.02) is required to break the Ge−SH and GeS−H bonds, respectively; an extra 0.68 eV (0.99) is required to break the Ge−SH bond compared to the GeS−H bond. Including vdW with LDA (GGA), an energy of 3.07 eV (2.83) and 3.94 eV (3.80) is required to break the Ge−SH and GeS−H bonds, respectively.

We reported in Table A.1 the total energy per $(2 \times 1)$ supercell for Fig. 4.1(c) and Fig. 4.1(d). Two further calculations were done: first we removed the relevant molecule completely from the supercell, re-relax the structure to calculate a new energy, and secondly we calculate the energy of the molecule on its own in the supercell. These energies are presented also in Table A.1. In LDA, LDA vdw and GGA vdW, the configuration in Fig. 4.1(c) is more stable than the configuration with the $H_2S$ molecule entirely desorbed, while for GGA the opposite is the case. With Fig. 4.1(d), the case where the $H_2$ molecule is removed from the surface is more stable.

Using the same starting Ge(001)-(2 × 1) configuration as shown in Fig. 4.1(d), we replace the $H_2S$ with $H_2O$ [97, 98] and repeat the same structural relaxation as that was performed previously for $H_2S$. Using LDA (GGA) the relaxed structure in Fig. 4.4(b) [99, 100] is much more stable than that of Fig. 4.4(c), with a total energy lower by 0.15 eV (0.32) per (2 × 1) supercell. The more energetically favourable structure for both LDA and GGA, Fig. 4.4(b), produces a Ge-O-H and Ge-H configuration consistent with that of Jung *et al.* [89]. However with the inclusion of the vdW interaction, LDA produces the stable structure (Fig. 4.4(b)) with a total energy lower by 0.07 eV, while GGA results in Fig. 4.4(c) being the more stable geometry by 0.1 eV. A comparison of the bond lengths for LDA, GGA, vdW, experimental values and calculated covalent radii are presented in Table 4.4 for the $H_2O$ passivated Ge(001)-(2 × 1) surfaces.

Table 4.4: Calculated bond lengths (in Å) for $H_2O$ on a Ge(001) surfaces for the LDA, GGA and vdW relaxed structures shown in Fig. 4.4(b) and Fig. 4.4(c). Experimental bond length and calculated covalent radii from [a]Ref. [1] and [b]Ref. [2] are given.

| | | LDA | LDA vdW | GGA | GGA vdW | Expt | Cov Radii |
|---|---|---|---|---|---|---|---|
| Ge-O | Fig 4.2(b) | 1.80 | 1.79 | 1.86 | 1.87 | | 1.95[a] |
| Ge-H | Fig 4.2(b) | 1.53 | 1.50 | 1.54 | 1.53 | | 1.59[a] |
| Ge-Ge dimer | Fig 4.2(b) | 2.46 | 2.50 | 2.53 | 2.57 | 2.45[b] | 2.44[a] |
| H-O | Fig 4.2(b) | 0.98 | 0.97 | 0.98 | 0.98 | | 1.10[a] |
| H-O molecule | Fig 4.2(b) | 1.00 | 0.98 | 0.99 | 0.98 | | 1.10[a] |
| Ge-O | Fig 4.2(c) | 1.77 | 1.78 | 1.84 | 1.85 | | 1.95[a] |
| Ge-Ge dimer | Fig 4.2(c) | 2.48 | 2.53 | 2.56 | 2.60 | 2.45[b] | 2.44[a] |
| H-O | Fig 4.2(c) | 0.99 | 0.97 | 0.98 | 0.98 | | 1.10[a] |
| H-H molecule | Fig 4.2(c) | 0.78 | 0.73 | 0.75 | 0.73 | | 0.74[a] |

The localized mode frequencies for the structures shown in Fig. 4.4(b) and Fig. 4.4(c) are given in Table 4.5.

A reference calculation for the $H_2O$ molecule gave a H-O bond length of 0.98 Å (0.97 Å) which is 2% (1%) greater than the experimental value. The vibrational mode frequencies for LDA (GGA) were found to be 3602 $cm^{-1}$ (3602), 3713 $cm^{-1}$ (3709) and 1581 $cm^{-1}$ (1624) for the symmetric, anti-symmetric and bond bending modes. In these reference calculations, despite the greater LDA H-O bond length,

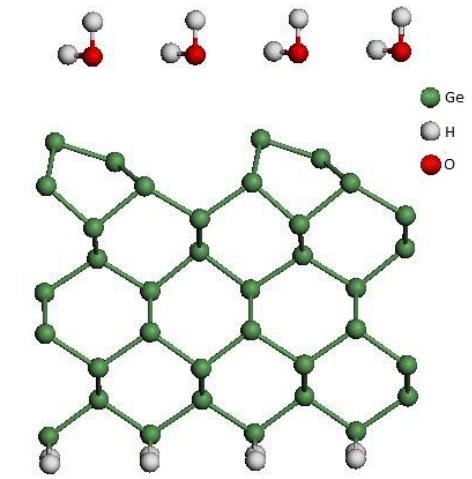


(a)

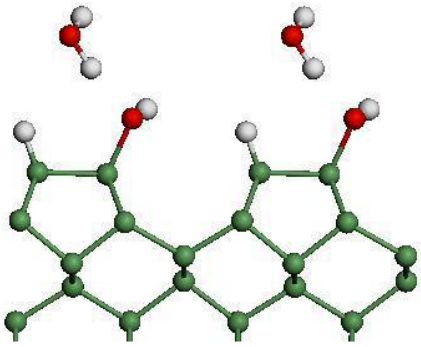

(b)

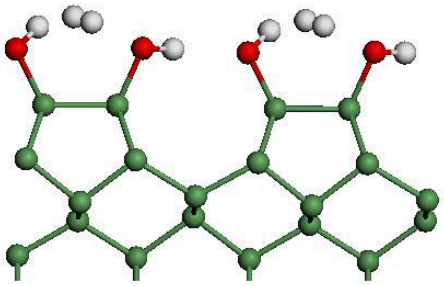

(c)

Figure 4.4: (a) Initial atomic configuration of the Ge(001)-$(2 \times 1)$ surface exposed to $H_2O$. (b) After structural relaxation one $H_2O$ is adsorbed onto the surface with the formation of a Ge-O-H and Ge-H bonds. (c) Artificial breaking of the Ge-H bond allows another $H_2O$ molecule to be adsorbed onto the surface. The resulting structure in (c) is less stable than that in (b).

Table 4.5: Calculated LDA and GGA vibrational mode frequencies (in $cm^{-1}$) for $H_2O$ on a Ge(001) surface for the relaxed structures shown in Fig. 4.4(b) and Fig. 4.4(c) and for the isolated molecule. Experimental frequencies for $H_2O$ molecule from Ref. [3] are also shown.

| | | H-O Stretch | H-O Bend | Ge-H Stretch | Ge-H Bend | Ge-O Stretch | H-O Wag |
|---|---|---|---|---|---|---|---|
| Fig. 4.2(b) | LDA | 3590 | 921 | 1995 | 538<br>455 | 609 | 342 |
| Fig. 4.2(b) | LDA vdW | 3583 | 947 | 2067 | 543<br>531 | 621 | |
| Fig. 4.2(b) | GGA | 3600 | 940 | 1991 | 486<br>469 | 559 | 336 |
| Fig. 4.2(b) | GGA vdW | 3552 | 951 | 2000 | 504<br>483 | 579<br>538 | 401 |
| Fig. 4.2(c) | LDA | 3593<br>3498 | 984<br>909 | | | 677<br>654 | 381 |
| Fig. 4.2(c) | LDA vdW | 3557<br>3555 | 972<br>937 | | | 652<br>612 | 347 |
| Fig. 4.2(c) | GGA | 3577<br>3575 | 969<br>942 | | | 621<br>586 | 340 |
| Fig. 4.2(c) | GGA vdW | 3548<br>3524 | 970<br>942 | | | 587<br>537 | 362 |
| Molecule | LDA | 3713<br>3602 | 1581 | | | | |
| Molecule | LDA vdW | 3677<br>3573 | 1635 | | | | |
| Molecule | GGA | 3709<br>3602 | 1624 | | | | |
| Molecule | GGA vdW | 3624<br>3584 | 1591 | | | | |
| Molecule | Experiment | 3942.5<br>3833.2 | 1648.5 | | | | |

both LDA and GGA provide very similar stretching modes, while GGA results in a more accurate bond bending mode frequency. With the vdW interactions, the $H_2O$ molecule gave a H-O bond length of 0.98 Å (0.98 Å) which is 2% (2%) greater than experiment. The corresponding LDA (GGA) frequencies were found to be 3573 $cm^{-1}$ (3584), 3677 $cm^{-1}$ (3624) and 1635 $cm^{-1}$ (1591) for the symmetric, anti-symmetric and bond bending modes. VdW produces results here that are less accurate, compared to the experimental values for the stretch modes, while LDA bending mode frequency is almost identical to experiment.

In LDA (GGA) the H-O stretch mode is about 120 $cm^{-1}$ (109) less than the isolated molecule stretch mode, a shift very similar to that found for the H-S stretch. This, despite the fact that the O-H bond length of 0.98 Å (0.98 Å) in the adsorbed species is the same as in the molecule. The LDA vdW produces a H-O stretch mode of 3583 $cm^{-1}$, 7 $cm^{-1}$ less than the LDA mode without vdW. However, the bond bending mode of 921 $cm^{-1}$ (940) is 196 $cm^{-1}$ (208) smaller than $1581/\sqrt{2} = 1117$ $cm^{-1}$ (1148), the frequency we should expect if the Ge-O-H bending force constant were the same as the H-O-H constant, indicating a substantially softened O-H bond in the absorbed species. Similarly with vdW, the bending mode of 947 $cm^{-1}$ is 209 $cm^{-1}$ smaller than the expected value of 1156 $cm^{-1}$.

A Ge-O stretch mode is reported at 609 $cm^{-1}$ (559), which characterizes the bonding of O to Ge. A slightly higher mode is produced from vdW at 653 $cm^{-1}$, again consistent with the shorter Ge-O bond length.

The presence of the Ge-H stretch mode distinguishes the equilibrium surface in Fig. 4.4(b) from the equilibrium surface in in Fig. 4.4(c), with the LDA (GGA) stretch mode reported at 1995 $cm^{-1}$ (1991). A Ge-H bond bending mode is seen at 498 $cm^{-1}$ (478). With the vdW interaction, the Ge-H stretch is higher at 2067 $cm^{-1}$ and the bending mode at 537 $cm^{-1}$. No large differences are seen between the LDA, GGA and LDA vdw vibrational frequencies for the surfaces except for the Ge-H stretch

mode, where LDA vdw is 72 $cm^{-1}$ higher.

For the relaxed GGA vdW surface (Fig. 4.4(c)), we report a H-O stretch of 3536 $cm^{-1}$, H-O bending of 956 $cm^{-1}$ and a Ge-O stretch of 562 $cm^{-1}$.

The same procedure as discussed earlier in this chapter which is shown in Fig. 4.3(a) and Fig. 4.3(b) followed for $H_2S$ is repeated to calculate the bond breaking energies for the $H_2O$ passivated Ge(001)-$(2 \times 1)$ surface (Fig. 4.4(b)). In LDA (GGA) an energy of 4.88 eV $(4.11)$ is required to break the Ge$-$OH bond, 5.30 eV $(5.08)$ for the GeO$-$H and 3.94 eV $(3.73)$ for Ge$-$H. In vdW, LDA (GGA) require an energy of 4.47 eV $(4.11)$ is required to break the Ge$-$OH bond, 4.93 eV $(4.86)$ for the GeO$-$H and 3.9 eV $(3.69)$ for Ge$-$H. The difference between the bond breaking energies of Ge$-$OH bond and GeO$-$H is 0.42 eV $(0.97)$, and in vdW, 0.46 eV $(0.75)$, indicating in both cases of the $H_2S$ and the $H_2O$ bonded to the germanium surface, the H$-$S and H$-$O bonds are stronger than the Ge$-$SH and Ge$-$OH. The Ge$-$H bond being the weakest bond on this $H_2O$ passivated germanium surface.

We report the total energy per $(2 \times 1)$ supercell for Fig. 4.4(b) and Fig. 4.4(c) in Table A.1 . For Fig. 4.4(b) the original case where the $H_2O$ molecule is near the surface is energetically favourable, while for structure Fig. 4.4(c), a mixture of both the $H_2$ molecule close to the surface and completely removed exist.

Vibrational mode frequency calculations were repeated for all $H_2S$ and $H_2O$ adsorbed on Ge(001)-$(2 \times 1)$ surfaces with the desorbed molecule removed from the calculation, and are reported in Table 4.3 and Table 4.5. The difference in the vibrational frequencies with the molecules removed only affects the results by a few wavenumbers.

## 4.4 Conclusions

In conclusion, we see both similarities and differences in the bonding of $H_2S$ and $H_2O$ to the Ge(001)-$(2 \times 1)$ surface. The differences between the exchange-correlation functionals including vdW terms and the LDA or GGA are less than the differences between LDA and GGA, thus vdW does not greatly alter the vibrational mode frequencies. Two distinct absorption sites of H-S exist for the more stable $H_2S$ structure, whereas only one is present for OH in the stable (LDA, GGA and LDA vdW) $H_2O$ structure. The bond bending mode for the adsorbed $H_2S$ is of the order of $\sqrt{2}$ of the bond-bending frequency in the free molecule, while the corresponding modes of the $H_2O$ is considerably less, indicating a much greater weakening of bonding bending forces. These calculated localized mode frequencies, particularly the Ge-S and Ge-O stretch modes, provide useful vibrational signatures of bonding of both sulfur and oxygen on Ge(001)-(2x1) surface, which may be compared with vibrational spectroscopy measurements. The Ge-H stretch and bending modes are characteristic in identifying the difference between the two $H_2O$ to the Ge(001)-$(2 \times 1)$ surfaces (Fig. 4.4(b) and Fig. 4.4(c)).

CHAPTER 5

# Ge-Si Interfaces

*The structural and electronic characteristics of a Ge-Si(001) interface are calculated in a supercell approach using first-principles density functional theory in the local density approximation (LDA) for regions where the germanium and silicon atoms align and misalign. Self-consistent calculations determine the atomic structure and the band lineup of the germanium and silicon band structures. Projected band structure calculations show the existence of interface states in the band gap.*

## 5.1 Introduction

In this chapter we are investigating a theoretical approach to the wafer bonding of germanium to silicon, which is the pressing together of a wafer of germanium to a wafer of silicon using force, to create a bond between the two wafers. One problem with this is the mismatch in the lattice constant. If the germanium matches the silicon well in some regions, which we define as the lattices aligned, then they will match poorly in neighbouring regions, which we define as the lattices are misaligned. Both the aligned and misaligned regions of the interface are shown in Fig. 5.1. The aligned regions imply that the germanium atoms lie in the same vertical plane as the silicon atoms where we expect no broken bonds, thus leading to good mechanical and elec-

trical characteristics. The misaligned regions imply the silicon atoms do not lie in the same vertical plane as the germanium atoms and we expect such regions of misalignment to result in broken bonds and interface states, thus leading to poor mechanical contact and electrical transmission characteristics.

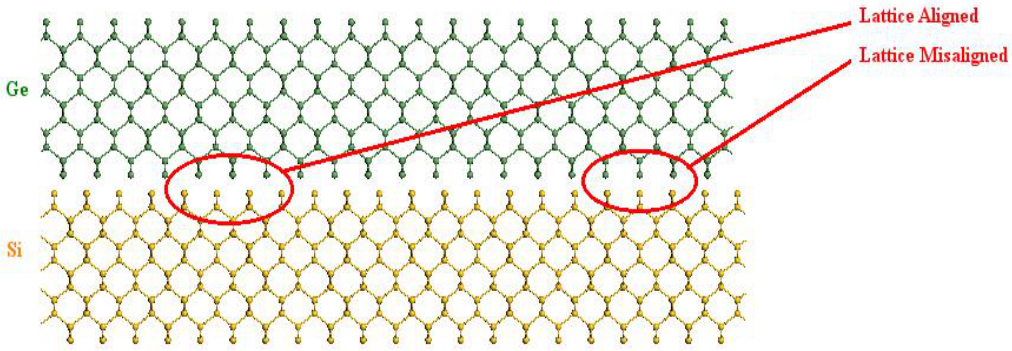


Figure 5.1: The GeSi interface showing the regions where the germanium and silicon interface atoms are aligned and misaligned.

With the lattice constant of germanium being about 4 % larger than silicon, we would require a calculation of a $(30 \times 30)$ size supercell to represent the regions of going from alignment to misalignment. However, such a supercell is too large for us to calculate using density functional theory so we investigate the best and worst case scenarios only, that being the region of perfect alignment and complete misalignment, respectively. We expect the region of lattice alignment to show a good interface, meaning good chemical bonds and no interface states, while in the region of misalignment we expect to see an interface reconstruction in order to adjust the bonding at the interface and also the presence of interface states due to dangling bonds.

An important point must be made here with regard to all calculations. As the calculations involve a supercell approach using a first-principles density functional theory calculation, we need to choose the size of the lattice for the supercell. It is simply not possible to run a calculation with a germanium bulk wafer bonded to a silicon bulk and have the lattice constants of both being used in the structural relaxation and electronic

properties. We run all calculations for the structural relaxation and electronic properties such as projected band structures, potential energy and charge density first using the germanium lattice constant and we repeat all these calculations with the silicon lattice constant. From this we expect the true wafer bonded results for both structural and electronic properties lay somewhere between the result of using the germanium and silicon lattice constants.

## 5.2 Method of Calculation

In our calculations the interfaces are represented in a supercell geometry [29]. Structural total energies and atomic forces are calculated using first-principles density functional theory [85]. We use the Teter-Pade parameterization [101] of the local density approximation. We use the ABINIT [85] code to calculate the ground state energies. We use the pseudopotentials of Hartwigsen, Goedecker and Hutter for germanium [42] and Troullier and Martins [43] for hydrogen and silicon. The plane-wave cutoff energy was set at 20 Ha. The method of special k-point generation is based on the Monkhorst-Pack [41] scheme. We have used a 32 k-point mesh for all supercells considered.

The germanium slab is modelled using a nine-layer periodic slab of germanium atoms. The bottom surface is terminated with hydrogen atoms to represent the underlying bulk. Silicon is modelled in the same way as germanium and is placed over the germanium slab as shown in Fig. 5.2(a). In the aligned case the GeSi interface is represented using a $(1 \times 1)$ supercell geometry, with one atom per layer in the germanium and silicon layers, implying a total of 22 atoms (9 germanium, 9 silicon and 4 hydrogen). The misaligned case is represented using a $(2 \times 1)$ supercell geometry. Each germanium and silicon atomic layer has 2 atoms per layer, giving a total of 44 atoms per supercell (18 germanium, 18 silicon and 8 hydrogen). For the silicon lattice

to be misaligned with germanium, the silicon slab is shifted so that the silicon atoms do not lie in the same vertical plane as the germanium atoms, as shown in Fig. 5.2(c).

The supercell has a vacuum layer of 18 Å. The lattice constant is held fixed at the calculated equilibrium value of 5.58 Å for bulk germanium, which is about 1% smaller than the experimental value of 5.65 Å. We also relaxed the aligned and misaligned structures using the lattice constant of silicon, at the calculated value of 5.41 Å which is about 0.4% smaller than the experimental value of 5.43 Å. Structures are optimised until the residual HF forces are less than 0.026 eV/Å and all interfaces are relaxed with atomic forces using the Broyden method as described in the paper by Schlegel [86]. The atoms on the three atomic layers on both sides of the GeSi interface as shown in Fig. 5.2(a) and Fig. 5.2(c) are only allowed to relax. All the other atoms in the GeSi slab are held fixed in position to represent the underlying bulk. This method of confining the relaxation was tested in the Ge(001)-$(2 \times 1)$ surface where all atomic layer were relaxed and only the top three layers were involved in the surface reconstruction. With the relaxation confined to these layers near the interface in both slabs, the structure is allowed to relax. After relaxation the silicon slab is brought closer to the germanium slab, thus reducing the interface separation and the interface is allowed to relax again as before. This process is continued until a minimum energy is found for the supercell, which gives the final relaxed geometry.

## 5.3 Interface using the Germanium Lattice Constant

### 5.3.1 Structural Relaxation

On relaxation using the lattice constant for germanium for our GeSi supercell, the GeSi aligned interface results in a GeSi(001)-$(1 \times 1)$ structure, with a Ge-Si bond length of 2.39 Å as shown in Fig. 5.2(b). The relaxed GeSi mismatched lattice re-

sults in a GeSi(001)-$(2 \times 1)$ reconstructed interface as shown in Fig. 5.2(d), with the presence of alternating 5-fold and 7-fold rings in the mismatched regions to adjust the bonding at the interface. This bonding region has a Ge-Ge and Si-Si symmetric dimer bond length of 2.43 Å and 2.50 Å respectively, and a Ge-Si bond length of 2.41 Å.

### 5.3.2 Band Lineup

A fundamental problem in deriving band lineups at interfaces is that for a bulk solid there is no intrinsic zero of energy to which all energies are referred [102], and therefore there exists no unique reference to compare the potentials of two different solids. In order to derive the potential shift which occurs at the interface of germanium and silicon, we perform a calculation where the average local potential $\overline{V}_{loc}(z)$ is given as

$$\overline{V}_{loc}(z) = \int V(\mathbf{r}) dxdy \tag{5.1}$$

where the variation of space coordinate $\mathbf{r}$ is limited to the perpendicular component $z$ to the interface and the potential is averaged over the parallel components $x$ and $y$. The local potential is the total Kohn-Sham potential which is defined as the sum of the local pseudopotential, the Hartree potential and the exchange-correlation potential. The local potential of the GeSi aligned and misaligned slab interfaces are presented in Fig. 5.3(a) and Fig. 5.3(b), respectively.

In the regions far from the interface, the slab structure returns to the properties of the bulk. We averaged the potential over a fixed number of repetitions (6 in the aligned slab and 3 in the misaligned slab) in the bulk-like regions to get the average local potential levels $\overline{V}_{Ge}$ and $\overline{V}_{Si}$. The potential shift

$$\Delta\overline{V} = \overline{V}_{Ge} - \overline{V}_{Si}, \tag{5.2}$$

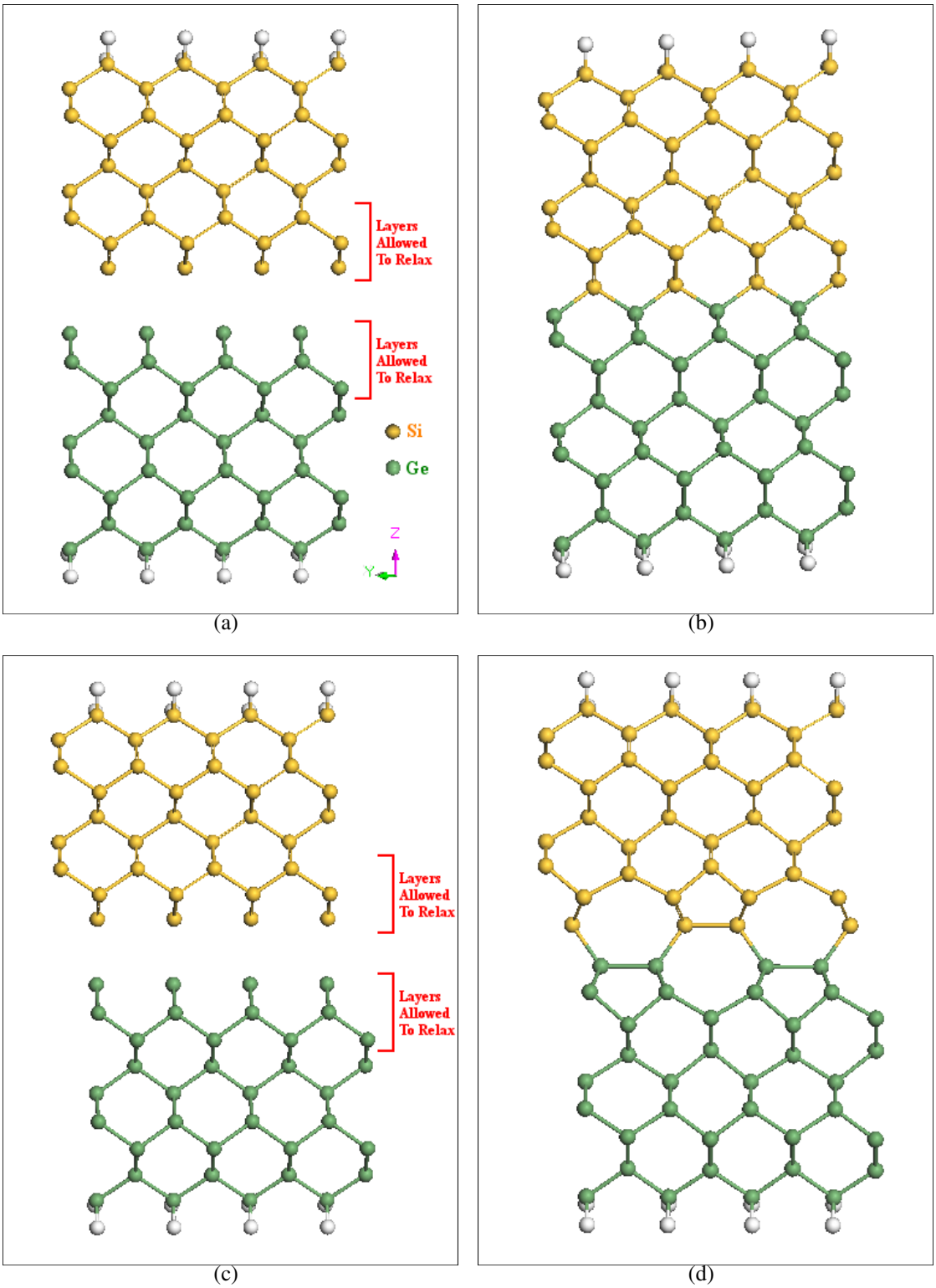


Figure 5.2: (a) The initial atomic configuration of the GeSi aligned structure. (b) After structural relaxation a GeSi(001)-$(1 \times 1)$ is produced. (c) The initial atomic configuration of the GeSi misaligned structure. (d) The final relaxed geometry results in a GeSi(001)-$(2 \times 1)$ interface.

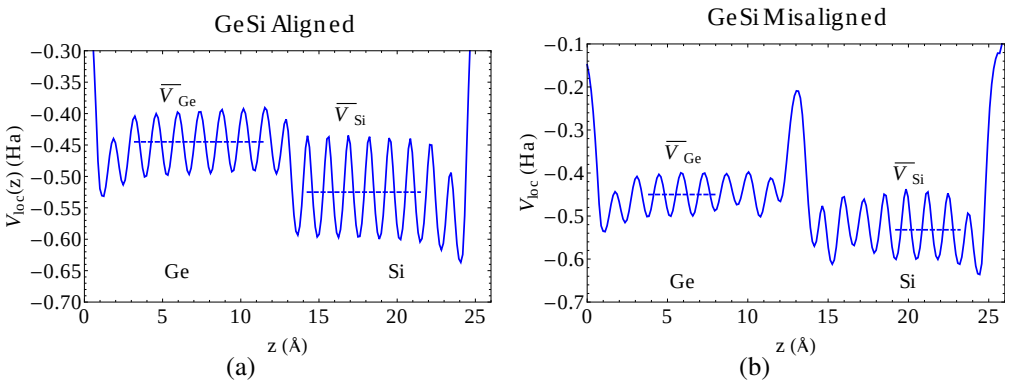


Figure 5.3: The local potential $\overline{V}_{loc}(z)$ averaged over the parallel components $x$ and $y$ as a function of the perpendicular coordinate $z$, to the interface for (a) the aligned and (b) misaligned GeSi interface. The dashed line in both the germanium and silicon is represented as $\overline{V}_{Ge}$ and $\overline{V}_{Si}$, respectively, defined as the average local potential over six periodic potential cycles in (a) and three in (b) in each section of the slab.

is defined as the difference in the average local potential level of germanium and silicon in the interface slab and is illustrated in Fig. 5.4. This potential shift $\Delta\overline{V} = 2.16$ eV for the aligned interface and $\Delta\overline{V} = 2.23$ eV for the misaligned interface.

In order to derive the values for the band lineups, we need to calculate the average local potential as a function of the perpendicular coordinate for both bulk germanium and silicon as we did with the GeSi interface slab. This averaged bulk germanium potential is aligned with that of the bulk-like germanium potential section in the slab as shown in Fig. 5.9(a) and Fig. 5.9(c) for the aligned and misaligned slabs. A curve fitting procedure is applied to both potential curves over three periodic potential cycles. Second order polynomials are fitted to the curves in the potential plots and polynomials of order one are fitted to the linear parts of the potential plots as shown in Fig. 5.5. The energy difference between the bulk and slab germanium is taken in intervals of $\Delta z = 0.01$ Å along the perpendicular coordinate $z$ and the averaged energy difference is denoted as $\Delta E_i$ where $i$ represents germanium or silicon.

$$\Delta E_i = \overline{V}_{loc}(z)|_{i,bulk} - \overline{V}_{loc}(z)|_{i,slab}. \tag{5.3}$$

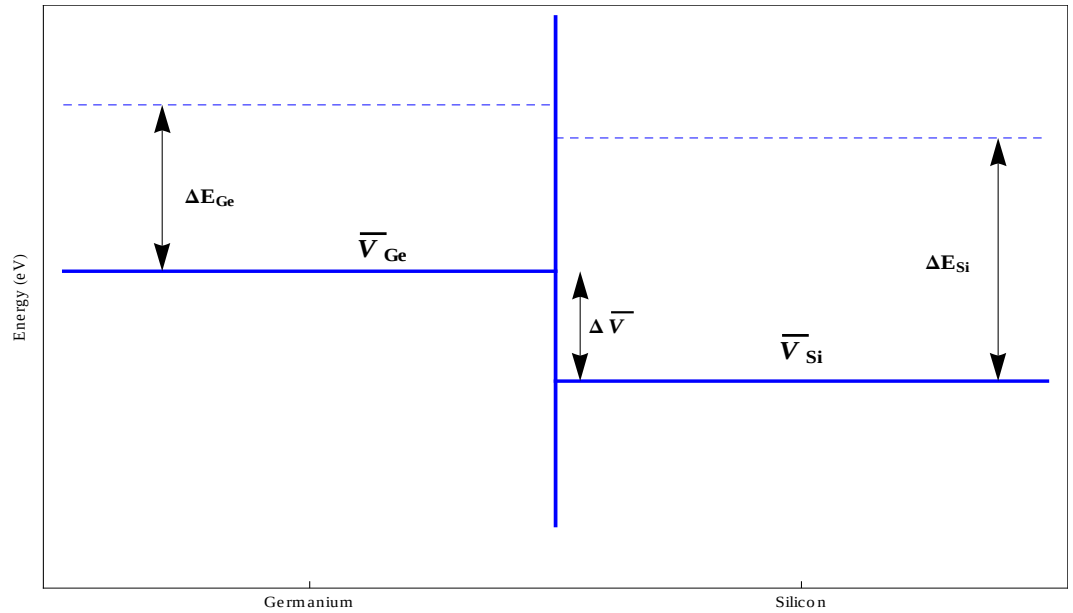


Figure 5.4: Derivation of band lineups: relative position of the average potentials $\overline{V}_{Ge}$ and $\overline{V}_{Si}$ and of the germanium and silicon bulk bands. The dashed lines are the average potentials of bulk materials.

We define an error associated to this energy difference $\delta(\Delta E_i)$ as half the difference between the maximum and minimum energy difference.

$$\delta(\Delta E_i) = \frac{1}{2}(\Delta E_{i,max} - \Delta E_{i,min}). \tag{5.4}$$

The results for $\Delta E_{Ge}$ are shown in Table 5.1 and illustrated in Fig. 5.4.

However, we are faced with a problem with regard to looking at aligning the potentials in silicon. Upon relaxation of the GeSi slab interface using the germanium lattice constant, the silicon atoms strain in order to match the germanium atoms in the parallel interface plane. This stretching of the atoms also causes the silicon atoms in the perpendicular direction to compress, resulting in a reduced slab thickness. Before we proceed to calculate the energy separation in the silicon side of the interface, we need to address how the strain affects bulk silicon and its band structure.

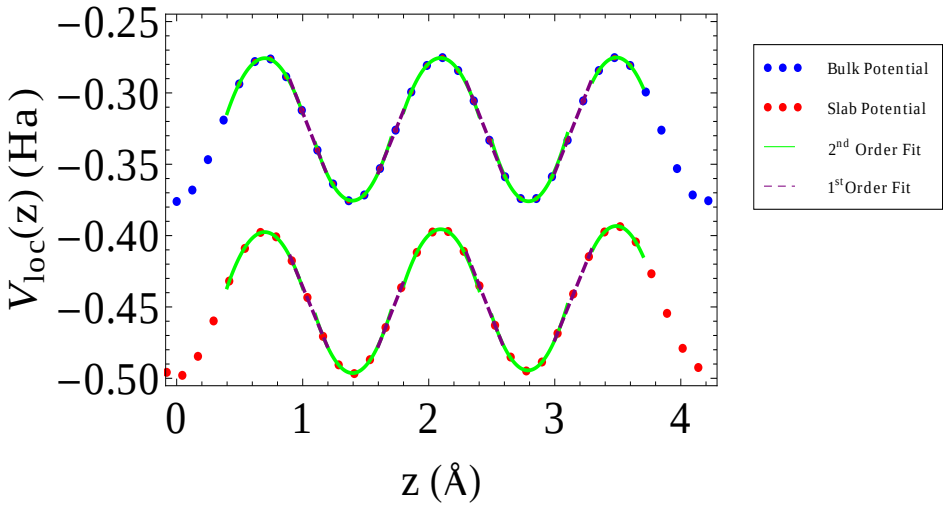


Figure 5.5: The averaged local potentials for the bulk (blue) and corresponding region of the GeSi slab (red) as a function of the perpendicular coordinate $z$. The green line represents the second order polynomial fit to the bulk and slab averaged local potential data and the purple dashed line is the first order polynomial fit.

#### 5.3.2.1 Strain

In order to investigate and understand the strain in this interface, we look at the relaxed geometry atomic layer separation in the both the germanium and strained silicon sides of the slab structure. The layer separation $d_i$ is defined as $d_i = z_{atom_{i+1}} - z_{atom_i}$, which is the difference in the perpendicular coordinate $z$, of the atoms in one atomic layer to the atomic layer directly below it, as shown in Fig. 5.6. The separation $d_1$ is the difference in length of the perpendicular component of the germanium atom in the second atomic layer ($z_{Ge_2}$) with the perpendicular component of the germanium atom in the first atomic layer ($z_{Ge_1}$). We calculate this atomic layer separation as a function of the perpendicular coordinate $z$ as shown in Fig. 5.7(a) and Fig. 5.7(b) for the germanium and strained silicon sides of the interface slab respectively.

The interface in these plots is located in the region from 12 Å to 16 Å. In Fig. 5.7(a) we see the germanium layer separation in the (001) direction ($z$-direction) in the bulk (from 4 Å to 10 Å) matches well to the theoretical value of 1.39 Å as derived from the

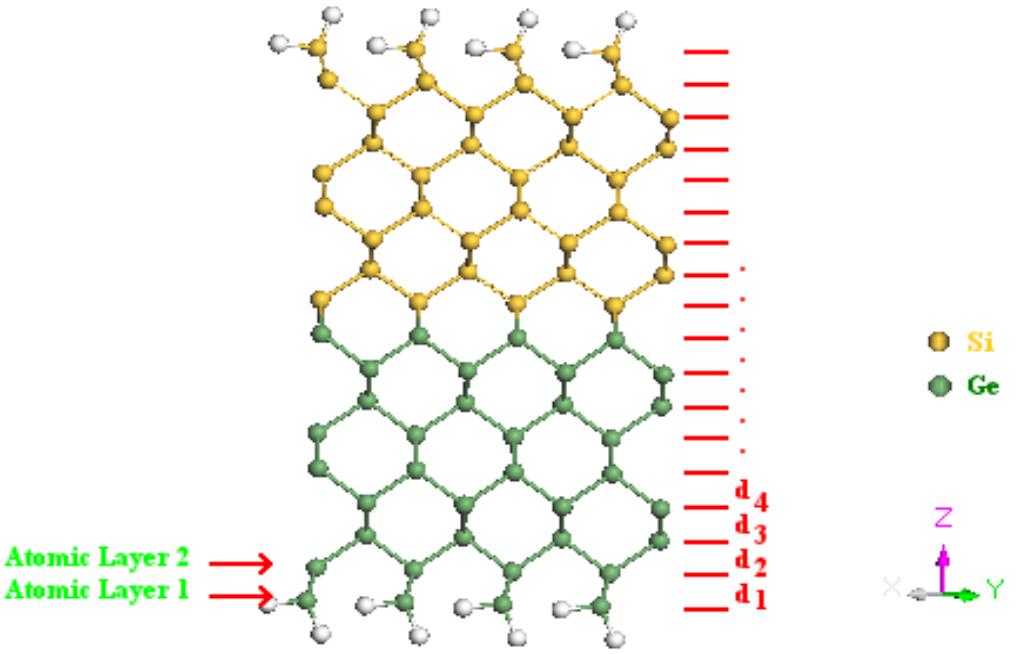


Figure 5.6: The GeSi interface slab shows the layer separations $d_1, d_2, ....$, where the layer separation $d_1$ is defined as the difference in the perpendicular coordinate $z$ of the germanium atoms in atomic layer two and atomic layer one, given by $d_1 = z_{Ge_2} - z_{Ge_1}$.

layer separation for germanium of $\frac{a_{Ge}}{4}$, where $a_{Ge} = 5.58$ Å is the lattice vector of germanium. Silicon is strained so that it matches the germanium lattice in the interface plane (x and y components) and this leads to the compression of the respective layers in the perpendicular direction. We optimise the lattice parameter in the perpendicular direction using the Abinit code. Here in this calculation we set the parallel components of the lattice vectors of strained silicon to be equal to the lattice constant of bulk germanium and allow the cell to be optimised only in the perpendicular direction. The lattice vector calculated from this optimization for strained silicon in this perpendicular $z$ direction is $a_{Si,strained} = 5.25$ Å. This results in silicon matching the germanium atoms in the parallel interface plane causing a strain of about 3.1%, while the silicon cell size is reduced in the perpendicular direction by about 3% from 5.41 Å to 5.25 Å. As the layer separation $d = \frac{a}{4}$, where $a$ is the lattice constant, the layer separation

for strained silicon is now derived to be 1.31 Å. In Fig. 5.7(b) we see that this layer separation value of 1.31 Å represented by the green line coincides with the layer separation of the strained silicon side of the interface slab represented by the blue line (in the region from 16 Å to 23 Å). The layer separation for unstrained bulk silicon is shown in red in Fig. 5.7(b). This allows one to see the $z$ interlayer compression of strained silicon. Similarly for the misaligned GeSi interface we see in Fig. 5.7(c) and Fig. 5.7(d) the layer separation of the bulk regions in the slab match well to the predicted layer separation values.

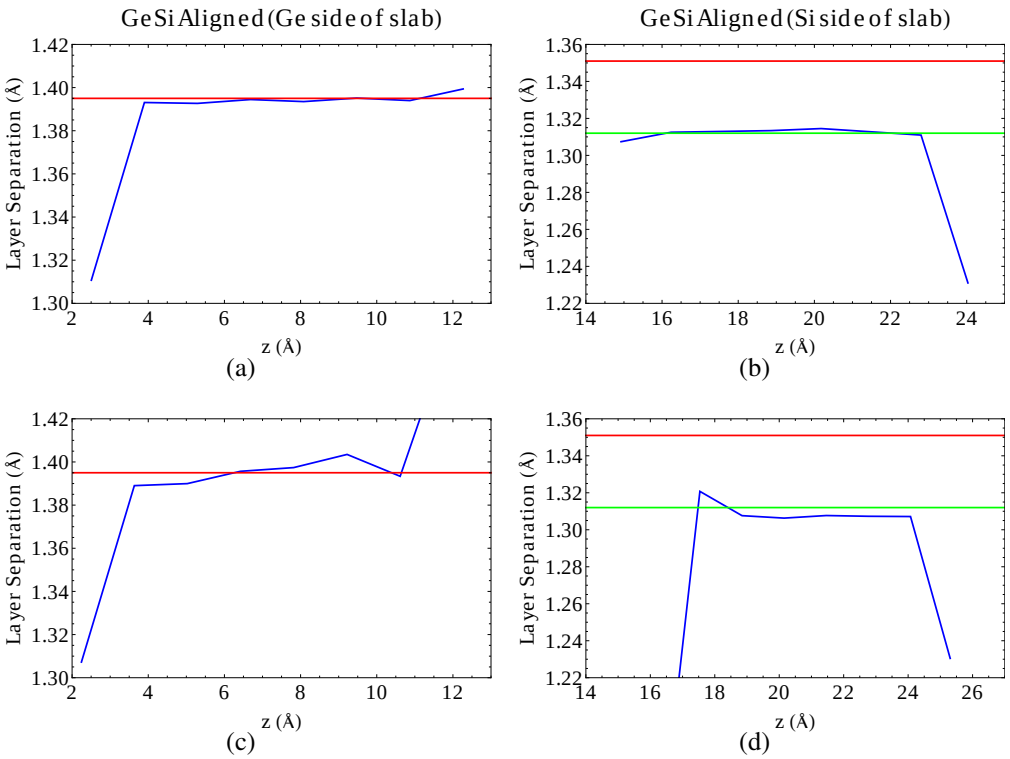


Figure 5.7: Atomic layer separation $d$ (blue line) in the relaxed GeSi slab as a function of position $z$ perpendicular to the plane of the interface. The region with $z < 13$ Å [in (a) and (c)] is unstrained germanium and the region with $z > 14$ Å [in (b) and (d)] is silicon with the in-plane lattice constant matched to unstrained germanium. Panels (a) and (b) show results for the "aligned" interface geometry and panels ( c) and (d) show results for the "misaligned" geometry. The red lines indicate the corresponding unstrained bulk layer separation and the green line indicates the $z$ interlayer separation found in bulk silicon, when its $x-y$ lattice constant is constrained to match that of unstrained germanium (see main text).

To further investigate the effects of strain, band structure calculations for the bulk materials of cubic germanium and strained silicon are done to see what effects this strain has on the electronic bands and the band gap. It must be pointed out here that the theoretical local density approximation band gaps in each material do not agree with experiment. This is a well-known problem that the band gaps of semiconductor materials are severely underestimated, while the topology of all the bands in germanium and silicon is generally good.

The reduced coordinates (in the primitive reciprocal lattice basis) for the high symmetry points in the Brillouin zone of the face centred cubic structure are given as:

$$L = (0.5, 0.0, 0.0), \tag{5.5}$$

$$\Gamma = (0.0, 0.0, 0.0), \tag{5.6}$$

$$X = (0.0, 0.5, 0.5), \tag{5.7}$$

$$\Gamma = (1.0, 1.0, 1.0) \tag{5.8}$$

The band structure calculation for bulk germanium results in a band gap of 0.26 eV as shown in Fig. 5.8(a) moving along the path $L\Gamma XL$, while in strained silicon, the band gap is 0.42 eV as shown in Fig. 5.8(b) going from $\Gamma(0.0, 0.0, 0.0)$ to $X(0.0, 0.5, 0.5)$. However when we move along the $\Delta$ line from $\Gamma(0.0, 0.0, 0.0)$ to $X(0.5, 0.5, 0.0)$ the band gap reduces to -0.13 eV as shown in Fig. 5.8(c). In this case, the minimum of the conduction band along the $\Delta$ line is much lower than in the unstrained case. In Fig. 5.8(d) and Fig. 5.8(e), we superimpose the strained silicon case using $X(0.0, 0.5, 0.5)$ and $X(0.5, 0.5, 0.0)$, respectively over the unstrained silicon band structure.

As mentioned earlier in Section 5.3.2 the procedure for the lineup of the bulk germanium potential with the potential of the germanium side of the interface slab,

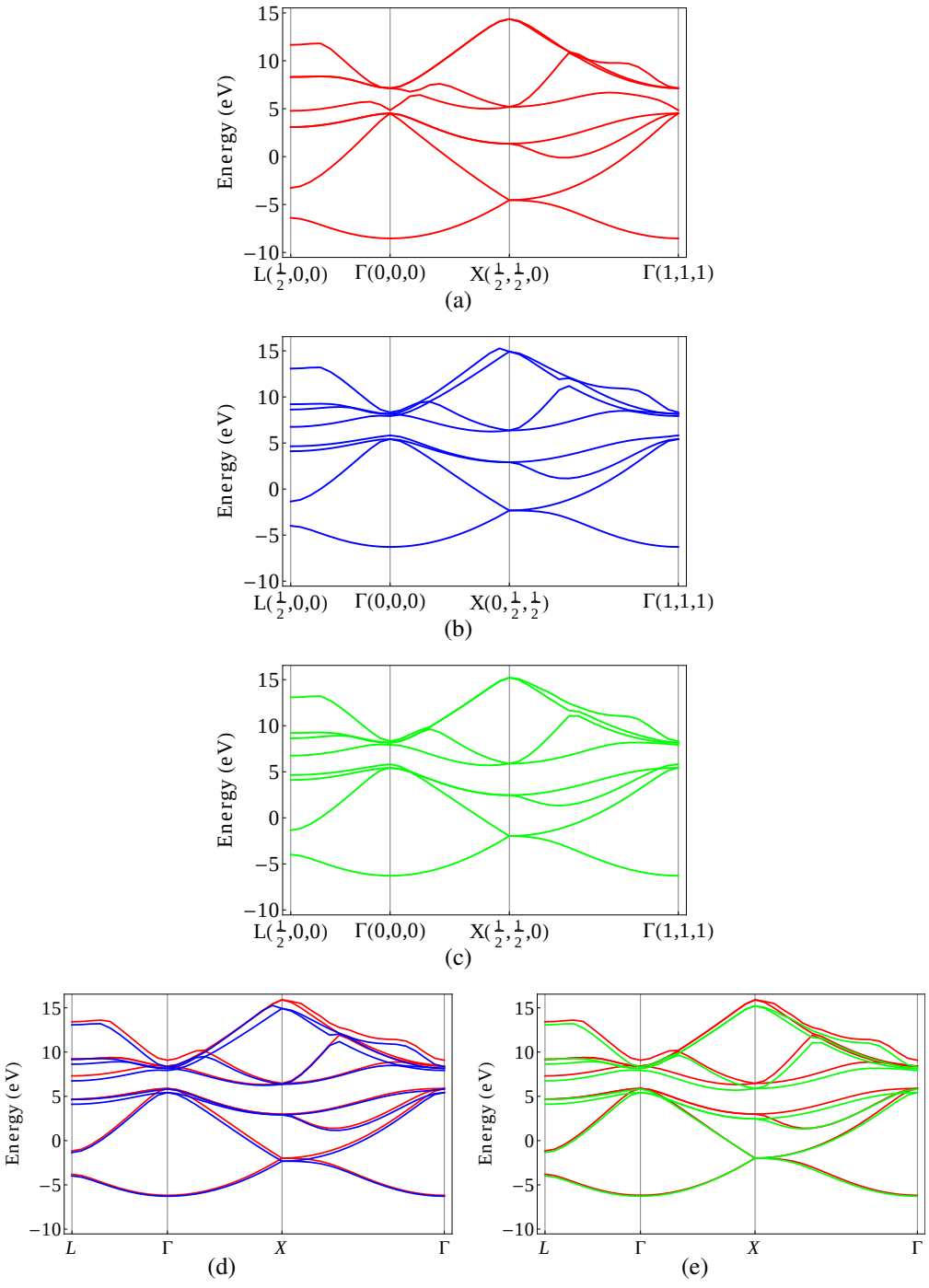


Figure 5.8: Bulk band structures along the path $L\Gamma XL$ for (a) germanium, (b) strained silicon going from $\Gamma(0,0,0)$ to $X\left(0,\frac{1}{2},\frac{1}{2}\right)$ and (c) strained silicon going from $\Gamma(0,0,0)$ to $X\left(\frac{1}{2},\frac{1}{2},0\right)$. (d) and (e) compare bulk unstrained silicon in red to the strained silicon in (b) and (c), respectively.

we repeat the method now for strained silicon. The silicon is aligned as before as shown in Fig. 5.9(b) and Fig. 5.9(d) for both aligned and misaligned and the results for $\Delta E_{Si}$ are given in Table 5.1 and illustrated in Fig. 5.4.

Table 5.1: Calculated energy shift (in eV) of the average local potential from bulk germanium to that in the germanium side of the GeSi slab (aligned and misaligned). We also show the corresponding quantities for the strained silicon side of the slab.

| | GeSi Aligned | GeSi Misaligned |
|---|---|---|
| $\Delta E_{Ge}$ | $3.27 \pm 0.05$ | $3.41 \pm 0.07$ |
| $\Delta E_{Si}$ | $4.78 \pm 0.12$ | $4.83 \pm 0.06$ |

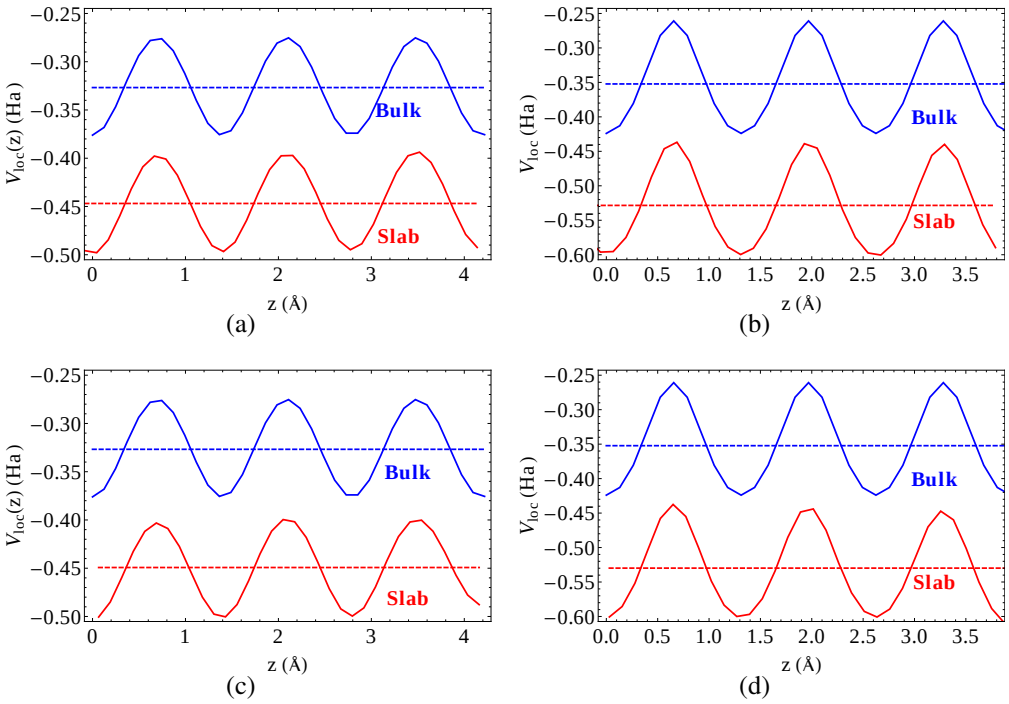


Figure 5.9: Comparison of the averaged local potential in bulk (blue) and corresponding region of GeSi slab (red) as a function of the perpendicular coordinate z for (a) germanium side of slab in "aligned" geometry, (b) silicon side of slab in "aligned" geometry, (c) germanium side in "misaligned" geometry and (d) silicon side of slab in "misaligned" geometry.

### 5.3.3 Projected Band Structures

So far, we have used the results of self-consistent calculations to derive the potential shift $\Delta\overline{V}$ of the interface slab and also the bulk band structures to derive the positions of the bands with respect to the average local potentials $\overline{V}_{loc}$. In order to investigate the presence of interface states we need to first project a 3D band structure on the 2D surface Brillouin zone. Here we follow a surface path $\overline{\Gamma JKJ'\Gamma}$ as shown in Fig. 2.2 in Chapter 2. We run a series of conventional band structure calculations around a path that is equivalent to the surface Brillouin zone path but offset along $k_\perp$ by an increasing value for bulk germanium and strained silicon. As mentioned in Chapter 2 on the section on projected band structures, the difficulty is translating the path from the surface Brillouin zone back to the equivalent path in the bulk Brillouin zone. We take that same set of k-points and add a constant $k_\perp$ for increasing values of $k_\perp$ until you reach the Brillouin zone boundary is reached.

Using the values in Table 5.1 for $\Delta E_{Ge}$ and $\Delta E_{Si}$ derived when aligning the averaged potentials of the bulk to the corresponding slab averaged potential, the projected band structure of bulk germanium is shifted by 3.27 eV and strained silicon by 4.78 eV. We superimpose these band structures onto each other and this gives the projected bulk bands for germanium and strained silicon. The projected band structure along the same surface path $\overline{\Gamma JKJ'\Gamma}$ for the GeSi for the aligned interface slab is shown in Fig. 5.10(a). The projected bulk band structure is generally shaded and we then overlay the actual interface slab band structure to see if interface states exist as shown in Fig. 5.12(a). No interface electronic states are present in the gap for this GeSi aligned structure, as initially expected due to the diamond crystal cubic structure exhibited throughout and thus, no dangling bonds are found at the interface.

In the misaligned case where we have a GeSi(001)-$(2\times1)$ interface reconstruction, the cell size has doubled in size compared to the aligned GeSi(001)-$(1\times1)$ interface.

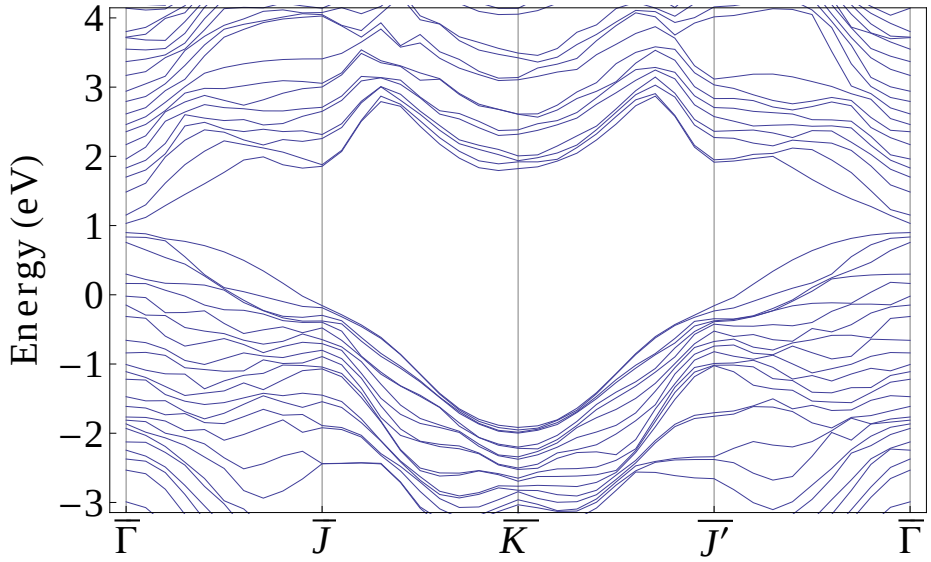


(a)

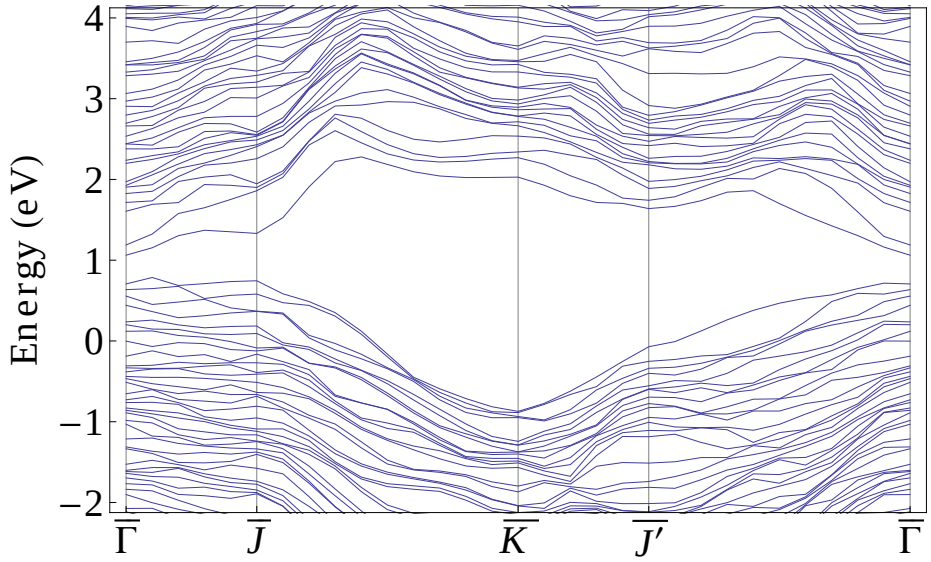


(b)

Figure 5.10: Projected electronic bands along the surface path $\overline{\Gamma JKJ'\Gamma}$ in the Brillouin zone for (a) the GeSi aligned $(1 \times 1)$ interface and (b) the misaligned $(2 \times 1)$ interface.

The lattice vectors for such a $(2 \times 1)$ cell are

$$\mathbf{a_1} = \frac{a}{2}(1,-1,0), \tag{5.9}$$
$$\mathbf{a_2} = \frac{a}{2}(2,2,0), \tag{5.10}$$
$$\mathbf{a_3} = \frac{a}{2}(0,0,n) \tag{5.11}$$

where $a$ is the lattice constant, $n$ is an integer for the number of cells in the $z$ direction. The vector $\mathbf{a_2}$ is twice the size of the corresponding vector in the $(1 \times 1)$ cell. Using the condition

$$\mathbf{a}_i.\mathbf{g}_j = 2\pi\delta_{ij} \tag{5.12}$$

where $\delta_{ij}$ is the Kronecker delta and the reciprocal lattice vectors $\mathbf{g}_j$ for this cell are given as

$$\mathbf{g_1} = \frac{2\pi}{a}(1,-1,0), \tag{5.13}$$
$$\mathbf{g_2} = \frac{2\pi}{a}(\frac{1}{2},\frac{1}{2},0), \tag{5.14}$$
$$\mathbf{g_3} = \frac{2\pi}{a}(0,0,\frac{2}{n}) \tag{5.15}$$

where $\mathbf{g_2}$ is halved from the $(1 \times 1)$ cell. This means that the Brillouin zone has halved as shown in Fig. 5.11 and also the surface path is halved. We follow along the path of the reduced Brillouin zone denoted as $\overline{\Gamma JKJ'\Gamma}$. It is important here to note that the reduced coordinates for the points $\overline{\Gamma}$, $\overline{J}$, $\overline{K}$, $\overline{J'}$ and $\overline{\Gamma}$ are the same as that in the $(1 \times 1)$ surface Brillouin zone, however when calculating the bulk projected band structures for bulk germanium and strained silicon, care is required as the Brillouin

zone is halved in the conventional cell. The projected band structure for this misaligned $(2 \times 1)$ interface is shown in Fig. 5.12(b). When we overlay the interface slab band structure with that of the bulk materials as shown in Fig. 5.12(b), we see states exist in the band gap. Five states exist in the gap in Fig. 5.12(b) of which four of these exist near the valence band edge and the other state exists higher up in the gap near the conduction band edge. The charge densities for these states as shown in Fig. 5.13(a) - 5.13(e) are calculated at the $\overline{K}$-point to view if these states are actually interface states. The charge density contour plot shown in Fig. 5.13(a) represents the state nearest the valence band edge, ascending in order to Fig. 5.13(e) representing the state nearest the conduction band edge.

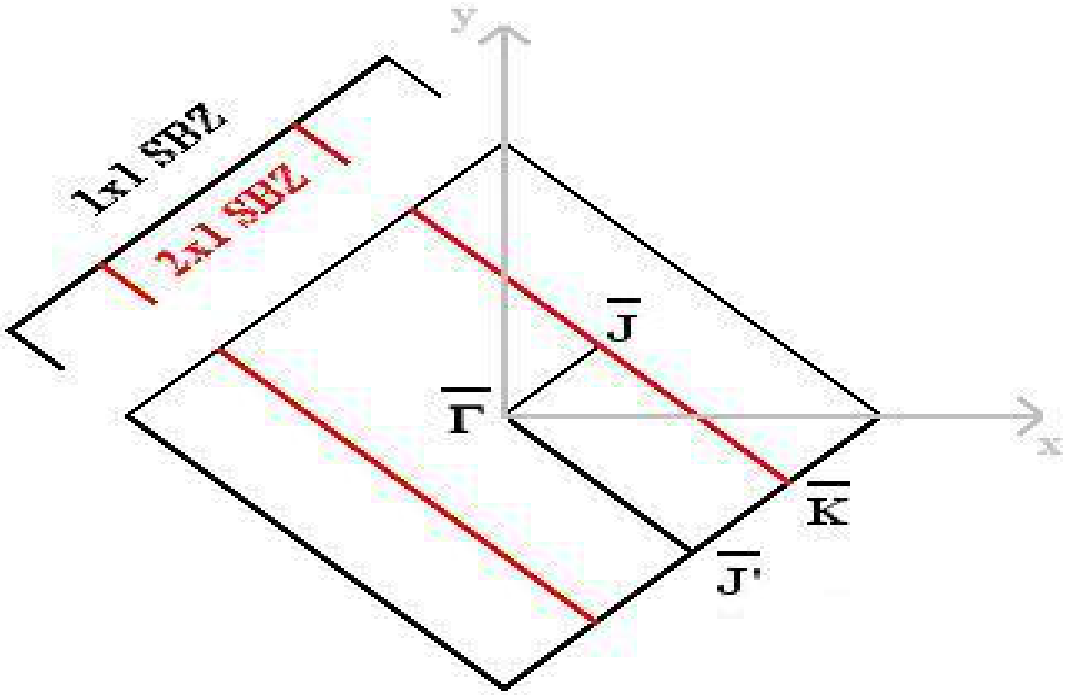


Figure 5.11: Surface Brillouin zone for the face centred cubic structure for $(1 \times 1)$ cell in black and the $(2 \times 1)$ cell in red. High symmetry points are shown on the $(2 \times 1)$ cell.

The lowest state in the gap is shown in Fig. 5.12(b), only appears in the gap around

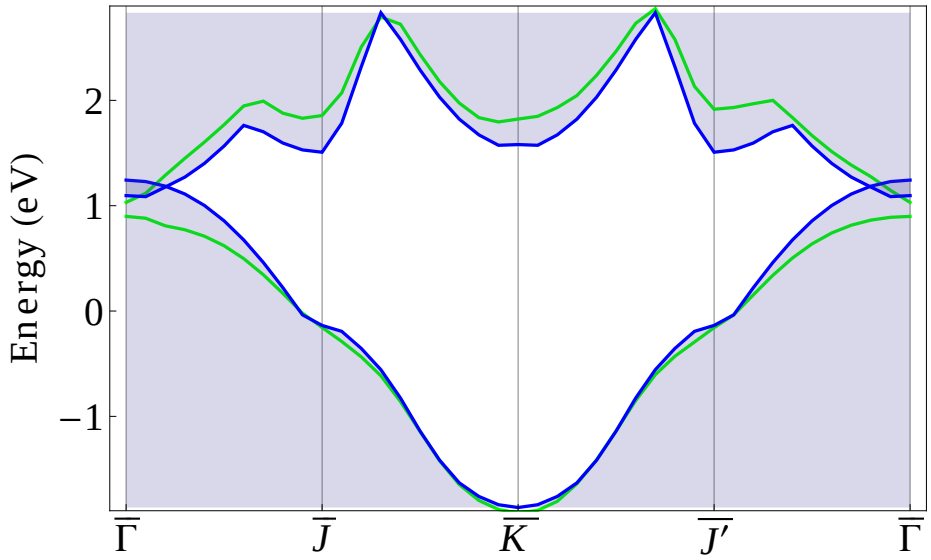


(a)

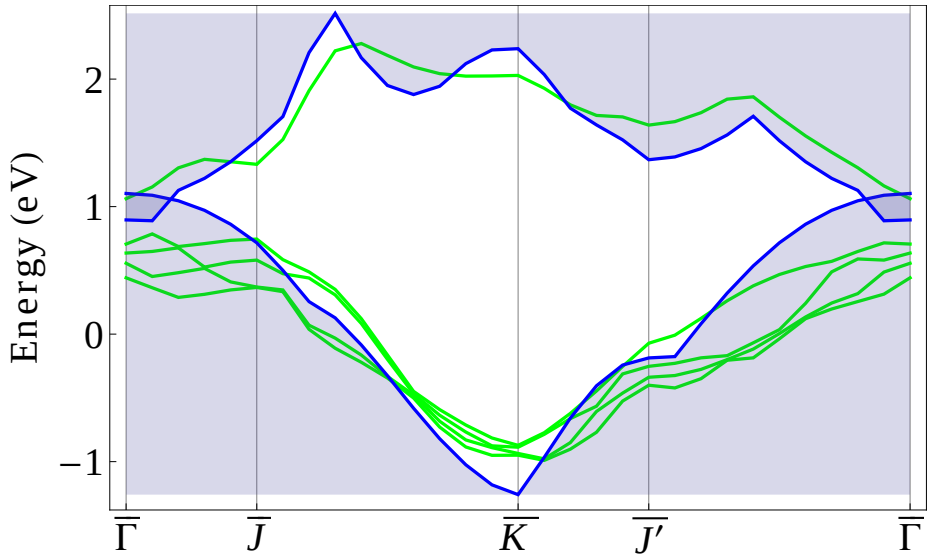


(b)

Figure 5.12: Projected electronic bands along the surface path $\overline{\Gamma JKJ'\Gamma}$ in the surface Brillouin zone using the germanium lattice constant. The slab electronic bands are represented in green and the bulk bands is the purple shaded area in (a) for the GeSi aligned interface, where no states are present in the band gap and (b) for the misaligned interface with states present in the band gap.

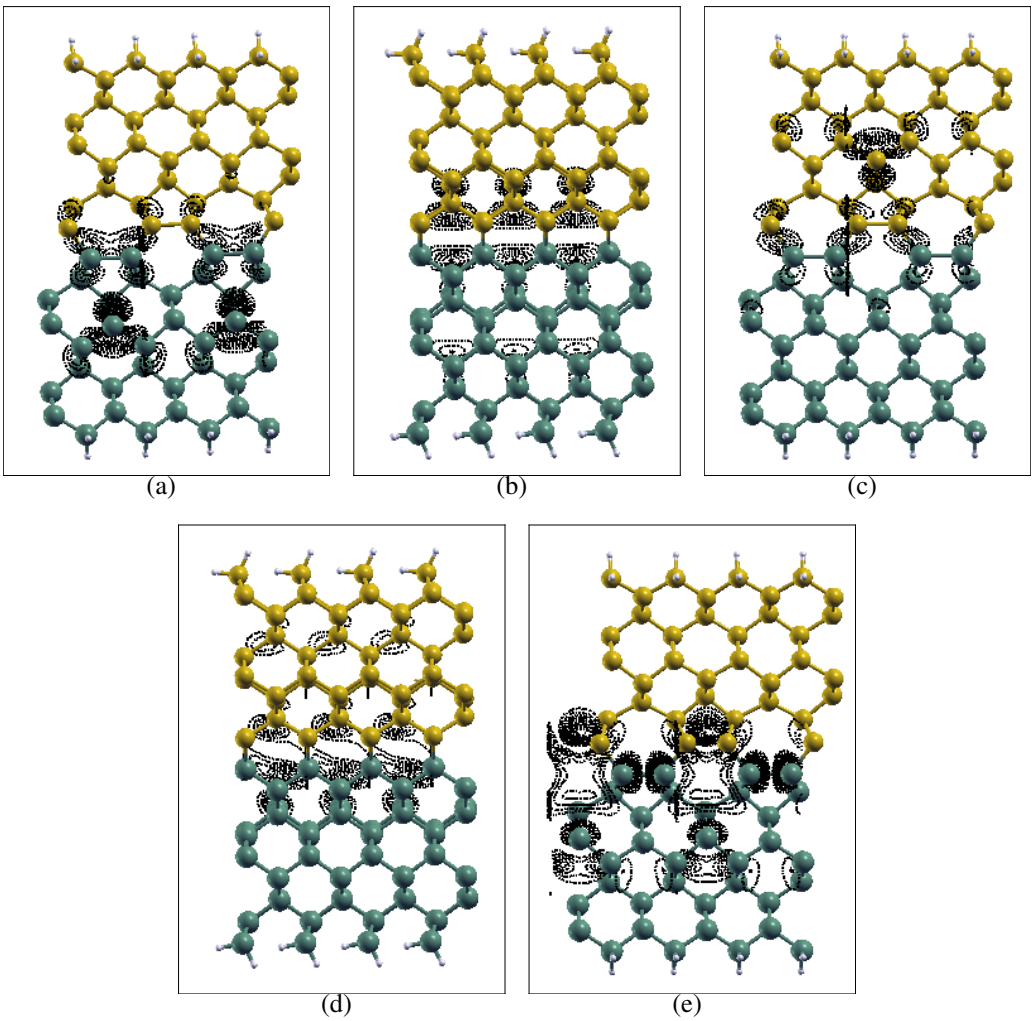


Figure 5.13: The charge density contour plots for the misaligned GeSi interface for the states shown in Fig. 5.12(b). All plots are calculated at the $\overline{K}$-point. (a) represents the state nearest the valence band edge, ascending in order to (e) which shows the state nearest the conduction band edge. Panels (b) and (d) are displayed in a drawing plane perpendicular to that of the other panels.

the $\overline{K}$-point and remains in bulk throughout the rest of the Brillouin zone. The charge density for this occupied state at the $\overline{K}$-point is shown in Fig. 5.13(a), where the largest percentage of charge density is located on the germanium side of the interface. The charge density appears as a bridge bond on a germanium atom deep in the slab and on the Ge-Si interface bond, thus implying an interface state. The charge density of the next occupied state is shown in Fig. 5.13(b) and is displayed in a drawing plane perpendicular to that of the other panels. The charge density contour lines are concentrated around the germanium and silicon atoms in a layer below the interface. These contour lines represent what is known as a back bond interface state induced by the interface. Such a back bond state exist also on the Ge(001)-$(2 \times 1)$ surface as shown in Fig. 3.2(a) of Chapter 3 and appears in the projected band structure in a very similar manner to that of the GeSi the interface. The third state near the valence band edge which is occupied appears in the gap at the $\overline{J}$-point and follows the valence band edge until it re-enters the bulk again at $\frac{1}{2}\overline{KJ'}$. Contour lines are present at the Ge-Si interface bond in Fig. 5.13(c), thus representing an interface state. We also see a large proportion of charge density is located at a silicon atom deep in the bulk as a bridge-bond state. The last state near the valence band edge enters the gap at the $\overline{J}$-point and does not re-enter the bulk until $\frac{1}{4}\overline{J'\Gamma}$. This occupied state is the most dominant state in the gap and the charge density plot for this state is shown in Fig. 5.13(d) and is displayed in a drawing plane perpendicular to that of the other panels. The charge density is mainly concentrated around a germanium atom at the interface layer as a back-bond state and similarly around a silicon atom at the interface thus again implying the presence of an interface state. Finally the unoccupied state in the gap near the conduction band edge appears along $\overline{J}$ to $\frac{1}{2}\overline{JK}$ and again at $\overline{K}$ as shown in Fig. 5.12(b). The charge density plots in Fig. 5.13(e) show contour lines around both the Ge-Ge and Si-Si interface dimers along with Ge-Si interface bond, thus this does represent an interface state.

## 5.4 Interface using the Silicon Lattice Constant

The aligned and misaligned GeSi interface were also relaxed using the lattice constant of silicon, at the calculated value of 5.41 Å which is about 0.4% smaller than the experimental value of 5.43 Å. The aligned structure is shown in Fig. 5.2(b) with a Ge-Si bond length of 2.36 Å. The misaligned structure is shown in Fig. 5.2(d) with a Ge-Ge and Si-Si symmetric dimer bond length of 2.56 Å and 2.69 Å respectively, and a Ge-Si bond length of 2.39 Å.

The band line ups at the interface are calculated as already mentioned in this chapter in Section 5.3.2 using the averaged local potential as a function of the perpendicular coordinate. The potential shift of the aligned and misaligned GeSi slab are $\Delta\overline{V} = 2.75$ eV and $\Delta\overline{V} = 2.54$ eV, respectively. Since we are now repeating the calculations using the silicon lattice constant, we are faced with the problem that germanium is now strained. Before we proceed in calculating the projected band structures where we require the energy separation between relative parts of slab potential to their corresponding bulk potentials, an investigation of the strain in germanium is required.

With the germanium now aligning with the silicon lattice, the germanium strains so that it matches the silicon lattice constant in the interface plane ($x$ and $y$) and this leads to the expansion of the respective layers in the perpendicular direction $z$. As mentioned already in Section 5.3.2.1, we calculate the layer separation $d_i$ from the slab and compare this to the cell parameter of strained germanium in the perpendicular direction as optimized using the ABINIT code. The lattice vector calculated from this optimization for strained germanium in this perpendicular $z$ direction is $a_{Ge,strained} =$ 5.71 Å. The layer separation for strained germanium is derived at $d = \frac{5.71}{4} = 1.43$ Å.

In Fig. 5.14(a) we see the strained germanium layer separation in the (001) direction (blue line) in the slab matches well to the optimized value of 1.43 Å (green line). The unstrained germanium layer separation is shown in red in Fig. 5.14(a). The layer

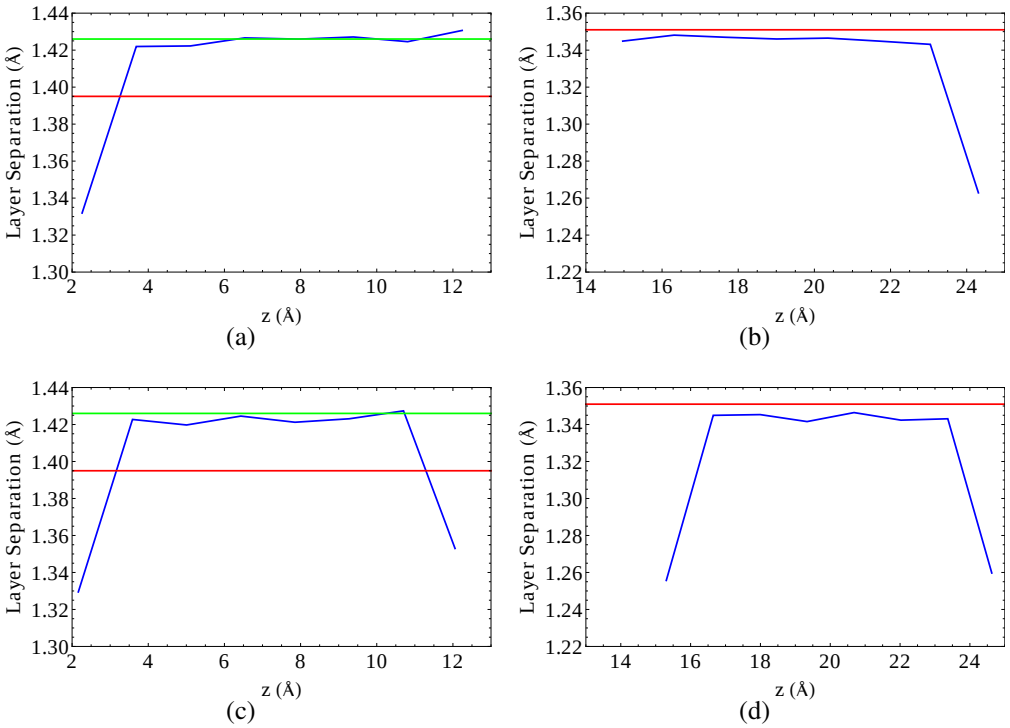


Figure 5.14: Atomic layer separation $d$ (blue line) in the relaxed GeSi slab as a function of position $z$ perpendicular to the plane of the interface. The region with $z < 13$ Å [in (a) and (c)] is strained germanium with the in-plane lattice constant matched to unstrained silicon and the region with $z > 14$ Å [in (b) and (d)] is unstrained silicon. Panels (a) and (b) show results for the "aligned" interface geometry and panels ( c) and (d) show results for the "misaligned" geometry. The red lines indicate the corresponding unstrained bulk layer separation and the green line indicates the $z$ interlayer separation found in bulk germanium, when its $x-y$ lattice constant is constrained to match that of unstrained silicon.

separation for silicon on the silicon side of the interface slab described by the blue line in Fig. 5.14(b) is slightly less ($\approx 0.5\%$) than the value derived from the silicon lattice constant of $d = \frac{5.41}{4} = 1.35$ Å (red line). Similarly for the misaligned GeSi interface we see in Fig. 5.14(c) and Fig. 5.14(d) the layer separation of bulk regions in the slab match well to the predicted layer separation values.

Moving along the path $L\Gamma XL$ in the Brillouin zone, the band structure calculation for bulk silicon is shown in Fig. 5.15(a) with a band gap of 0.44 eV. Strained germanium has a band gap of 0.10 eV in the cases where we move from $\Gamma(0.0,0.0,0.0)$ to $X(0.0,0.5,0.5)$ as shown in Fig. 5.15(b). However when we move from $\Gamma(0.0,0.0,0.0)$ to $X(0.5,0.5,0.0)$ the band gap increases to 0.18 eV as shown in Fig. 5.15(c). Bulk germanium has its valence band maximum at the $\Gamma$-point and its conduction band minimum at the $L$-point. In Fig. 5.15(d) and Fig. 5.15(e), we superimpose the strained germanium case using $X(0.0,0.5,0.5)$ and $X(0.5,0.5,0.0)$, respectively over the unstrained germanium band structure. We see in Fig. 5.15(d), the valence band maximum remains at the $\Gamma$-point, however the conduction band minimum occurs along the $\Delta$ line and in Fig. 5.15(e) the conduction band minimum returns to bulk-like and occurs at the $L$-point.

We can now calculate the energy separation $\Delta E_i$ for the strained germanium side of the slab potential with its corresponding strained germanium bulk potential and also the silicon. In order to align the bulk bands with the GeSi slab bands as before, we find the energy separation for the aligned and the misaligned slab, and the results are shown in Table 5.2

Using these values the projected band structures for the aligned and misaligned GeSi slab using the silicon lattice constant as shown in Fig. 5.16(a) and in Fig. 5.16(b) respectively. As expected no interface states exist in the aligned interface slab, while for the misaligned slab, states appear in the band gap but are pushed more into the bulk

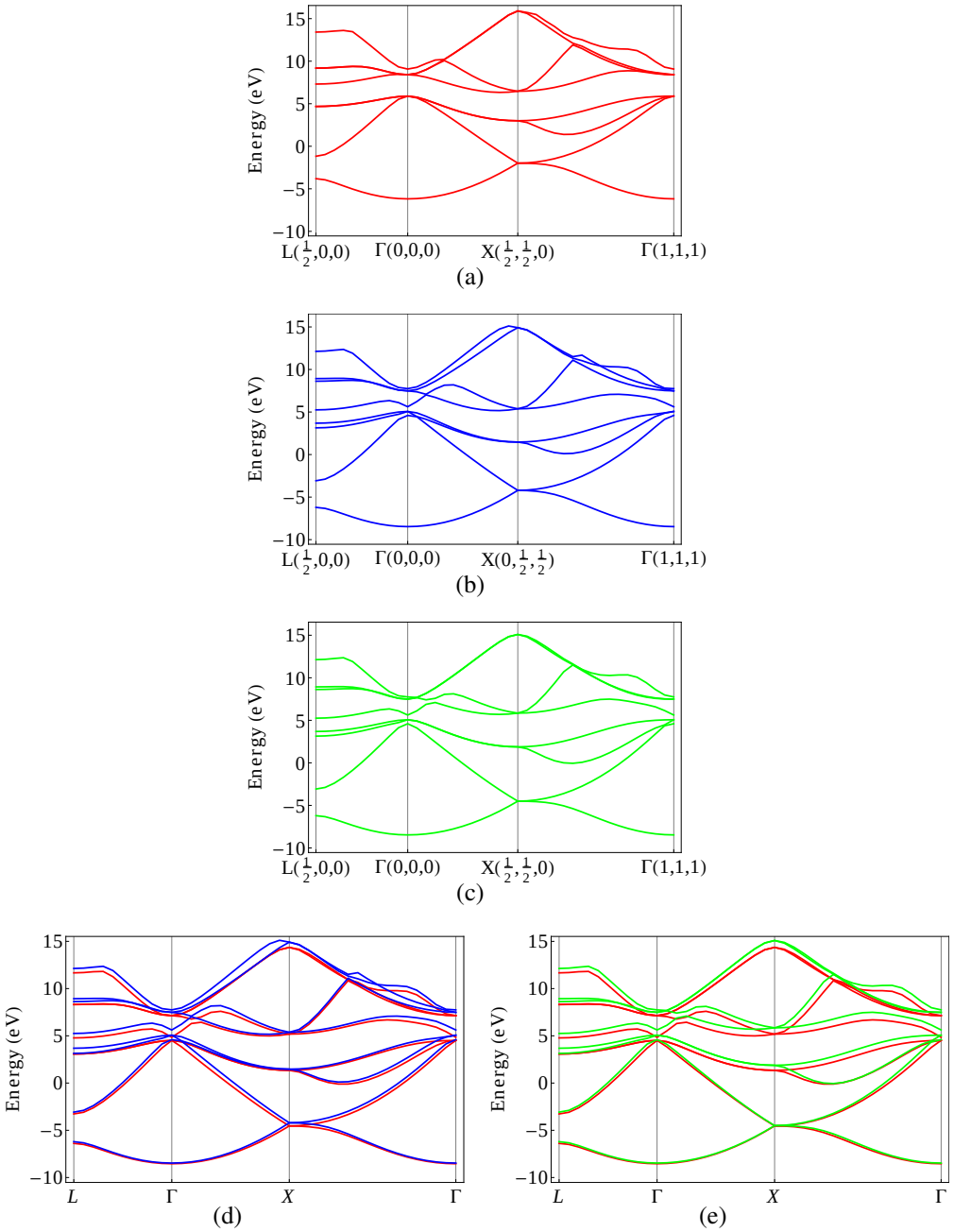


Figure 5.15: Bulk band structures along the path $L\Gamma XL$ for (a) silicon, (b) strained germanium going from $\Gamma(0,0,0)$ to $X\left(0,\frac{1}{2},\frac{1}{2}\right)$ and (c) strained germanium going from $\Gamma(0,0,0)$ to $X\left(\frac{1}{2},\frac{1}{2},0\right)$. (d) and (e) compare bulk unstrained germanium in red to the strained germanium in (b) and (c), respectively.

Table 5.2: Calculated energy shift (in eV) of the average local potential from strained germanium to that in the germanium side of the GeSi slab (aligned and misaligned). We also show the corresponding quantities for the silicon side of the slab.

| | GeSi Aligned | GeSi Misaligned |
|---|---|---|
| $\Delta E_{Ge}$ | $3.05 \pm 0.07$ | $3.14 \pm 0.08$ |
| $\Delta E_{Si}$ | $4.53 \pm 0.11$ | $4.98 \pm 0.16$ |

than in the case where we use the germanium lattice constant as shown in Fig. 5.12(b). Five states exist in the gap in Fig. 5.16(b) of which four of these exist near the valence band edge and the other state exists higher up in the gap near the conduction band edge. The charge densities for these states as shown in Fig. 5.17(a) - 5.17(e), where the states near the valence band edge are calculated at the $\overline{K}$-point and the one state near the conduction band edge is calculated at $\overline{J}$-point. The charge density contour plot shown in Fig. 5.17(a) represents the state nearest the valence band edge, ascending in order to Fig. 5.17(e) representing the state nearest the conduction band edge. The charge density of the lowest occupied state in the gap as shown in Fig. 5.17(a), shows the existence of contour lines around the Ge-Si interface bond implying an interface state. It must also be noted, a large proportion of the charge density is located around germanium atoms and silicon atoms in bridge bond like states deep in the germanium and silicon sides of the slab respectively. The charge density of the next occupied state in Fig. 5.17(b) is a back-bond state where the contour line exists on the germanium and silicon atoms in a layer below the interface. This is similar to the back bond state we see on the Ge(001)-$(2 \times 1)$ in Chapter 3. This state shown here is an interface state as it is induced by the interface. This state is displayed in a drawing plane perpendicular to that of the other panels. The contour lines of the next occupied state is shown in Fig. 5.17(c) are around the germanium and silicon atoms on the interface layer showing an interface state. In Fig. 5.17(d), the contour lines are localised around germanium atoms deep in the slab like a bridge-bond state, however this is again an

interface state as the contour lines are induced by the interface. This occupied state is also displayed in a drawing plane perpendicular to that of the other panels. The final state in the gap near the conduction band edge appears only around the $\bar{J}$-point and is the only unoccupied state in the band gap. The charge density in Fig. 5.17(e) shows the charge located around three silicon atomic layers at the interface and on the Ge-Ge dimer at the interface. This is an interface state.

## 5.5 Conclusion

In conclusion, after we perform calculations for structural relaxations and electronic band structures using both the germanium and silicon lattice constants, we see that the GeSi aligned interface structure follows the diamond cubic crystal structure across the interface. Strain was an important feature in all our calculations due to the independent use of a particular lattice constant in each calculation. Upon calculation of the projected band structures, no interface states are present in the band gap as expected due to no dangling bonds being present at the interface.

The GeSi misaligned interface reconstructs to a $(2 \times 1)$ structure with the presence of Ge-Ge and Si-Si dimers and alternating 5-fold and 7-fold rings in the mismatched regions to adjust the bonding at the interface. The projected band structure for this misaligned GeSi interface using both the germanium and silicon lattice constants show the presence of states in the band gap. Four states are present near the valence band edge in which all are occupied and one state appears near the conduction band edge which is unoccupied. All these states in the gap are interface states whereby the charge densities are located around the germanium and silicon interface layers or the charge densities are located in the slab induced by the GeSi interface. However the only state that is of concern in the development of a GeSi APD is the unoccupied state as it has the potential to create an electronic trap for the carriers. The projected band structure

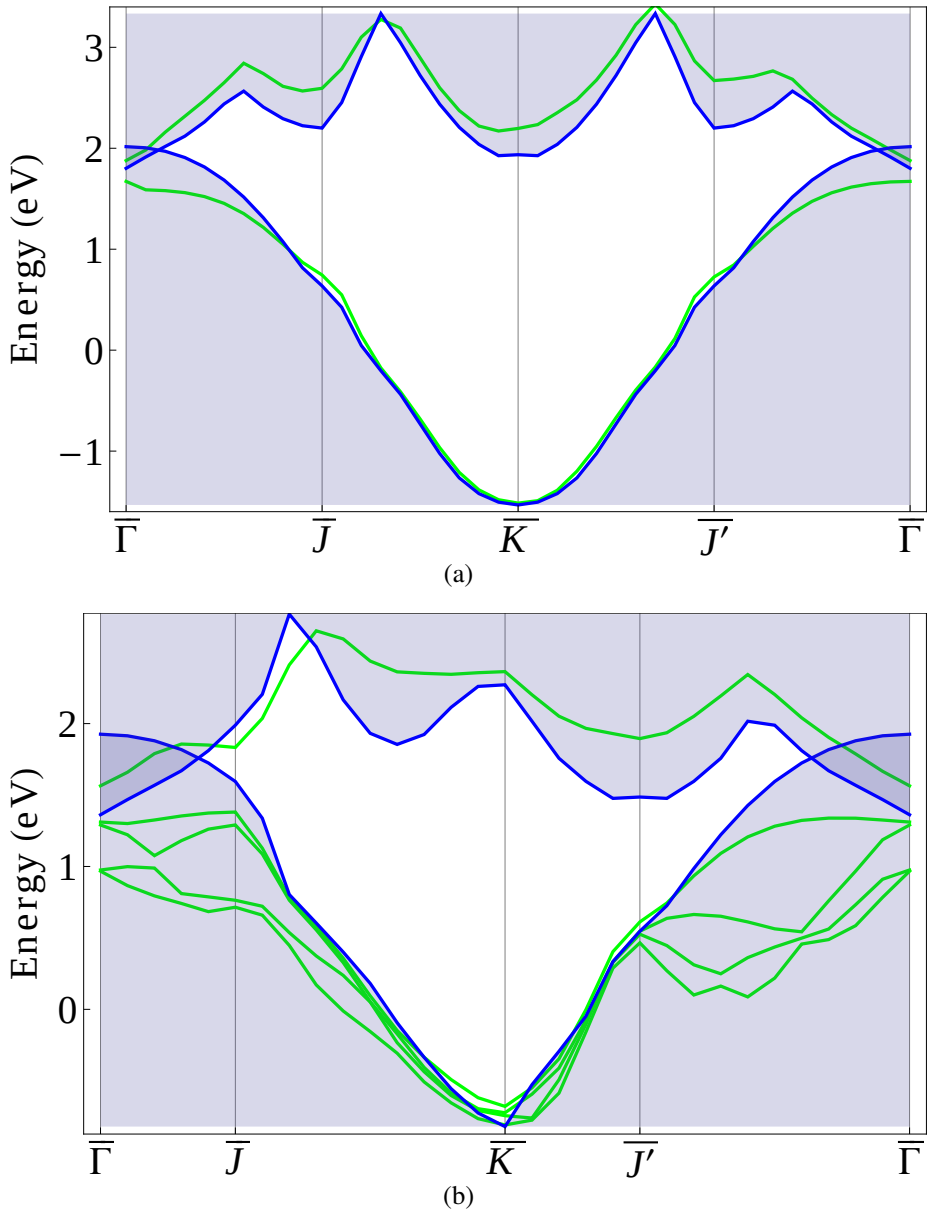


Figure 5.16: Projected electronic bands along the surface path $\overline{\Gamma JKJ'\Gamma}$ in the surface Brillouin zone using the silicon lattice constant. The slab electronic bands are represented in green and the bulk bands is the purple shaded area in (a) for the GeSi aligned interface, where no states are present in the band gap and (b) for the misaligned interface with states present in the band gap.

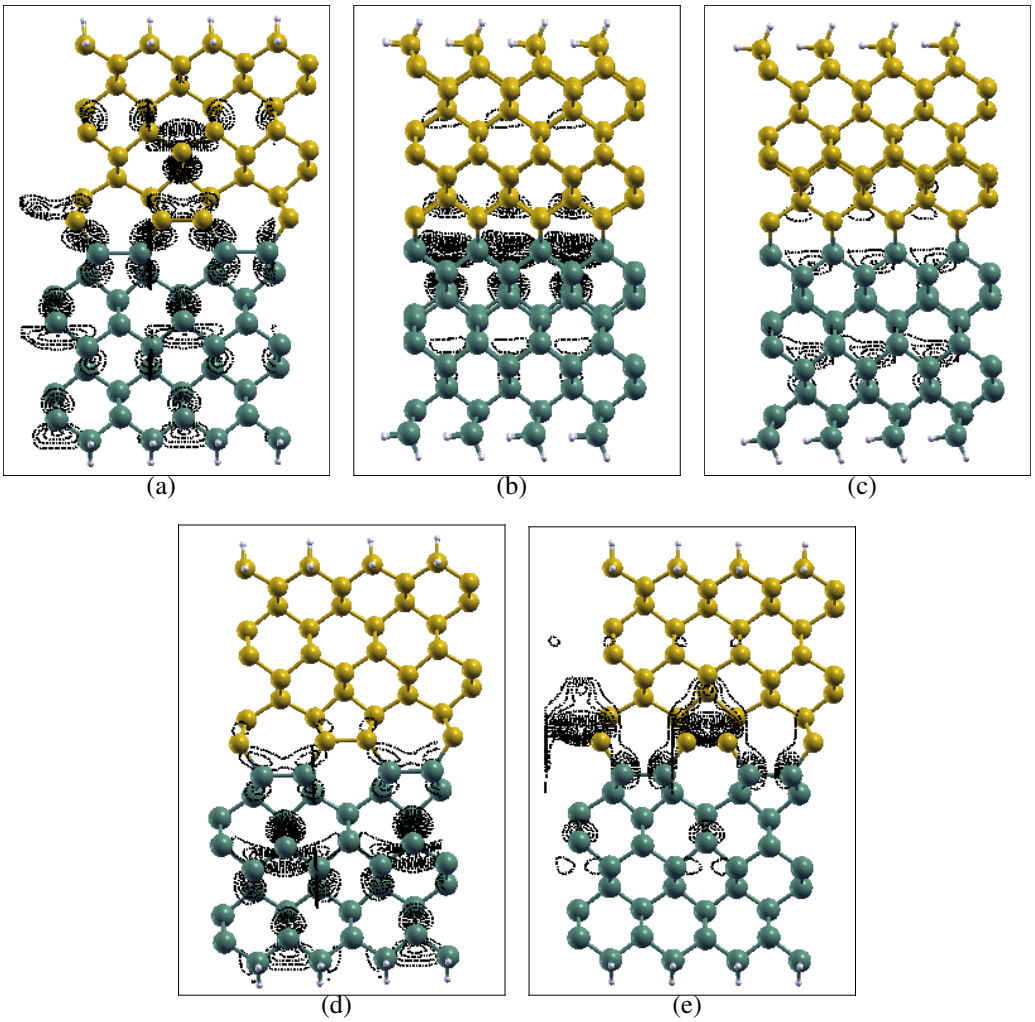


Figure 5.17: The charge density contour plots for the misaligned GeSi interface for the states shown in Fig. 5.16(b). (a) represents the state nearest the valence band edge, ascending in order to (e) which representing the state nearest the conduction band edge. Panels (b) and (d) are displayed in a drawing plane perpendicular to that of the other panels. (a)-(d) are calculated at the $\overline{K}$-point and (e) is calculated at the $\overline{J}$-point.

using the silicon lattice constant shows the states in the band gap are positioned nearer the valence band edge than that of the germanium lattice constant case. Again the states near the valence band edge are all fully occupied. The unoccupied state that existed near the conduction band edge using the germanium lattice constant, is pushed more into the bulk region when using the silicon lattice constant and the state only appears slightly around the $\overline{J}$-point. Thus if we were to able to calculate the exact wafer bonded GeSi interface using first-principle calculations we would expect the electronic bands to be somewhere in the middle region between the germanium and silicon lattice constant calculations.

Finally examining the best and worst case scenario of aligned and misaligned regions of the GeSi interface, we see good bonding in both cases at the interface. We also see that one unoccupied interface state exists in the band gap in the GeSi misaligned interface using the germanium and silicon lattice constants, thus this has the potential to be a problem in the development of a GeSi avalanche photodiode. We will look at the use of sulfur in the interface in order to possibly remove this interface state.

CHAPTER 6

# Ge-S-Si and Ge-S-H-Si Interfaces

*The structural and electronical characteristics of a Ge-Si(001) interface are calculated in the previous chapter. Sulfur is an atom with flexible chemical bonds and we investigate if this flexibility will adjust the bonding in the interface regions where the germanium and silicon lattices align and misalign. We also investigate the presence of both sulfur and hydrogen at the interface as the presence of both species on the germanium surface removes surface states. We use the same supercell approach using first-principles density functional theory in the local density approximation (LDA). Self-consistent calculations determine the atomic structure and the band lineup of the germanium and silicon band structures. Projected band structure calculations show that interface states do exist in the band gap despite the qualitative considerations that led us to expect sulfur and hydrogen would assist in passivating the interface.*

## 6.1 Introduction

Germanium and silicon interfaces across the aligned and misaligned regions show different bonding configurations and electronic structure. In the aligned lattice the slab

follows the diamond crystal structure, while in the misaligned region a $(2 \times 1)$ reconstruction is present. The aligned GeSi interface is free of interface electronic states as shown in Chapter 5. It is widely known that both the silicon and germanium surfaces form a $(2 \times 1)$ reconstruction with the presence of dangling bond states present in the band gap. We have shown in Chapter 5 that the misaligned GeSi interface shows the $(2 \times 1)$ reconstruction at the interface and has one interface state present on the Ge-Ge and Si-Si dimers in the $(2 \times 1)$ reconstruction of the interface region.

Here we investigate the possibility that the use of sulfur [103], [104] and [105] with its flexible chemical bonds may improve the bonding across the interface of germanium [106] and silicon and provide an interface free of electronic states. Looking at the clean Ge(001)-$(2 \times 1)$ surface, adsorption of a full monolayer of sulfur changes the structure into a $(1 \times 1)$ geometry [107], removing the dimers and restoring the germanium bulk configuration [27]. The electronic structure is very different to the Ge(001)-$(2 \times 1)$ surface because the adsorbed sulfur atoms have six valence electrons instead of the four valence electrons characteristic of germanium. In Ref [27], the sulfur passivated germanium surfaces show dangling bond states, a back bond state and a bridge bond state. We begin with this sulfur passivated germanium surface and investigate the geometric and electronic structure when this surface is bonded to a silicon slab, creating the GeSSi interface.

When both hydrogen and sulfur are bonded to the clean Ge(001)-$(2 \times 1)$ surface, as discussed in detail in Chapter 4, first-principles density functional theory calculations confirm that the $(2 \times 1)$ surface reconstruction remains and predicts the formation of (S-H)-(S-H) inter-germanium dimer bridges. The computed energy band gap of this atomic configuration is shown to be free of surface states with all the states being pushed into the bulk region [22]. With this knowledge we investigate if the presence of hydrogen and sulfur sandwiched between the germanium and silicon bulk will provide an interface free of electronic states.

## 6.2 Method of Calculation

In the calculations for the GeSi interfaces with sulfur and hydrogen, the interfaces are represented using $(2 \times 1)$ supercells as before and all the calculations are carried out exactly as they were in Section 5.2 of Chapter 5, except for the number of k-points used. We have used a 32 k-point mesh for all the supercells considered in this chapter based on the Monkhorst-Pack [41] scheme. Starting with the Ge(001)-$(2 \times 1)$ surface as shown in Chapter 3 we place a monolayer of sulfur over the surface and allow the structure to relax, thus reproducing the GeS(001)-$(1 \times 1)$ surface as shown in [27]. Using this relaxed GeS surface structure, a silicon slab is moved over the GeS surface. This represents the GeSSi interface as shown in Fig. 6.1(a) and Fig. 6.1(c) for the aligned and misaligned interfaces, respectively. Both structures are allowed to relax using the same procedure that is explained in Section 5.2, with the three atomic layers on both side of the interface (containing sulfur) only allowed to relax. The total number of atoms in these GeSSi interface supercells is 46 (18 germanium, 18 silicon, 2 sulfur and 8 hydrogen).

For the GeSHSi interface, we use the $H_2S$-terminated Ge(001)-$(2 \times 1)$ from Chapter 4 and place the silicon slab above the surface and allow the system to re-relax as shown later in this Chapter in Fig. 6.11(a) and Fig. 6.11(d) for the aligned and misaligned interfaces, respectively. Here as the $H_2S$-terminated germanium surface does not bond with the silicon surface, we artificially break the hydrogen bonds and re-relax the interface. The total number of atoms in these GeSHSi interface supercells is 48 (18 germanium, 18 silicon, 2 sulfur and 10 hydrogen).

Again here we investigate the aligned and misaligned regions for the GeSSi and GeSHSi interfaces using both the germanium and silicon lattice constants as in Chapter 5.

## 6.3 Ge-S-Si Interface using Ge Lattice Constant

### 6.3.1 Structural Relaxation

On relaxation using the germanium lattice constant, the GeSSi aligned interface results in a GeSSi(001)-$(2 \times 1)$ structure, with a Ge-S bond lengths of 2.22 Å and a S-Si bond lengths of 2.14 Å as shown in Fig. 6.1(b). We also see the existence of a Ge-Ge and Si-Si symmetric dimers of bond length 2.47 Å and 2.41 Å respectively. The binding energy of this interface defined as the energy difference between the initial structure (Fig. 6.1(a)) and the final relaxed geometry (Fig. 6.1(b)) per supercell is $\approx 47$ eV.

The relaxed GeSSi misaligned lattice results in a different GeSSi(001)-$(2 \times 1)$ reconstructed interface as shown in Fig. 6.1(d), with a Si-Si symmetric dimer bond length of 2.38 Å, four Ge-S bond lengths of 2.23 Å, 2.24 Å, 2.53 Å and 2.59 Å and a S-Si bond length of 2.16 Å. No Ge-Ge dimer is present in the misaligned structure. The binding energy of this misaligned interface is $\approx 44$ eV. It is also worth noting that the aligned structure is the most favourable interface energetically by 3 eV ($47 - 44$ eV).

The layer separation for the aligned and misaligned lattices are shown in Fig. 6.2(a)-6.2(d). As we are using the germanium lattice constant, we see as we did in Chapter 5, the silicon strains in the perpendicular direction as expected.

### 6.3.2 Band Lineup

The averaged local potential $\overline{V}_{loc}(z)$ as a function of the perpendicular coordinate $z$ is shown in Fig. 6.3(a) and Fig. 6.3(b) for the aligned and misaligned interfaces respectively. In these plots, different potentials are seen at the interface region where the sulfur atoms are positioned. This is due to the difference in bonding types at the two different interfaces, where the sulfur bonds to both a germanium and silicon atom

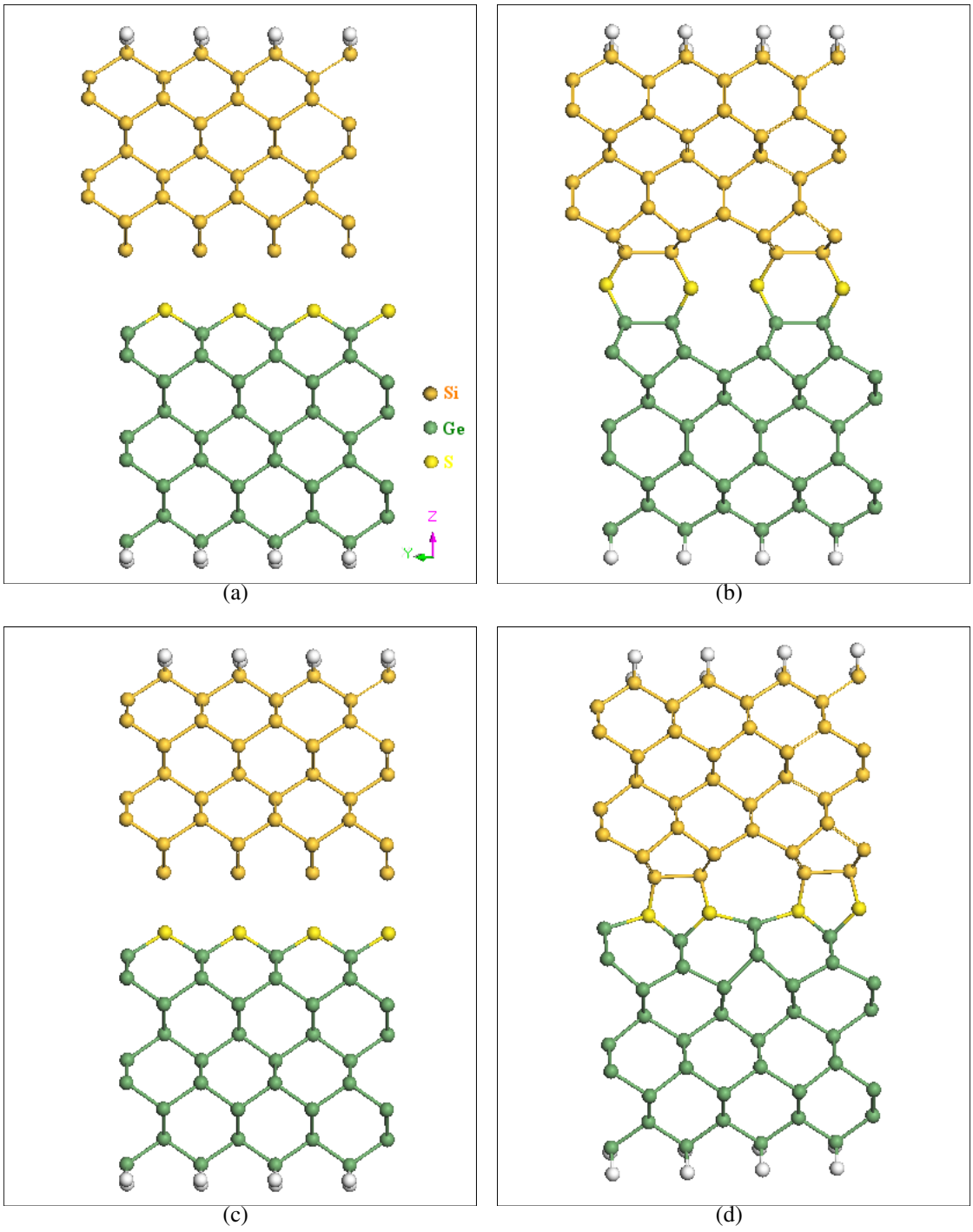


Figure 6.1: (a) The initial atomic configuration of the GeSSi aligned structure. (b) The GeSSi aligned interface after structural relaxation. The interface shows a GeSSi(001)-$(2 \times 1)$ reconstruction with the presence of Ge-Ge and Si-Si symmetric dimers. (c) The initial atomic configuration of the GeSSi misaligned structure. (d) The final relaxed geometry for the misaligned structure showing a GeSSi(001)-$(2 \times 1)$ interface with Si-Si dimer.

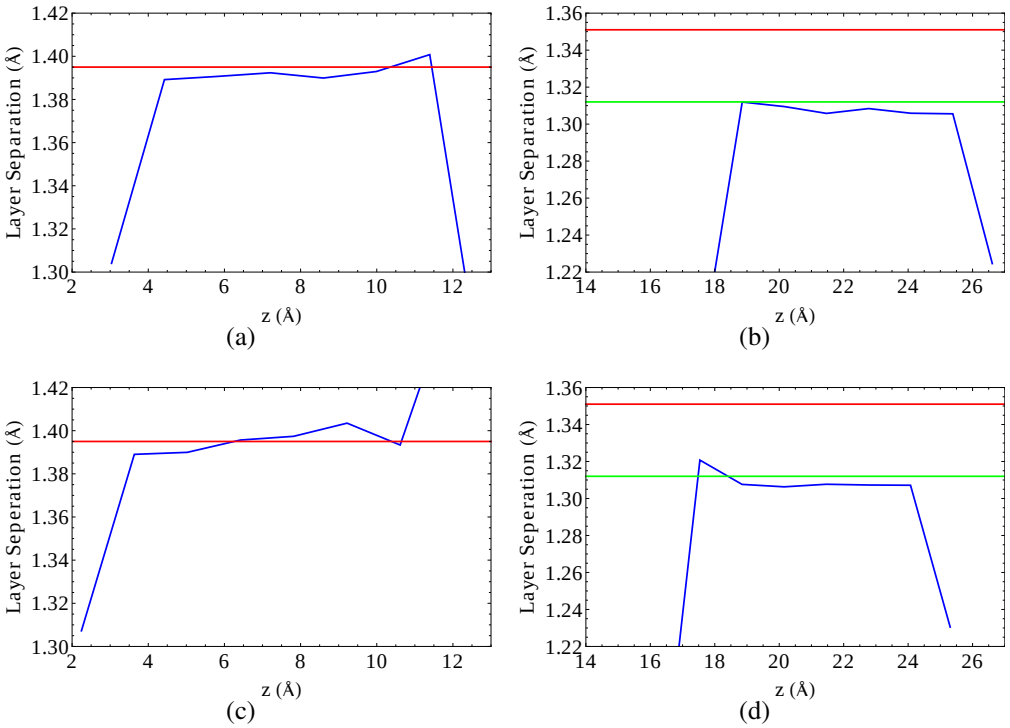


Figure 6.2: Atomic layer separation $d$ (blue line) in the relaxed GeSSi slab as a function of position $z$ perpendicular to the plane of the interface. The region with $z < 13$ Å [in (a) and (c)] is unstrained germanium and region the with $z > 17$ Å [in (b) and (d)] is silicon with the in-plane lattice constant matched to unstrained germanium. Panels (a) and (b) show results for the "aligned" interface geometry and panels (c) and (d) show results for the "misaligned" geometry. The red lines indicate the corresponding unstrained bulk layer separation and the green line indicates the $z$ interlayer separation found in bulk silicon, when its $x-y$ lattice constant is constrained to match that of unstrained germanium.

in the aligned interface in Fig. 6.1(b), while the sulfur bonds to two germanium and one silicon atom in the misaligned interface in Fig. 6.1(d).

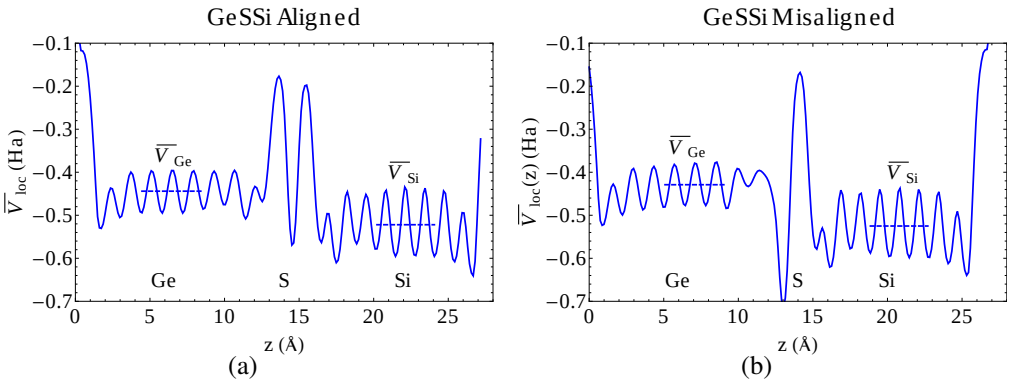


Figure 6.3: The local potential $\overline{V}_{loc}(z)$ averaged over the parallel components $x$ and $y$ as a function of the perpendicular coordinate $z$, to the interface for (a) the aligned and (b) misaligned GeSSi interface. The dashed line in both the germanium and silicon is represented as $\overline{V}_{Ge}$ and $\overline{V}_{Si}$, respectively, defined as the average local potential over three periodic potential cycles in each section of the slab. Ge, S and Si represent the regions in the slab where the germanium, sulfur and silicon atoms are located.

Using the averaged local potential $\overline{V}_{loc}(z)$ as a function of the perpendicular coordinate $z$, the potential shift $\Delta\overline{V} = \overline{V}_{Ge} - \overline{V}_{Si}$ for the aligned and misaligned structures are 2.11 eV and 2.62 eV, respectively. The energy separations $\Delta E_i$ as stated in Section 5.3.2 in Chapter 5, is defined as the difference in energy between the bulk potential and the corresponding part of the slab potential. These energy separations $\Delta E_i$ for the aligned and misaligned GeSSi interfaces are shown in Table 6.1. The aligning of the various potentials are shown in Fig. 6.4(a)- 6.4(d).

Table 6.1: Calculated energy shift (in eV) of the average local potential from bulk germanium to that in the germanuim side of the GeSSi slab (aligned and misaligned). We also show the corresponding quantities for the strained silicon side of the slab.

| | GeSSi Aligned | GeSSi Misaligned |
|---|---|---|
| $\Delta E_{Ge}$ | $3.26 \pm 0.14$ | $2.81 \pm 0.10$ |
| $\Delta E_{Si}$ | $4.69 \pm 0.16$ | $4.76 \pm 0.07$ |

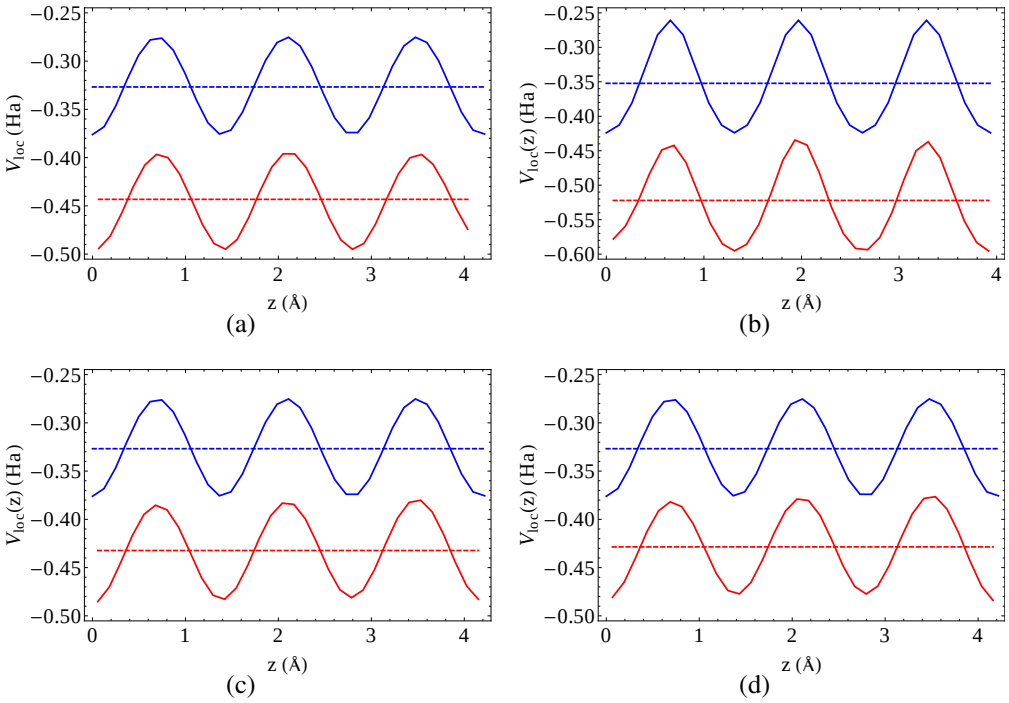


Figure 6.4: Comparison of the averaged local potential in bulk (blue) and corresponding region of GeSSi slab (red) as a function of the perpendicular coordinate z for (a) germanium side of slab in "aligned" geometry, (b) silicon side of slab in "aligned" geometry, (c) germanium side in "misaligned" geometry and (d) silicon side of slab in "misaligned" geometry.

### 6.3.3 Projected Band Structure

Using the values of the energy difference defined in Eq.5.3 and shown in Table 6.1, we show the projected band structures of the aligned and misaligned GeSSi interfaces in Fig. 6.5(a) and Fig. 6.5(b), respectively. In the aligned interface slab we see a large number of states in the band gap with six near the valence band and one near the conduction band. The charge density contour plots for each of these states are shown in Fig. 6.6(a) - 6.6(g), where Fig. 6.6(a) represents the state nearest the valence band edge, ascending in order to Fig. 6.6(g) representing the state nearest the conduction band edge. All the charge density plots are calculated at the $\overline{K}$-point.

In Fig. 6.6(a), the charge density of this occupied state is localized in two areas of the structure, the first area is below the interface layers and the second area is located deep in the silicon bulk. The distribution of contour lines around the bond between two atoms in both bulk germanium and silicon in this case is referred to as a back-bond state. We have seen such back bond states in the GeSi misaligned interface in Fig. 5.13(b) of Chapter 5 and also on the Ge(001)-(2 $\times$ 1) surface as shown in Fig. 3.2(a) of Chapter 3. This state even though has no contour lines directly around the interface atoms, is an interface state as it has been induced by the interface. The second state shown in Fig. 6.6(b) which is occupied is also a back-bond state and shows the charge density contour lines located around the germanium and silicon interface layers. This state in the band gap is an interface state. It must be noted here that the states shown in Fig. 6.6(a) and Fig. 6.6(b) are displayed in a drawing plane perpendicular to that of the other panels in Fig. 6.6(c) - 6.6(g). The occupied state in Fig. 6.6(c) is also an interface state as the contour lines are around the Ge-S-Si interface, as well as deep in both the germanium and silicon bulk. The occupied states in Fig. 6.6(d) and Fig. 6.6(f), are hybridised states involving the sulfur lone-pair [27] and the silicon and germanium bonding state. The state shown in Fig. 6.6(e)

is a pure sulfur lone-pair state. These states shown in Fig. 6.6(d), Fig. 6.6(e) and Fig. 6.6(f) clearly cut through the band gap in Fig. 6.5(a) are interface states but will not effect the electronic transmission across the interface. The only unoccupied state is the state near the conduction band edge as shown in Fig. 6.6(g) and only appears in the band gap around the $\overline{K}$-point and shows contour lines around the Ge-Ge dimer atoms. As such charge density appears around the interface, it is safe to say this state is an interface state. This state is identical to what we see in the GeSi misaligned interface in Fig. 5.13(e).

In the misaligned interface slab in Fig. 6.5(b) we see two states near the valence band edge, one state across the middle of the gap and one state slightly appearing at $\frac{1}{3}\overline{JK}$. The charge density contour plots for each of these states are shown in Fig. 6.7(a) - 6.7(d), where Fig. 6.7(a) represents the state nearest the valence band edge, ascending in order to Fig. 6.7(d) representing the state nearest the conduction band edge. The charge density for all these states are calculated at $\overline{K}$-point except for the state near the conduction band edge which is calculated at the point $\frac{1}{3}\overline{JK}$.

In Fig. 6.7(a), the charge density contour lines shows a back-bond state deep in the silicon bulk, thus this occupied state in the gap is not an interface state. An occupied interface state is shown in Fig. 6.7(b), where we see what is like a bridge-bond state on the interface germanium atom bridging to the two interface sulfur atoms. The occupied state that crosses through the middle of the band gap is shown in Fig. 6.7(c). This state is an interface state, with a dangling bond on the interface germanium atom. This state is almost identical to the surface state that appears in the projected band structure on the clean Ge(001)-$(2 \times 1)$ surface as presented in Fig. 3.1(b) in Chapter 3 of this thesis. The last state which appears around the point $\frac{1}{3}\overline{JK}$ in Fig. 6.7(d), is an unoccupied interface state with the contour lines appearing over three layers in the silicon bulk as well as the sulfur interface atoms.

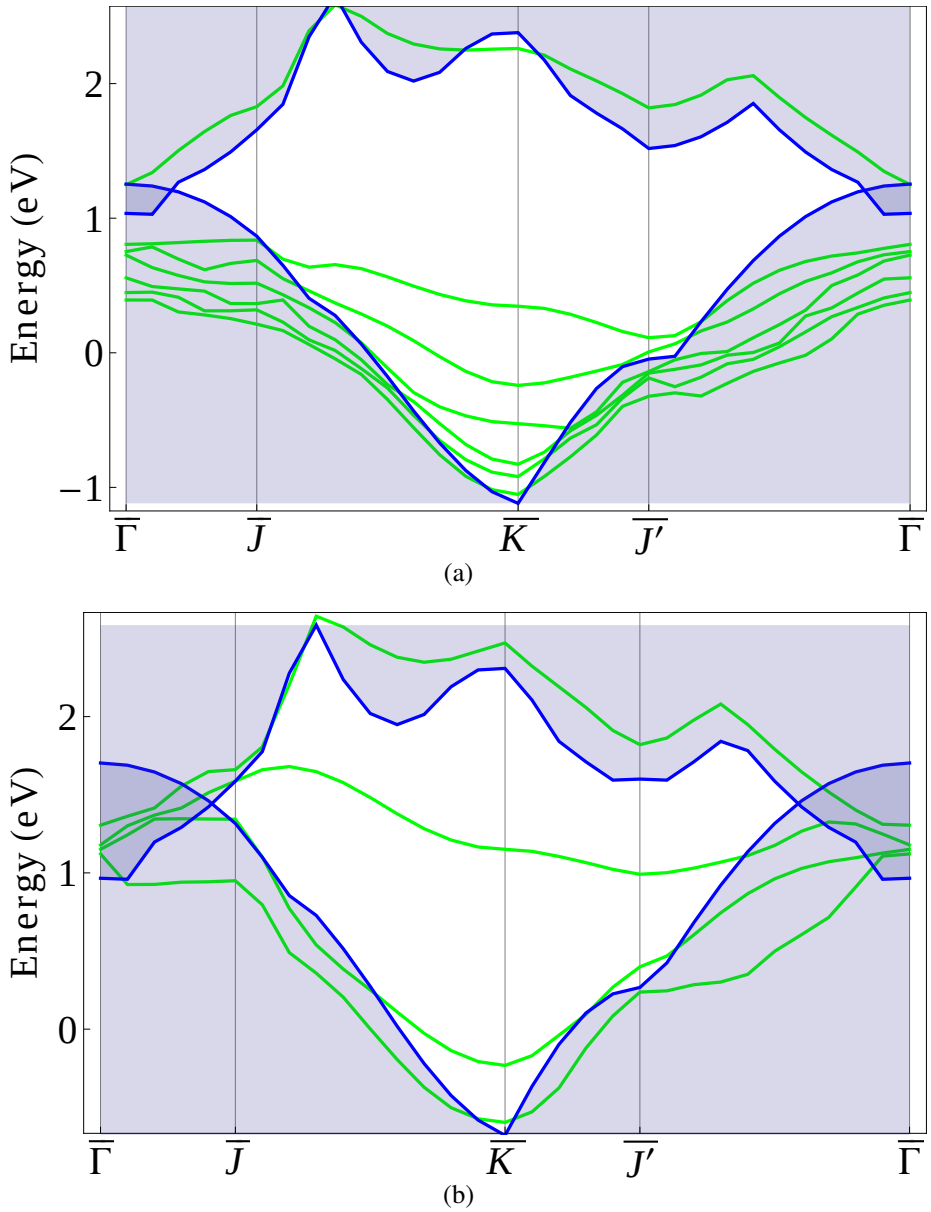


Figure 6.5: Projected electronic bands along the surface path $\overline{\Gamma JKJ'\Gamma}$ in the Brillouin zone using the germanium lattice constant. The slab electronic bands are represented in green and the bulk bands is the shaded area in (a) for the GeSSi aligned interface and (b) for the GeSSi misaligned interface.

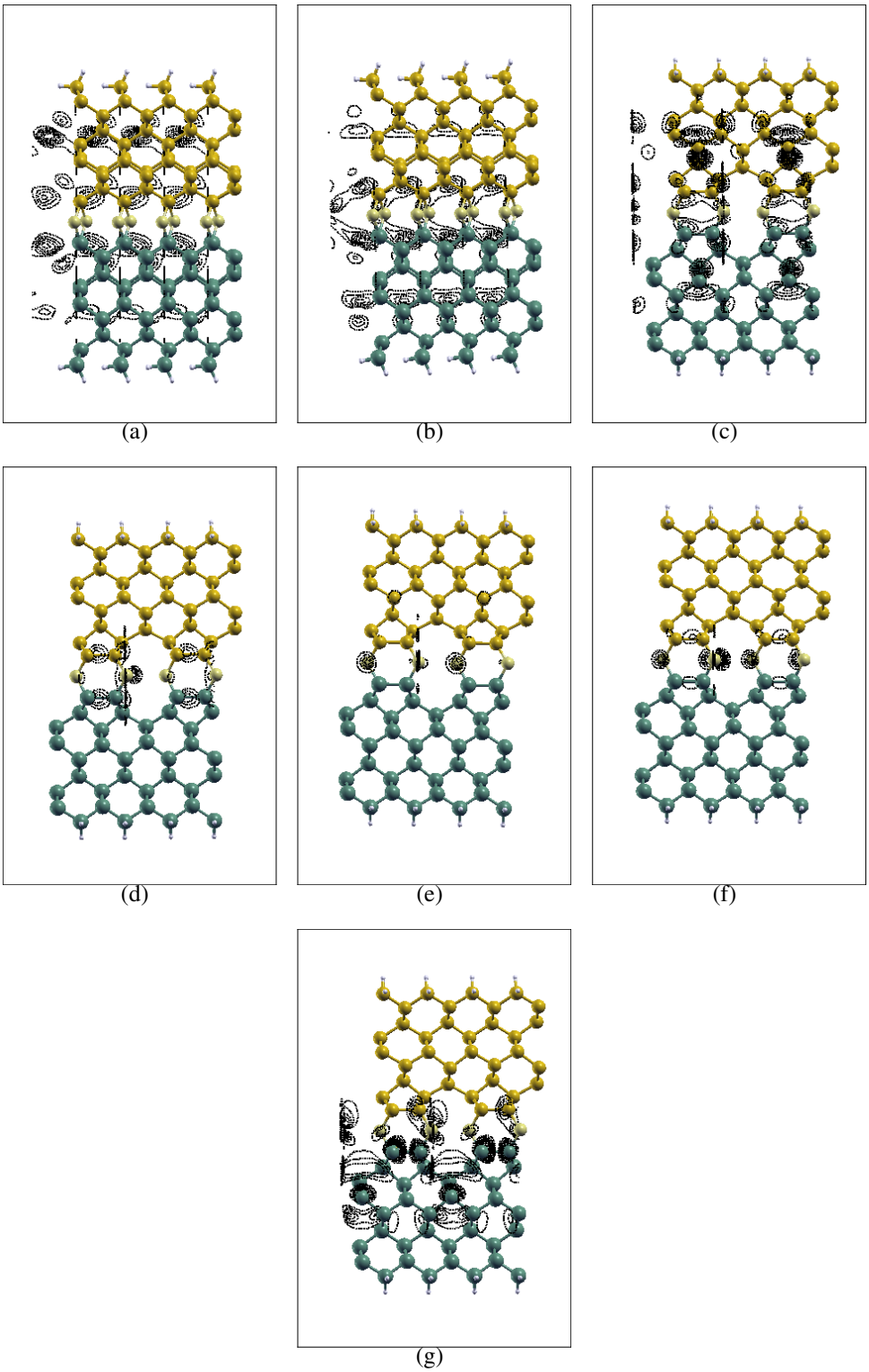


Figure 6.6: The charge density contour plots for the aligned GeSSi interface for the states shown in Fig. 6.5(a). All plots are calculated at the $\overline{K}$-point. (a) represents the state nearest the valence band edge, ascending in order to (g) which representing the state nearest the conduction band edge. Panels (a) and (b) are displayed in a drawing plane perpendicular to that of the other panels.

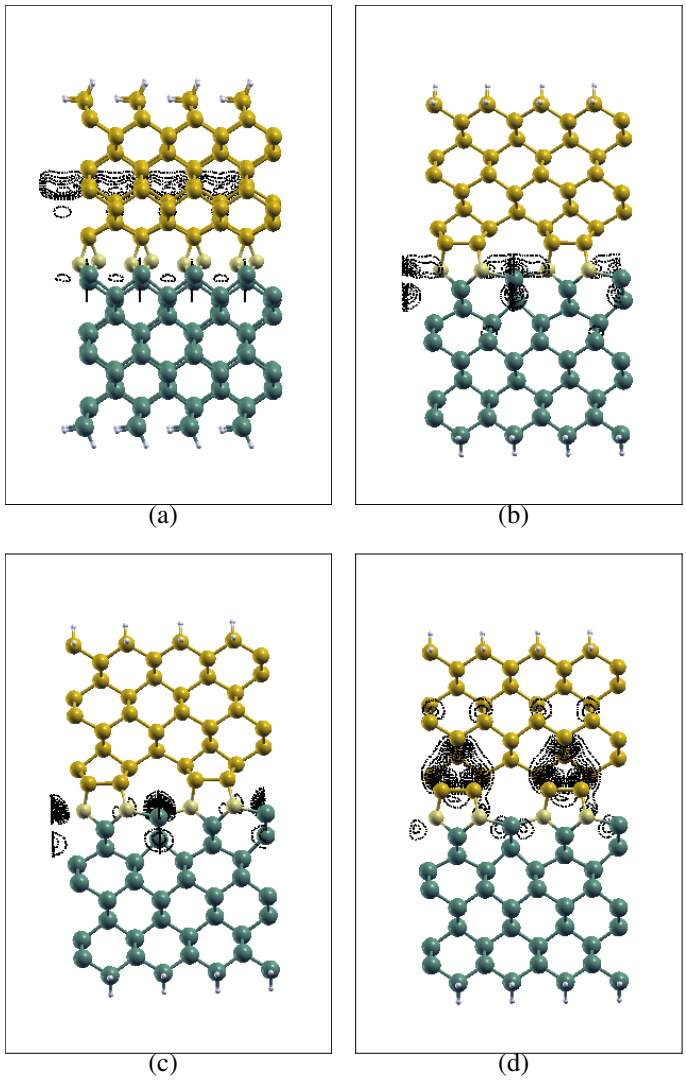


Figure 6.7: The charge density contour plots for the misaligned GeSSi interface for the states shown in Fig. 6.5(b). The plots are calculated at the $\overline{K}$-point for (a)-(c) and at $\frac{1}{3}\overline{JK}$ for (d). (a) represents the state nearest the valence band edge, ascending in order to (d) which representing the state nearest the conduction band edge. Panel (a) is displayed in a drawing plane perpendicular to that of the other panels.

## 6.4 Ge-S-Si Interface using the Si Lattice Constant

The GeSSi aligned and misaligned structures were relaxed using the lattice constant of silicon, at the calculated value of 5.41 Å. The aligned structure shown in Fig. 6.1(a) upon relaxation results in a Ge-S bond lengths of 2.22 Å, a S-Si bond lengths of 2.14 Å and Ge-Ge and Si-Si symmetric dimers of bond length 2.45 Å and 2.39 Å respectively. The misaligned structure is shown in Fig. 6.1(b), with a Si-Si symmetric dimer bond length of 2.36 Å, three Ge-S bond lengths of 2.23 Å, 2.25 Å and 2.44 Å and two S-Si bond length of 2.14 Å and 2.17 Å.

The potential shift calculated using the averaged local potential $\overline{V}_{loc}(z)$ of the aligned and misaligned GeSSi slab as described already in Chapter 5 are $\Delta\overline{V} = 2.33$ eV and $\Delta\overline{V} = 2.49$ eV, respectively. Using the averaged local potential and aligning it with the corresponding bulk averaged potential as described in detail in Section 5.3.2, the values for the energy difference $\Delta E$ are given in Table 6.2.

Table 6.2: Calculated energy shift (in eV) of the average local potential from bulk germanium to that in the germanium side of the GeSSi slab (aligned and misaligned). We also show the corresponding quantities for the strained silicon side of the slab.

| | GeSSi Aligned | GeSSi Misaligned |
|---|---|---|
| $\Delta E_{Ge}$ | $2.93 \pm 0.06$ | $2.83 \pm 0.09$ |
| $\Delta E_{Si}$ | $4.54 \pm 0.11$ | $4.56 \pm 0.12$ |

Using the values for the energy difference in Table 6.2, the projected band structures for the aligned and misaligned interfaces are shown in Fig. 6.8(a) and Fig. 6.8(b), respectively. In the aligned GeSSi interface, the projected band structure shows five states in the band gap near the valence band edge around the $\overline{K}$-point, compared to six in Fig. 6.5(a) where the germanium lattice constant was used. The state near the conduction band edge in Fig. 6.8(a) only appears at the point $\frac{1}{3}\overline{JK}$ and does not appear at

the $\overline{K}$-point as it did in Fig. 6.5(a). Using the silicon lattice constant causes the states nearer the edges to be pushed into the bulk.

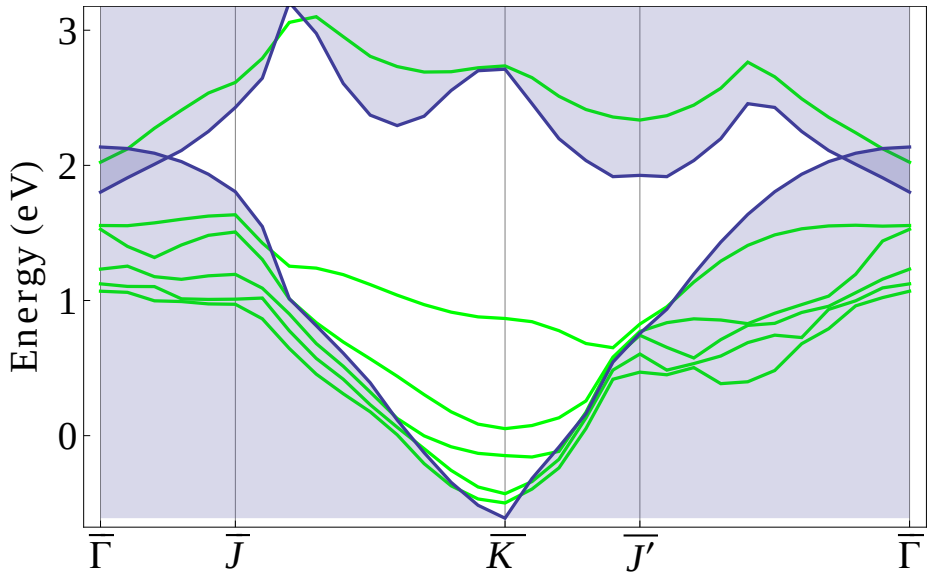


(a)

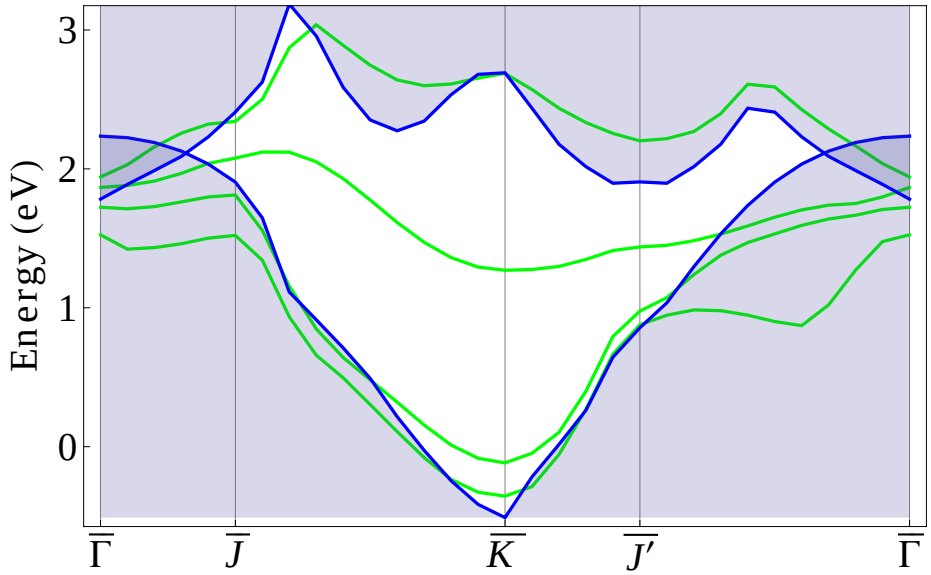


(b)

Figure 6.8: Projected electronic bands along the surface path $\overline{\Gamma JKJ'\Gamma}$ in the Brillouin zone using the silicon lattice constant. The slab electronic bands are represented in green and the bulk bands is the shaded area in (a) for the GeSSi aligned interface and (b) for the GeSSi misaligned interface.

The charge density contour plots for these states in the band gap in Fig. 6.8(a)

are shown in Fig. 6.9(a)- 6.9(f), where Fig. 6.9(a) represents the state nearest the valence band edge, ascending in order to Fig. 6.9(f) representing the state nearest the conduction band edge. The first occupied state shown in Fig. 6.9(a) is an interface state where by the charge density contour lines are seen to be located around the Ge-S-Si atoms in a back bond like state. This state is displayed is in a drawing plane perpendicular to that of the interface in Fig. 6.9(b) . In Fig. 6.9(b) the contour lines are deep in both the germanium and silicon bulk as well as the Ge-S-Si interface which shows that this occupied state is an interface state. The occupied states in Fig. 6.9(c) and Fig. 6.9(e), are hybridised states involving the sulfur lone-pair [27] and the silicon and germanium bonding state. The occupied state shown in Fig. 6.9(d) is a pure sulfur lone-pair state. These states involving the sulfur lone-pair are interface states but are fully occupied and will not effect the electronic transmission across the interface. The final state near the conduction band edge at $\frac{1}{3}\overline{JK}$ which is an unoccupied state, shows contour lines in Fig. 6.9(f) around the Ge-Ge dimer and around the Si-S bond, thus implying this in an interface state.

In the misaligned interface, the projected band structure in Fig. 6.8(b) shows two states near the valence band edge at the $\overline{K}$-point, one state across the middle of the band gap and a state appearing near the conduction band edge between $\overline{J}$ and $\frac{1}{3}\overline{JK}$-point. The charge density contour plots for each of these states are shown in Fig. 6.10(a) - 6.10(d), where Fig. 6.10(a) represents the state nearest the valence band edge, ascending in order to Fig. 6.10(d) representing the state nearest the conduction band edge.

At the $\overline{K}$-point, the charge density plot in Fig. 6.10(a) for the lowest state near the valence band edge is not an interface state, as the contour lines shows a back-bond state deep in the silicon bulk. A bridge-bond state on the interface germanium atom bridging to the interface sulfur atoms is shown in Fig. 6.10(b). This occupied state is an interface state. In Fig. 6.10(c), the occupied state that crosses through the middle of

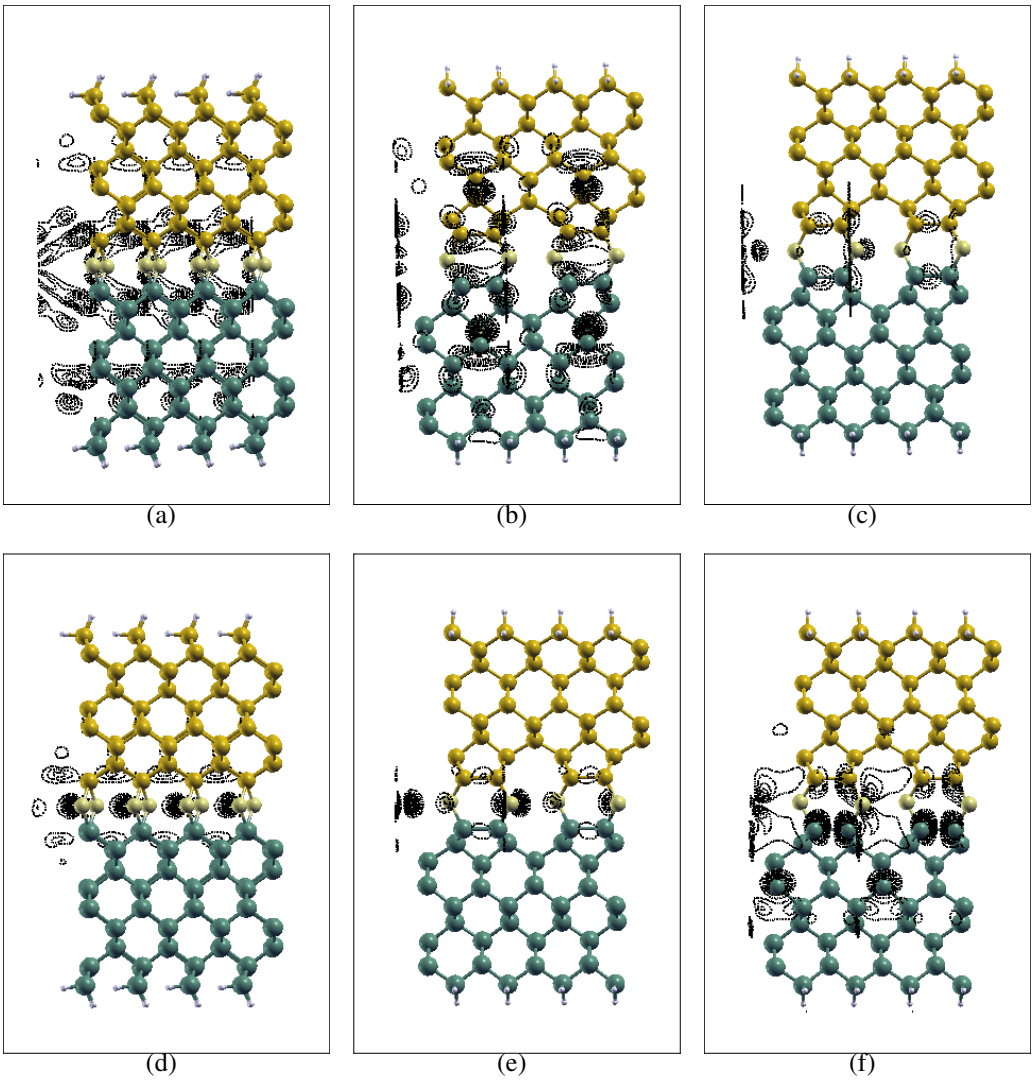


Figure 6.9: The charge density contour plots for the aligned GeSSi interface for the states shown in Fig. 6.8(a). The plots are calculated at the $\overline{K}$-point for (a)-(e) and at $\frac{1}{3}\overline{JK}$ for (f). (a) represents the state nearest the valence band edge, ascending in order to (f) which representing the state nearest the conduction band edge. Panels (a) and (d) are displayed in a drawing plane perpendicular to that of the other panels.

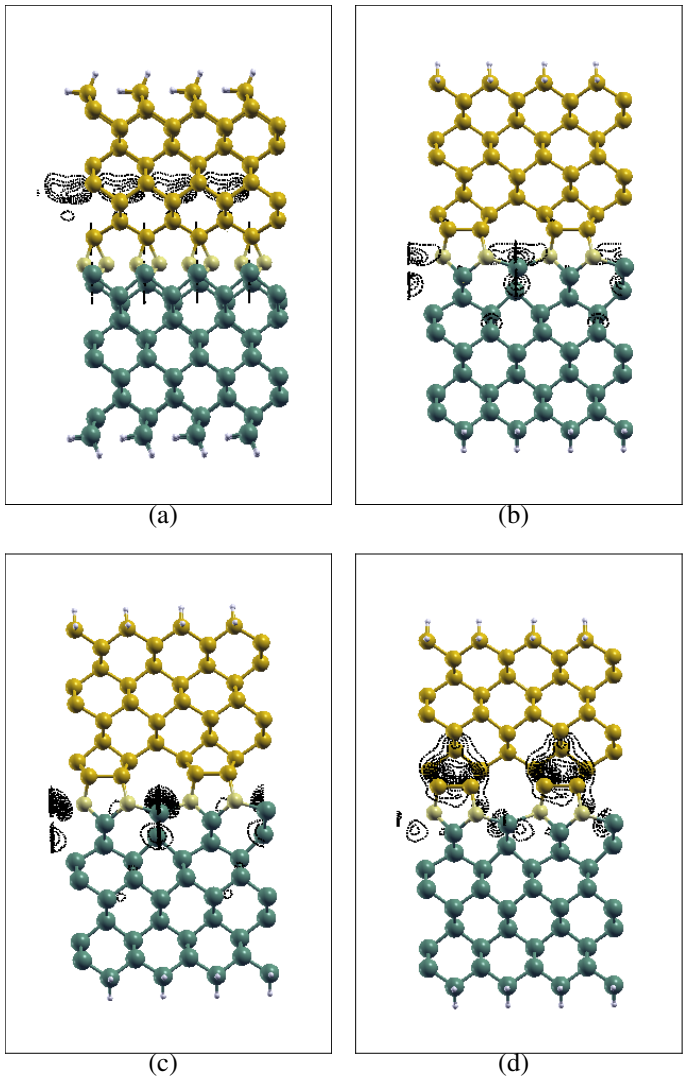


Figure 6.10: The charge density contour plots for the misaligned GeSSi interface for the states shown in Fig. 6.8(b). The plots are calculated at the $\overline{K}$-point for (a)-(c) and at $\frac{1}{3}\overline{JK}$ for (d). (a) represents the state nearest the valence band edge, ascending in order to (d) which representing the state nearest the conduction band edge. Panel (a) is displayed in a drawing plane perpendicular to that of the other panels.

the band gap is an interface state as it can be seen that a dangling bond on the interface germanium atom exists here. Again as with the case of using the germanium lattice constant in Fig. 6.7(c), this state is identical to what we see on clean Ge(001)-(2 × 1) surface in Chapter 3. The unoccupied state in Fig. 6.10(d) calculated at the point $\frac{1}{3}\overline{JK}$ is an interface state due to the contour lines cycling over three atomic layers in the silicon bulk and contour lines around the interface sulfur and germanium atom. It's important to note here that the states calculated using both the germanium and silicon lattice constants in the misaligned GeSSi interface are identical.

## 6.5 Ge-S-H-Si Interface using the Ge Lattice Constant

### 6.5.1 Structural Relaxation

Initially we began our investigation of the GeSHSi interface with using the $H_2S$-terminated Ge(001)-(2 × 1) surface from Chapter 4 with a silicon slab placed over this surface to form the GeSHSi interface, as shown in Fig. 6.11(a) and Fig. 6.11(d) for the aligned and misaligned interfaces, respectively. Using sulfur at the interface does result in a nice chemically bonded region as shown in Fig. 6.1(b) and Fig. 6.1(d), interface states do however exist. As the presence of hydrogen on the $H_2S$-terminated Ge(001)-(2 × 1) surface removed the surface states that were present on the S-passivated Ge(001)-(1 × 1) surface [22], it was important to investigate if the presence of hydrogen on the GeSSi interface would remove the interface states that we have seen and discussed earlier in this Chapter. The structures are relaxed using the same procedure as in Section 5.2, with the three atomic layers on both side of the interface (containing sulfur and hydrogen) only allowed to relax.

Relaxing the interfaces shown in Fig. 6.11(a) and Fig. 6.11(d) for the aligned and misaligned structures respectively, resulted in no bonding of the interface. From here

we artificially broke the H-S bonds on the germanium as shown in Fig. 6.11(b) for the aligned and Fig. 6.11(e) for the misaligned, and allowed these GeSHSi interfaces to relax. The relaxed aligned and misaligned GeSHSi interfaces using the germanium lattice constant are shown in Fig. 6.11(c) and Fig. 6.11(f), respectively. The aligned GeSHSi interface is identical to the aligned GeSSi interface in Fig. 6.1(b) except for the hydrogen molecule being present in the channel between the dimer rows. The misaligned GeSHSi interface is almost identical to the GeSSi interface in Fig. 6.1(d), except for the hydrogen molecule being present in the channel but with one Ge-S bond less than in the GeSSi interface.

To further investigate if both these aligned and misaligned GeSHSi interfaces were the minimum energy structures, we artificially moved the hydrogen molecule to different locations in the channels between the adjacent Ge-S-Si rings and re-relaxed the structures. This was done to see if the hydrogen molecule would split and bond to any dangling bonds that may be present on the germanium, sulfur or silicon atoms at the interface. All our test calculations showed that the structures shown in Fig. 6.11(c) and Fig. 6.11(f) are the true minimum energy relaxed interface geometries.

In the aligned interface the relaxed structure gives a Ge-S bond lengths of 2.21 Å, a S-Si bond lengths of 2.15 Å and a Ge-Ge and Si-Si symmetric dimers of bond length 2.45 Å and 2.41 Å respectively. The relaxed misaligned interface results in a Si-Si symmetric dimer bond length of 2.38 Å, three Ge-S bond lengths of 2.22 Å, 2.25 Å and 2.48 Å and two S-Si bond length of 2.15 Å and 2.18 Å respectively.

The layer separation for the aligned and misaligned lattices are shown in Fig. 6.12(a)-6.12(d). As we are using the germanium lattice constant, we see as we did in Chapter 5 and earlier in this chapter, the silicon strains in the perpendicular direction as expected.

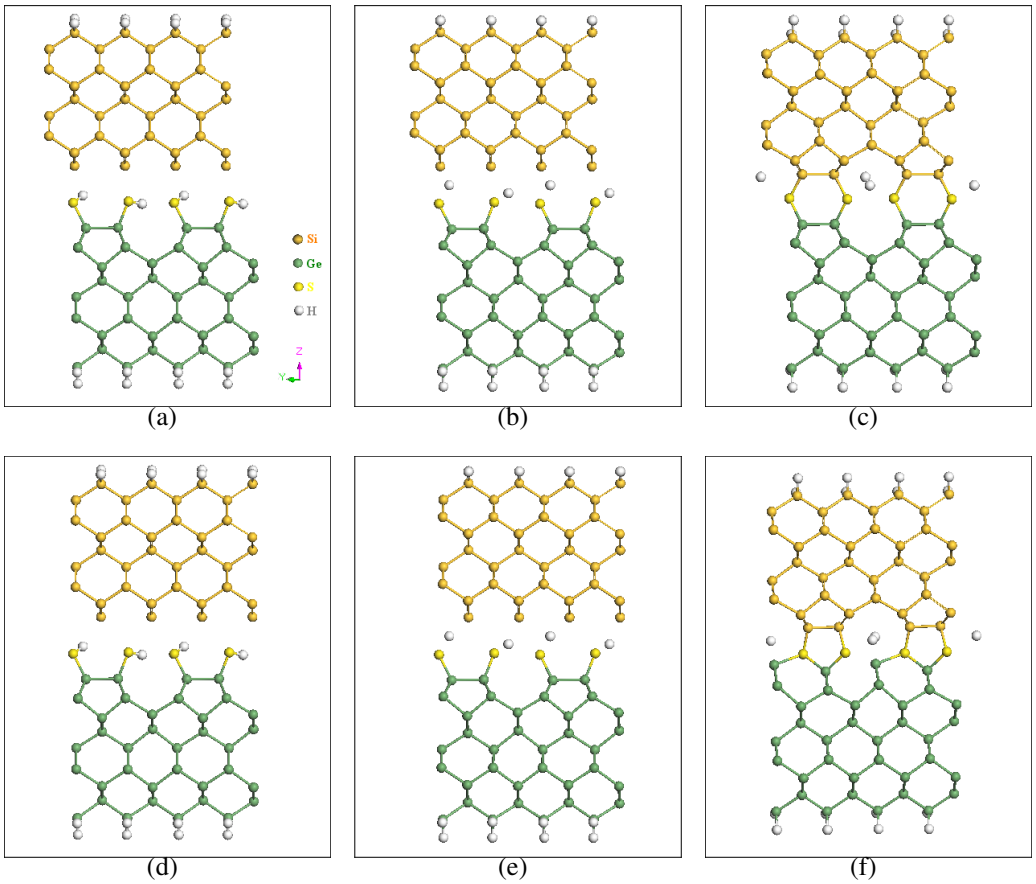


Figure 6.11: (a) The initial atomic configuration of the GeSHSi aligned structure. (b) The S-H bonds are broken to help initiate the bonding at the interface. (c) After structural relaxation the final atomic configuration of the GeSHSi aligned structure showing a GeSHSi(001)-$(2 \times 1)$ reconstruction with the presence of Ge-Ge and Si-Si symmetric dimers and a hydrogen molecule in the channel. (d) The initial atomic configuration of the GeSHSi misaligned structure. (e) The S-H bonds are broken to help initiate the bonding at the interface. (f) The final relaxed geometry for the misaligned structure showing a GeSHSi(001)-$(2 \times 1)$ interface with Si-Si dimer only.

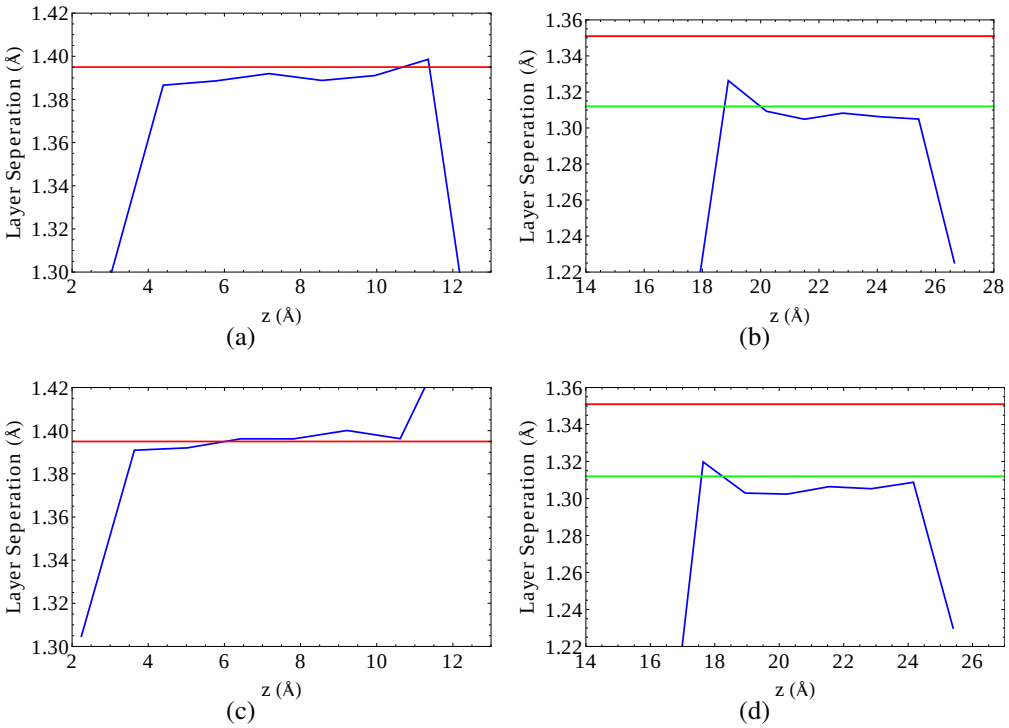


Figure 6.12: Atomic layer separation $d$ (blue line) in the relaxed GeSHSi slab as a function of position $z$ perpendicular to the plane of the interface. The region with $z < 13$ Å [in (a) and (c)] is unstrained germanium and region the with $z > 17$ Å [in (b) and (d)] is silicon with the in-plane lattice constant matched to unstrained germanium. Panels (a) and (b) show results for the "aligned" interface geometry and panels (c) and (d) show results for the "misaligned" geometry. The red lines indicate the corresponding unstrained bulk layer separation and the green line indicates the $z$ interlayer separation found in bulk silicon, when its $x-y$ lattice constant is constrained to match that of unstrained germanium.

### 6.5.2 Band Lineup and Projected Band Structure

The averaged local potential is shown in Fig. 6.13(a) and Fig. 6.13(b) for the aligned and misaligned interfaces respectively. Due to the presence of hydrogen molecule in the interface region, these potentials are only slightly different to the local potentials of the GeSSi interfaces in Fig. 6.3(a) and Fig. 6.3(b).

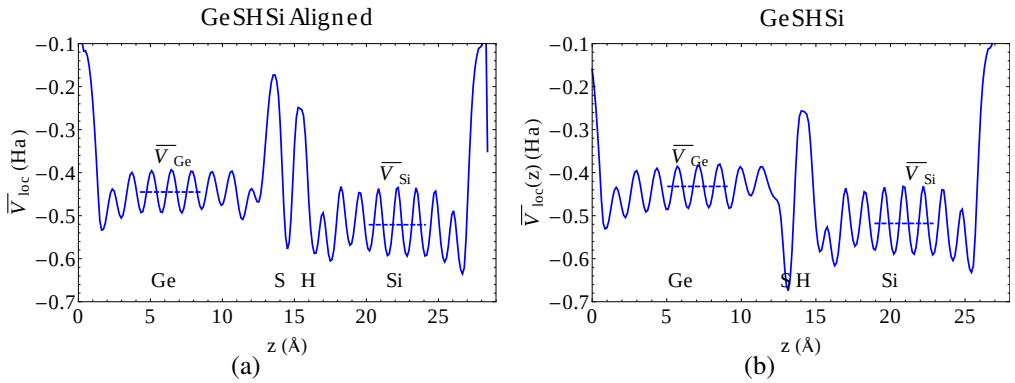


Figure 6.13: The local potential $\overline{V}_{loc}(z)$ averaged over the parallel components $x$ and $y$ as a function of the perpendicular coordinate $z$, to the interface for (a) the aligned and (b) misaligned GeSHSi interface. The dashed line in both the germanium and silicon is represented as $\overline{V}_{Ge}$ and $\overline{V}_{Si}$, respectively, defined as the average local potential over three periodic potential cycles in each section of the slab. Ge, S, H and Si represent the regions in the slab where the germanium, sulfur, hydrogen and silicon atoms are located.

The potential shift $\Delta\overline{V}$ defined in Eq. 5.2 as $\Delta\overline{V} = \overline{V}_{Ge} - \overline{V}_{Si}$ for the aligned and misaligned structures are 2.07 eV and 2.32 eV, respectively. The energy difference $\Delta E$ defined as the difference in energy between the bulk potential and the corresponding part of the slab potential for the aligned and misaligned GeSHSi interface are shown in Table 6.3.

The projected band structures for the GeSHSi aligned and misaligned interfaces are aligned with the corresponding projected bulk band structures using the energy difference values in Table 6.3. The projected band structure of both are shown in Fig. 6.14(a) and Fig. 6.14(b).

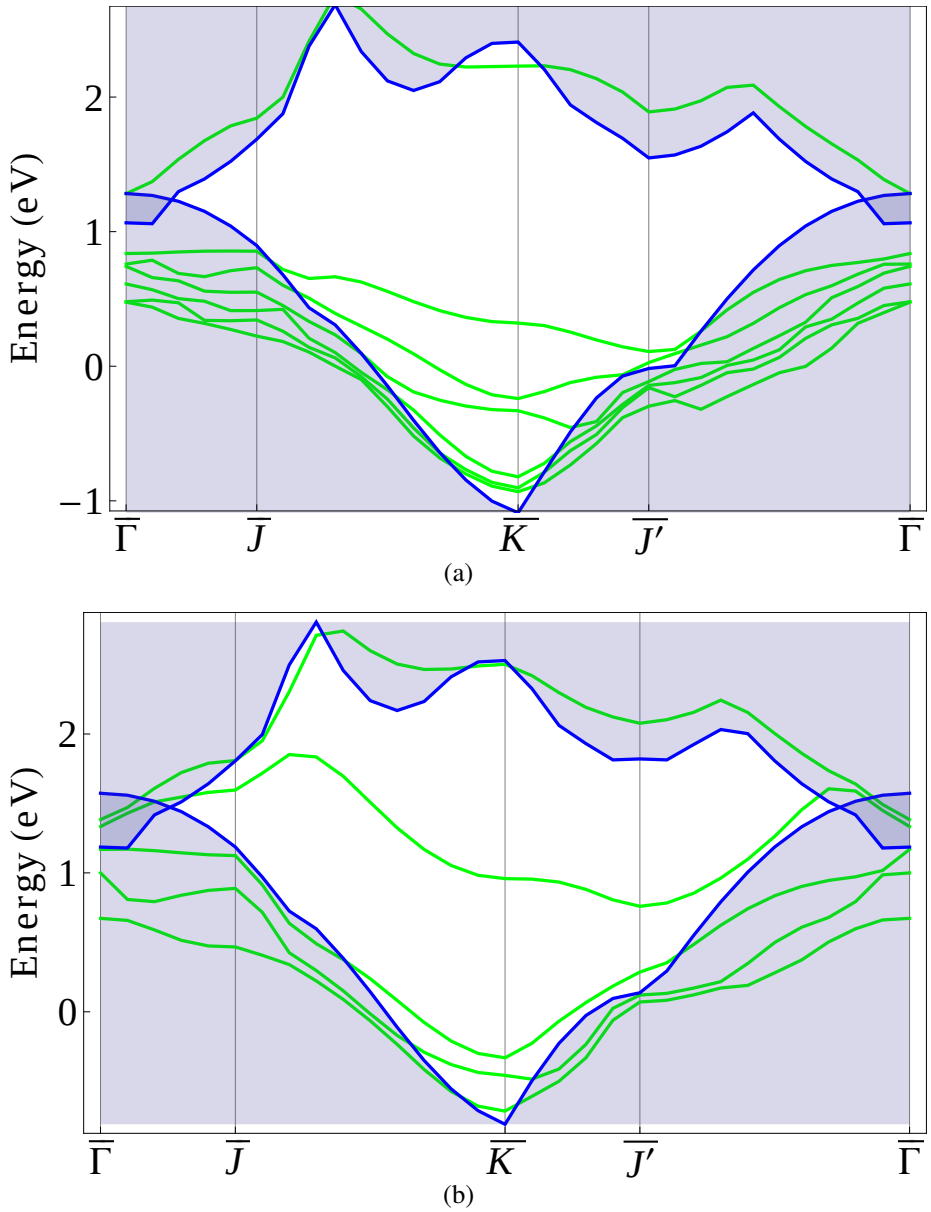


Figure 6.14: Projected electronic bands along the surface path $\overline{\Gamma JKJ'\Gamma}$ in the Brillouin zone using the germanium lattice constant. The slab electronic bands are represented in green and the bulk bands is the shaded area in (a) for the GeSHSi aligned interface and (b) for the GeSHSi misaligned interface.

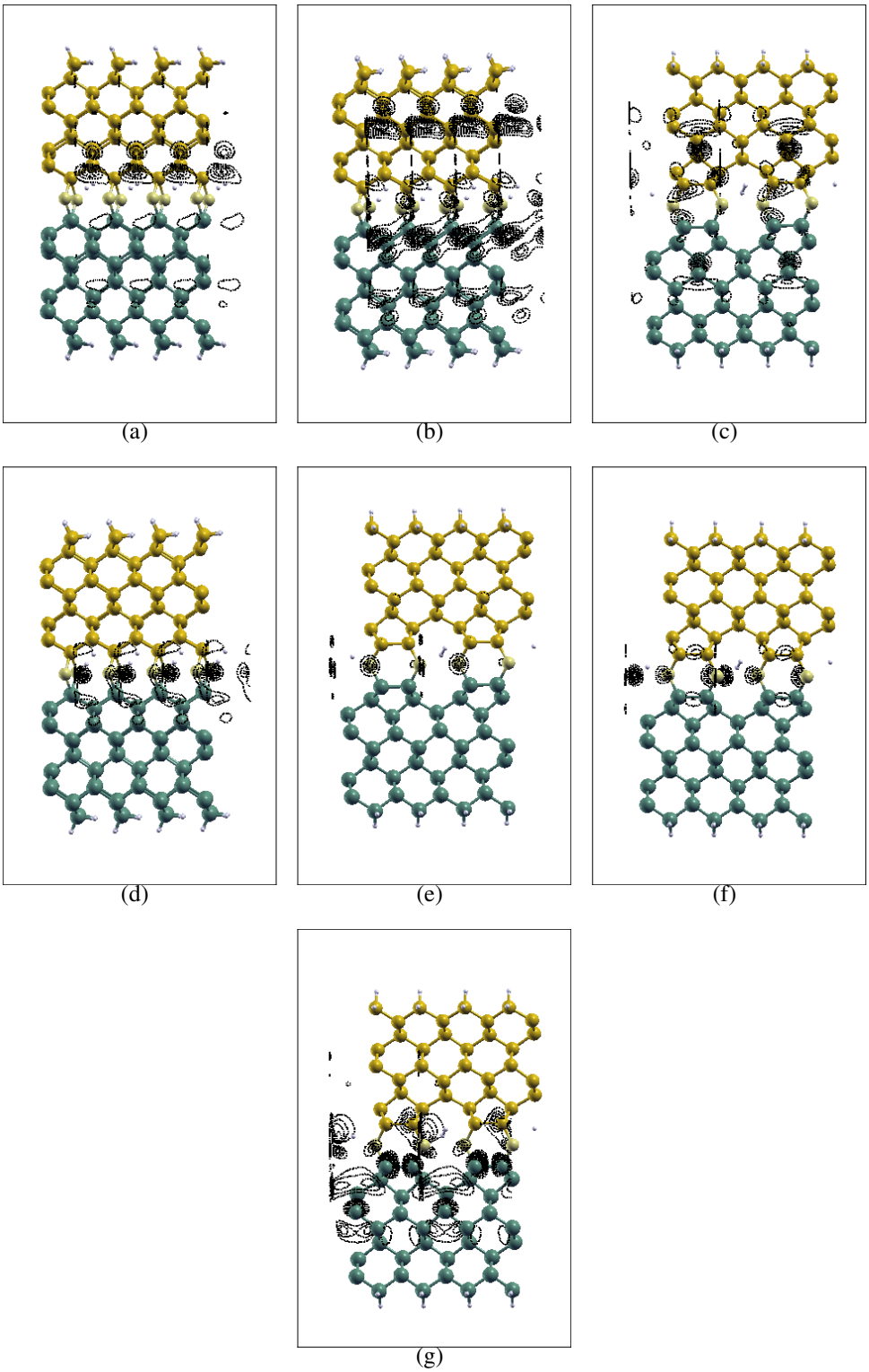


Figure 6.15: Charge density contour plots for the aligned GeSHSi interface for the states shown in Fig. 6.14(a). All plots are calculated at the $\overline{K}$-point. (a) represents the state nearest the valence band edge, ascending in order to (g) which representing the state nearest the conduction band edge. Panels (a), (b) and (d) are displayed in a drawing plane perpendicular to that of the other panels.

Table 6.3: Calculated energy shift (in eV) of the average local potential from bulk germanium to that in the germanuim side of the GeSHSi slab (aligned and misaligned). We also show the corresponding quantities for the strained silicon side of the slab. The energy difference $\Delta E$ is defined in Eq. 5.2.

| | GeSHSi Aligned | GeSHSi Misaligned |
|---|---|---|
| $\Delta E_{Ge}$ | $3.23 \pm 0.05$ | $2.94 \pm 0.09$ |
| $\Delta E_{Si}$ | $4.66 \pm 0.10$ | $4.54 \pm 0.15$ |

In Fig. 6.15(a)- 6.15(g) all these charge density plots are calculated at the $\overline{K}$-point and Fig. 6.15(a) represents the state in the band gap in Fig. 6.14(a) nearest the valence band edge ascending in order to the state nearest the conduction band edge where the charge density is shown in Fig. 6.15(g). The contour lines in Fig. 6.15(a) represent a back-bond state near the interface silicon atoms. The charge density in Fig. 6.15(b) shows a back-bond state in the germanium layer near the interface and a bridge-bond state deep in the silicon bulk. In Fig. 6.15(c), contour lines are located on the Ge-S-Si interface. These three states which are all occupied all represent interface states. The occupied states in Fig. 6.15(d) and Fig. 6.15(f), are hybridised states involving the sulfur lone-pair [27] and the silicon and germanium bonding state. The occupied state shown in Fig. 6.15(e) is a pure sulfur lone-pair state. These lone-pair states clearly cut through the band gap in Fig. 6.14(a) are interface states but will not affect the electronic transmission across the interface. The final state shown in Fig. 6.15(g) which is also the only unoccupied state shows contour lines around the Ge-Ge dimer atoms, thus implying an interface state. It must be noted here that all the interface states are indistinguishable from the interface states in the GeSSi aligned interface and the presence of the hydrogen molecule does not influence the electronic characteristics of the interface.

The misaligned interface in Fig. 6.14(b) we see three states near the valence band edge, one state across the middle of the gap and another one appearing around $\frac{1}{3}\overline{JK}$. The charge density of the lowest state in the gap is represented in Fig. 6.16(a) and

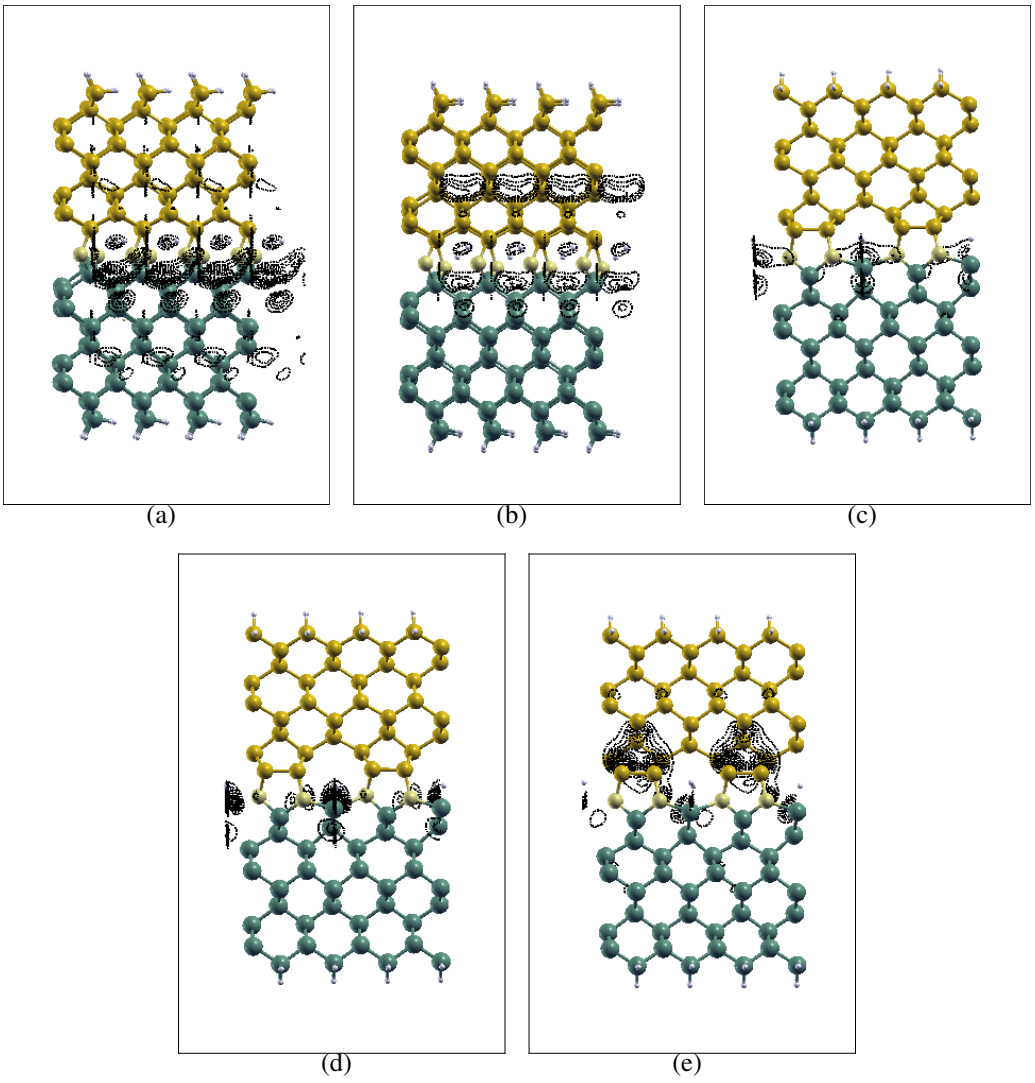


Figure 6.16: The charge density contour plots for the misaligned GeSHSi interface for the states shown in Fig. 6.14(b). The plots are calculated at the $\overline{K}$-point for (a)-(d) and at $\frac{1}{3}\overline{JK}$ for (e). (a) represents the state nearest the valence band edge, ascending in order to (e) which representing the state nearest the conduction band edge. Panel (a) and (b) are displayed in a drawing plane perpendicular to that of the other panels.

ascending in order to the state nearest the conduction band edge where the charge density is shown in Fig. 6.16(e). The charge density for all these states are calculated at the $\overline{K}$-point except for the state near the conduction band edge, which is calculated at the point $\frac{1}{3}\overline{JK}$.

In Fig. 6.16(a) is a back-bond state where the charge density is located on a Ge-Ge bond below the interface. This occupied interface state is not seen in the projected band structure of the GeSSi misaligned interface in Fig. 6.5(b). The occupied state shown in Fig. 6.16(b) is again another back-bond state and is located deep in the silicon bulk and contour lines are around the interface germanium atoms implying that this is an interface state. The next interface state which is occupied is shown in Fig. 6.16(c) where we see a bridge-bond state on the interface germanium atom bridging also to the interface sulfur atoms. Another interface state is seen in Fig. 6.16(d) where the charge density contour lines are located on the interface germanium atom, forming a dangling bond. This occupied state is represented in the projected band structure in Fig. 6.14(b) is the one that crosses the middle of the gap and as mentioned in Section 6.3.3 this state is similar to the dangling bond state on the Ge(001)-$(2 \times 1)$ surface. The final state that appears around $\frac{1}{3}\overline{JK}$ is shown in Fig. 6.16(e) has the largest proportion of charge density located over three atomic layers in the silicon bulk and has contour lines around the sulfur and germanium interface atoms again implying that this is an interface state. This is the only unoccupied state in the band gap. In this GeSHSi misaligned interface, the only difference with the GeSSi misaligned interface is the presence of an extra state with the presence of hydrogen. This state is the one shown in Fig. 6.16(a). The presence of the hydrogen molecule does not influence the electronic characteristics of the misaligned interface. The hydrogen molecule in both the aligned and misaligned GeSHSi interfaces does not remove any of the interface states that were present in the GeSSi interfaces.

## 6.6 Ge-S-H-Si Interface using the Si Lattice Constant

Using the lattice constant of silicon, the GeSHSi aligned and misaligned interfaces are re-relaxed as shown in Fig. 6.11(c) and Fig. 6.11(f). In the aligned interface the relaxed structure gives Ge-S bond lengths of 2.20 Å and 2.21 Å, a S-Si bond lengths of 2.15 Å and a Ge-Ge and Si-Si symmetric dimers of bond length 2.42 Å and 2.39 Å, respectively. The relaxed misaligned interface results in a Si-Si symmetric dimer bond length of 2.35 Å, three Ge-S bond lengths of 2.23 Å, 2.26 Å and 2.42 Å and two S-Si bond length of 2.14 Å and 2.18 Å, respectively.

The potential shift $\Delta V$ defined in Eq. 5.2 for the aligned and misaligned structures are 2.36 eV and 2.48 eV, respectively. The energy difference $\Delta E$ defined as the difference in energy between the bulk potential and the corresponding part of the slab potential for the aligned and misaligned GeSHSi interface are shown in Table 6.4.

Table 6.4: Calculated energy shift (in eV) of the average local potential from strained germanium to that in the germanium side of the GeSi slab (aligned and misaligned). We also show the corresponding quantities for the silicon side of the slab. The energy difference $\Delta E$ is defined in Eq. 5.2.

| | GeSHSi Aligned | GeSHSi Misaligned |
|---|---|---|
| $\Delta E_{Ge}$ | $2.90 \pm 0.07$ | $2.81 \pm 0.05$ |
| $\Delta E_{Si}$ | $4.48 \pm 0.19$ | $4.53 \pm 0.12$ |

The projected band structures for the aligned and misaligned interfaces are aligned with the corresponding projected bulk band structures using the energy difference values in Table 6.4. The projected band structure of both are shown in Fig. 6.17(a) and Fig. 6.17(b).

For the aligned GeSHSi interface, six states appear in the band gap of the projected band structure. The corresponding charge density contour plots for these six states are shown in Fig. 6.18(a)- 6.18(f) where the charge density for each of these bands is calculated at the $\overline{K}$-point. The lowest state in the band gap near the valence band edge

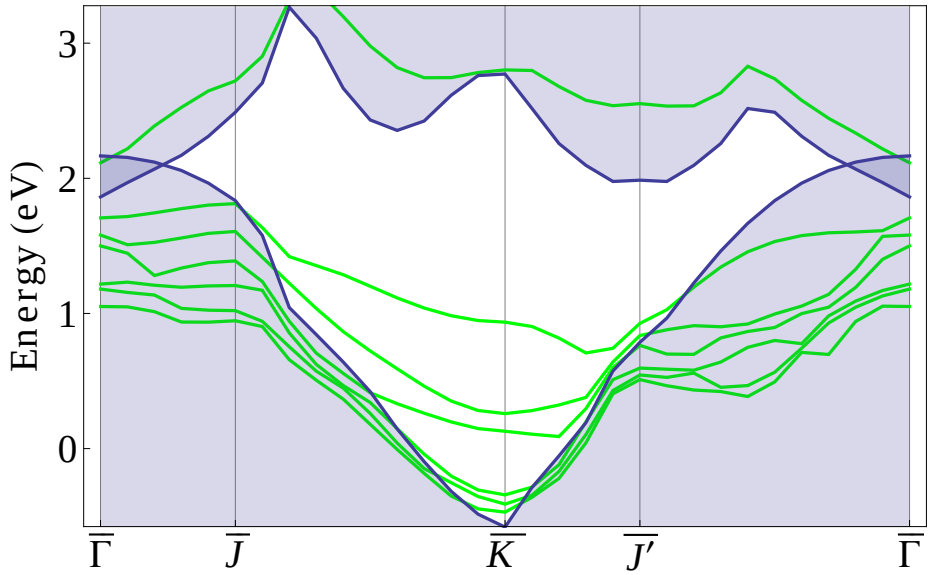


(a)

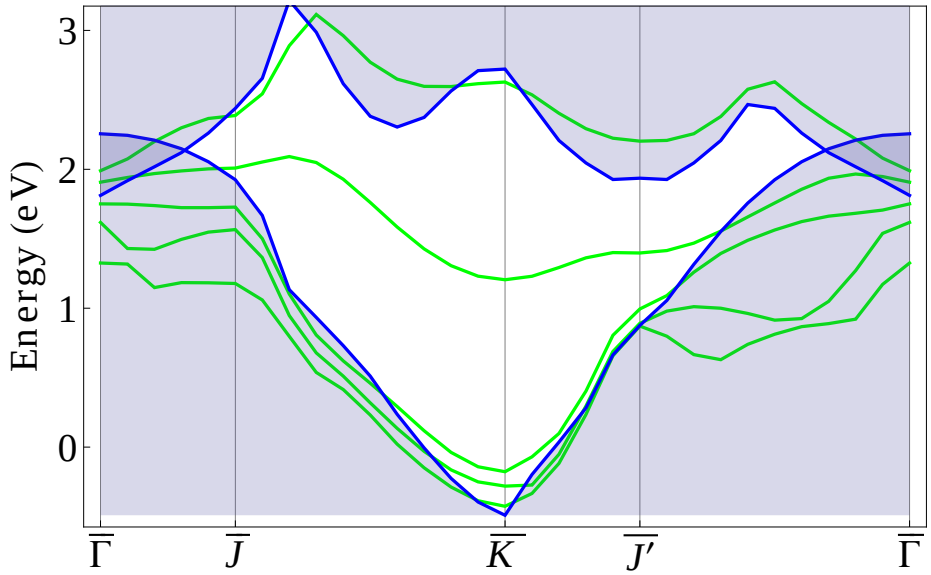


(b)

Figure 6.17: (a) Projected electronic bands for the GeSHSi aligned interface along the surface path $\overline{\Gamma JKJ'\Gamma}$ in the Brillouin zone using the silicon lattice constant. The slab electronic bands are represented in green and the bulk bands are the shaded area. Six states exist in the band gap. (b) The projected band structure for the misaligned interface with the of presence five states in the band gap.

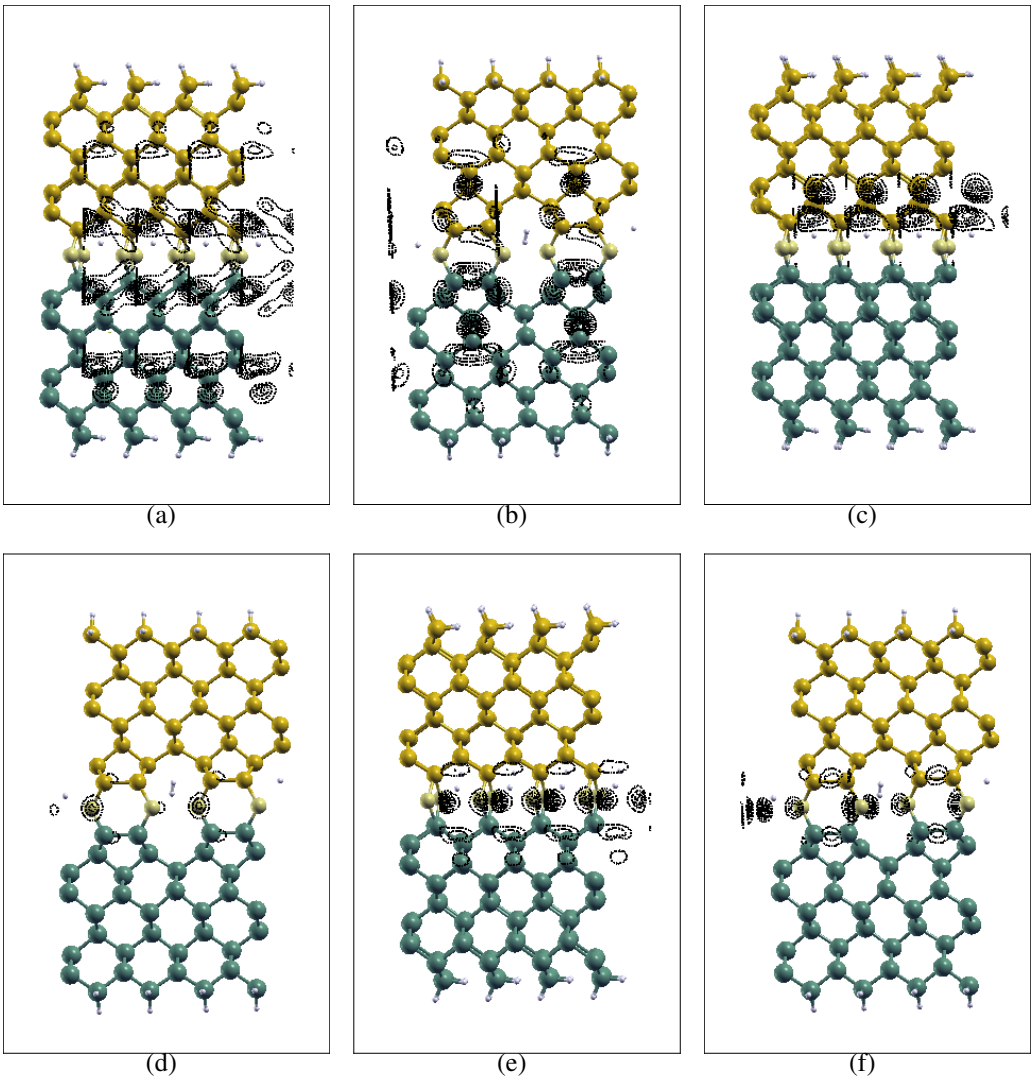


Figure 6.18: Charge density contour plots of the individual states for the GeSHSi aligned interface at the $\overline{K}$-point for (a)-(f). All plots are calculated using the silicon lattice constant. (a) shows back-bond states in both the germanium and silicon bulk and is represented in a drawing plane perpendicular to the other panels. (b) and (c) are bridge-bond states in the bulk. (d)-(f) represent interface states on the sulfur atoms.

as shown in Fig. 6.18(a) is a back-bond state with the contour lines around both a Si-Si and Ge-Ge bonds at the interface. This occupied state is an interface state. A mixture of a back-bond and bridge-bond state is shown in Fig. 6.18(b). The contour lines are mainly situated in the bulk however contour lines are seen around the Ge-Ge dimer and S-Si bond thus this occupied state is referred to as an interface state. In the silicon layer at the interface in Fig. 6.18(c) another back-bond and interface state is seen which is also occupied. The occupied state shown in Fig. 6.18(d) is a pure sulfur lone-pair state. The occupied states in Fig. 6.18(e) and Fig. 6.18(f), are hybridised states involving the sulfur lone-pair [27] and the silicon and germanium bonding state. These lone-pair states are all interface states but will not effect the electronic transmission across the interface. In comparison to the charge density plots of the aligned GeSHSi interface using the germanium lattice constant Fig. 6.15(a)-6.15(f), we see bridge and back bond states in both that are interface states. We see three interface states related to the sulfur lone-pairs, however we see an interface state due to the Ge-Ge dimer in the germanium lattice constant case. This was only visible in the projected band structure around the $\overline{K}$-point as shown in Fig. 6.14(a). This is not seen in the projected band structure in Fig. 6.17(a) where we used the silicon lattice constant.

The misaligned GeSHSi interface projected band structure in Fig. 6.17(b) shows three states near the valence band edge, one state directly across the band gap and the final state near the conduction band edge. All charge density plots for these states shown in Fig. 6.19(a)- 6.19(e) are calculated at the $\overline{K}$-point. The charge density plots in Fig. 6.19(a) and Fig. 6.19(b) which are interface states are shown in a perpendicular drawing plane to the charge density plots in Fig. 6.19(c)- 6.19(e). In Fig. 6.19(a) we see a back-bond interface state on the germanium atom at the interface and also in Fig. 6.19(b). An interface state is shown in Fig. 6.19(c), where we see a bridge-bond on the interface germanium atom bridging to the interface sulfur atoms. Another

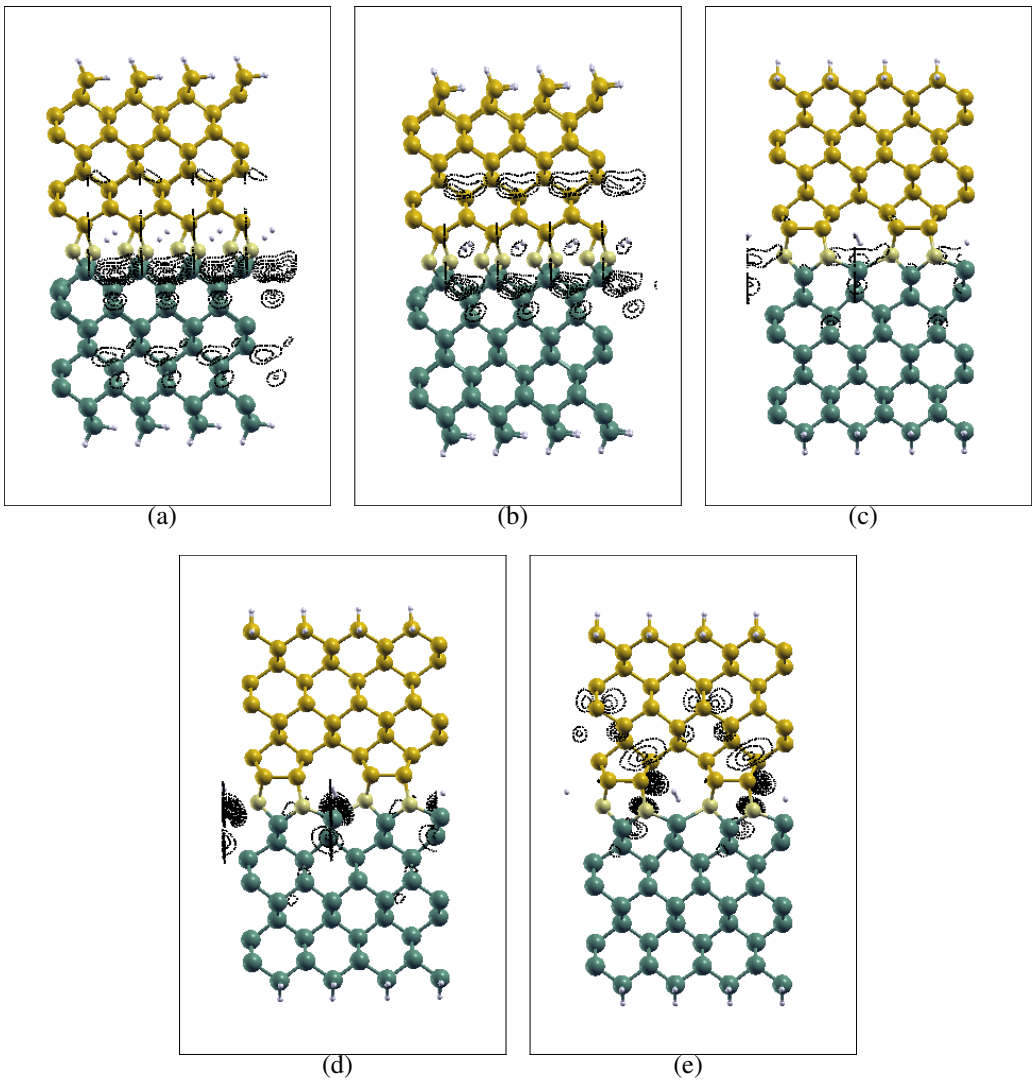


Figure 6.19: Charge density contour plots of the individual states for the GeSHSi misaligned interface at the $\overline{K}$-point for (a)-(c) and at $\frac{1}{3}\overline{JK}$ for (d). All plots are calculated using the silicon lattice constant. (a) and (b) are bridge-bond states in the germanium bulk and are drawn in a plane perpendicular to the other panels. (c) is an interface state with bridge-bond state on the interface germanium atom bridging to the interface sulfur atoms. (d) is a dangling bond interface state on the interface germanium atom. (e) shows the interfaces state with contour lines on the interface silicon and sulfur atoms.

interface state is shown in Fig. 6.19(d), which is the state that runs directly across the middle of the band gap, is like a dangling bond state on the interface germanium atom. This state as already mentioned in the case of the misaligned interface using the germanium lattice constant in this Chapter is equivalent to the dangling bond state on the Ge(001)-$(2 \times 1)$ surface. All these states are occupied. The final state near the conduction band edge is shown in Fig. 6.19(e) is an interface state and is the only unoccupied state. The contour lines are located around one of the sulfur interface atoms and also on one of the silicon atoms on the Si-Si dimer.

## 6.7 Conclusion

In conclusion, calculations for both structural geometries and electronic band structures using both the germanium and silicon lattice constants were performed. The GeSSi aligned interface forms a $(2 \times 1)$ structure with a ring of Ge-S-Si-Si-S-Ge atoms. Ge-Ge and Si-Si symmetric dimers exist on this six atom ring. The projected band structure for this interface using the germanium lattice constant shows seven interface states in the band gap with six of these states being nearer the valence band side. The state nearest the valence band edge does not appear in the projected band structure using the silicon lattice constant. In both cases of using different lattice constants, only one unoccupied state exists in each. This is the state that is near the conduction band edge.

In the GeSSi misaligned interface a $(2 \times 1)$ structure is formed with the presence of Si-Si dimers only. No Ge-Ge dimers are present as the sulfur bonds to germanium like the GeS$(1 \times 1)$ structure. The projected band structure for this interface state shows four states in the band gap. In both the aligned and misaligned cases of the GeSSi interface, interface states exist due to the presence of the sulfur atoms. The states in the aligned structures are fully occupied and are due to the presence of the

sulfur lone-pairs. The states in the misaligned structures which are also fully occupied are due to bridge-bonds between the Ge-S bonds, Sulfur here forms 3 bonds with its neighbouring germanium and silicon atoms and thus the six valence electrons of sulfur are used in these bonds. Without the presence of sulfur we saw in Chapter 5 that the GeSi misaligned structure had one unoccupied interface state and we proposed that the use of sulfur with its flexible chemical bonds would remove this interface state. However this was not the case as the unoccupied state near the conduction band edge remained when sulfur was used at the interface. From this sulfur does not improve the interface and the electronic trap still remains which may be an issue in the production of the GeSi APD.

Introducing the hydrogen molecule into the GeSSi interfaces, the aligned GeSHSi interface is identical to the aligned GeSSi interface except for the hydrogen molecule being present in the channel between the dimer rows. Similarly the misaligned GeSHSi interface is almost identical to the GeSSi interface except for the hydrogen molecule being present but with one Ge-S bond less than in the GeSSi interface. The aligned GeSHSi shows seven interface states in the projected band structure using the germanium lattice constant and shows six states using the silicon lattice constant whereby the state near the conduction band edge does not appear in the projected band structure.

The misaligned GeSHSi interface shows five interface states in using both the germanium and silicon lattice constants respectively.

As originally suggested from our knowledge of the GeSH surface whereby the presence of hydrogen removed the surface states, the presence of hydrogen on the GeSSi interfaces did not influence the electronic characteristics of the interfaces. The unoccupied interface state around the conduction band edge still remained in both the aligned and misaligned structures. The introduction of the hydrogen molecule with the hope of atomic hydrogen bonding with the unoccupied state did not occur in both

the aligned and misaligned GeSHSi interfaces.

To conclude the original unoccupied interface state that existed in the GeSi misaligned interface remained throughout. The presence of sulfur and hydrogen did not remove this state. Using S and HS on the GeSi interface provided some interesting bonding configurations, however the single interface state has the potential to be a problem in the development of the GeSi avalanche photodiode.

CHAPTER 7

# Conclusion

This theoretical study was to investigate various aspects of the bonding, vibrational modes and electronic structure of GeSi surfaces and interfaces. It was originally stimulated by the possibilities for development of GeSi avalanche photodiodes using wafer-bonding techniques to create the GeSi interface.

As a benchmarking exercise we first looked at the bare germanium surface and using density functional theory (DFT) we reproduced the theoretical results as published in the literature of a Ge(001)-$(2 \times 1)$ surface. The asymmetric dimer is produced at the Ge(001)-$(2 \times 1)$ surface. The projected band structure shows distinct states in the band gap. These were two dangling-bond states on the surface germanium atoms and a back-bond surface state on a germanium atom below the surface. This then provided us with the correct foundations using DFT, to investigate theoretically the vibrational mode frequencies of adsorbed species on a germanium surfaces and the GeSi interfaces.

The equilibrium geometry and vibrational modes of $H_2S$ and $H_2O$-terminated Ge(001)-$(2 \times 1)$ surfaces were calculated in a supercell approach using first-principles density functional theory in the local density (LDA), generalized gradient (GGA) approximations and van der Waals (vdW) interactions. We saw both similarities and differences in the bonding of $H_2S$ and $H_2O$ to the Ge(001)-$(2 \times 1)$ surface. The differences between the exchange-correlation functionals including vdW terms and the

LDA or GGA are less than the differences between LDA and GGA, thus vdW does not greatly alter the vibrational mode frequencies. The calculated localized mode frequencies, particularly the Ge-S and Ge-O stretch modes, provide useful vibrational signatures of bonding of both sulfur and oxygen on Ge(001)-(2x1) surface, which may be compared with vibrational spectroscopy measurements. The Ge-H stretch and bending modes are characteristic in identifying the difference between two different $H_2O$ to the Ge(001)-$(2 \times 1)$ surfaces.

The structural and electronic characteristics of a GeSi(001) interface were calculated for regions where the germanium and silicon atoms align and misalign. The GeSi aligned interface structure follows the diamond cubic crystal structure across the interface and no interface states are present in the band gap as expected due to no dangling bonds being present at the interface. The GeSi misaligned interface reconstructs to a $(2 \times 1)$ structure with the presence of Ge-Ge and Si-Si dimers and alternating 5-fold and 7-fold rings in the mismatched regions to adjust the bonding at the interface. Interfaces states were present in the band gap, however only one of the states was unoccupied. This unoccupied state existed near the conduction band edge and this is the only state that is of concern in the development of a GeSi APD as it has the potential to create an electronic trap for the carriers.

Sulfur is an atom with flexible chemical bonds and we investigated if this flexibility would adjust the bonding in the interface regions where the germanium and silicon lattices align and misalign to provide an interface free of electronic states. Two very different structural geometries resulted with the use of sulfur at the interface. In both the aligned and misaligned interfaces, the electronic structure showed the existence of interface states. One of these states was unoccupied and this unoccupied state also existed in the GeSi misaligned interface without the presence of sulfur, thus sulfur does not improve the interface and the electronic trap still remains which may be an issue in the production of the GeSi APD.

From here we investigated the presence of using both sulfur and hydrogen at the interface as the presence of both species on the germanium surface removes surface states. The aligned and misaligned GeSHSi interfaces are almost identical to the aligned and misaligned GeSSi interfaces except for the hydrogen molecule being present in the channel between the dimer rows. Interfaces states existed in both interfaces with one of these states being unoccupied. Again this unoccupied state exists as before and thus the introduction of the hydrogen molecule with the hope of atomic hydrogen bonding with the unoccupied state did not occur in both the aligned and misaligned GeSHSi interfaces.

To conclude the original unoccupied interface state that existed in the GeSi misaligned interface remained throughout our calculations. Sulfur and hydrogen did not remove this potential electronic trap and this has the potential to be a problem in the development of the GeSi avalanche photodiode.

APPENDIX A

# Appendix

## A.1 Total Energies of Surfaces

Table A.1: Calculated supercell energies (eV) for $H_2S$ and $H_2O$-terminated Ge(001)-$(2 \times 1)$ surfaces. The calculated supercell energy for each surface with the desorbed molecule removed and the structure re-relaxed are also presented, along with the supercell energy for the relevant isolated molecule.

| | LDA | LDA vdW | GGA | GGA vdW |
|---|---|---|---|---|
| Fig 4.1(c) $H_2S$ removed | -2323.78 | -2354.81 | -2292.63 | -2316.95 |
| $H_2S$ molecule | -309.31 | -314.32 | -309.52 | -312.91 |
| Fig 4.1(c) $H_2S$ removed + $H_2S$ molecule | -2633.09 | -2669.13 | -2602.15 | -2629.86 |
| Fig 4.1(c) | -2633.13 | -2669.17 | -2602.03 | -2629.89 |
| Fig 4.1(d) $H_2$ removed | -2602.76 | -2636.76 | -2571.02 | -2597.53 |
| $H_2$ molecule | -30.64 | -32.76 | -31.39 | -32.75 |
| Fig 4.1(d) $H_2$ removed +$H_2$ molecule | -2633.40 | -2669.52 | -2602.41 | -2630.28 |
| Fig 4.1(d) | -2633.38 | -2669.47 | -2602.28 | -2630.20 |
| Fig 4.2(b) $H_2O$ removed | -2479.40 | -2513.75 | -2449.14 | -2475.73 |
| $H_2O$ molecule | -462.78 | -470.30 | -464.10 | -468.97 |
| Fig 4.2(b) $H_2O$ removed + $H_2O$ molecule | -2942.18 | -2984.05 | -2913.24 | -2944.70 |
| Fig 4.2(b) | -2942.36 | -2984.14 | -2913.31 | -2944.92 |
| Fig 4.2(c) $H_2$ removed | -2911.24 | -2951.12 | -2881.39 | -2911.71 |
| $H_2$ molecule | -30.94 | -33.13 | -31.72 | -33.13 |
| Fig 4.2(c) $H_2$ removed + $H_2$ molecule | -2942.18 | -2984.25 | -2913.11 | -2944.84 |
| Fig 4.2(c) | -2942.21 | -2984.24 | -2912.99 | -2944.85 |

## A.2 Vibrational Mode Frequencies

The vibrational mode frequencies of $H_2S$ on a Ge(001) surface for the relaxed structures Fig. 4.1(c) and Fig. 4.1(d) shown in Chapter 4 for LDA and GGA, with and without vdW are given in Table A.2.

Table A.2: Calculated vibrational mode frequencies (in $cm^{-1}$) for $H_2S$ on a Ge(001) surface for the relaxed structures shown in Fig. 4.1(c) and Fig. 4.1(d) and the isolated molecule using both LDA and GGA. Experimental frequencies for $H_2S$ molecule from Ref. [3] are also shown.

| | | H-S Stretch | H-S Bend | Ge-H Stretch | Ge-H Bend | Ge-S Stretch | H-S Wag |
|---|---|---|---|---|---|---|---|
| Fig. 4.1(c) | LDA | 2441 | 708 | 1945 | 533<br>503 | 350 | 393 |
| Fig. 4.1(c)<br>($H_2S$ removed) | LDA | 2501 | 703 | 1989 | 513<br>504 | 329 | 381 |
| Fig. 4.1(c) | LDA vdW | 2473 | 743 | 2032 | 544<br>529 | 331 | 374 |
| Fig. 4.1(c)<br>($H_2S$ removed) | LDA vdW | 2524 | 732 | 2010 | 550<br>547 | 308 | 351 |
| Fig. 4.1(c) | GGA | 2494 | 703 | 1946 | 503<br>487 | 342 | 392 |
| Fig. 4.1(c)<br>($H_2S$ removed) | GGA | 2540 | 693 | 1953 | 505<br>491 | 320 | 358 |
| Fig. 4.1(c) | GGA vdW | 2459 | 714 | 1952 | 517<br>477 | 317 | 376 |
| Fig. 4.1(c)<br>($H_2S$ removed) | GGA vdW | 2513 | 709 | 1935 | 519<br>502 | 325 | 338 |
| Fig. 4.1(d) | LDA | 2438<br>2419 | 718<br>706 | | | 396<br>374<br>361 | 328 |
| Fig. 4.1(d)<br>($H_2$ removed) | LDA | 2488<br>2414 | 709<br>693 | | | 394<br>373 | 336 |
| Fig. 4.1(d) | LDA vdW | 2492<br>2473 | 748<br>736 | | | 364<br>346 | 333 |
| Fig. 4.1(d)<br>($H_2$ removed) | LDA vdW | 2515<br>2498 | 735<br>729 | | | 365<br>349 | 287 |
| Fig. 4.1(d) | GGA | 2495<br>2484 | 708<br>704 | | | 373<br>353 | 337 |
| Fig. 4.1(d)<br>($H_2$ removed) | GGA | 2528<br>2518 | 695<br>694 | | | 374<br>356 | 287 |
| Fig. 4.1(d) | GGA vdW | 2481<br>2469 | 729<br>719 | | | 352<br>332 | 315 |
| Fig. 4.1(d)<br>($H_2$ removed) | GGA vdW | 2499<br>2487 | 721<br>711 | | | 352<br>342 | 273 |
| Molecule | LDA | 2562<br>2545 | 1117 | | | | |
| Molecule | LDA vdW | 2541<br>2524 | 1187 | | | | |
| Molecule | GGA | 2565<br>2547 | 1140 | | | | |
| Molecule | GGA vdW | 2525<br>2508 | 1179 | | | | |
| Molecule | Expt | 2733.4<br>2721.9 | 1214.5 | | | | |

Table A.3: Calculated LDA and GGA vibrational mode frequencies (in $cm^{-1}$) for $H_2O$ on a Ge(001) surface for the relaxed structures shown in Fig. 4.4(b) and Fig. 4.4(c) and for the isolated molecule. Experimental frequencies for $H_2O$ molecule from Ref. [3] are also shown.

| | | H-O Stretch | H-O Bend | Ge-H Stretch | Ge-H Bend | Ge-O Stretch | H-O Wag |
|---|---|---|---|---|---|---|---|
| Fig. 4.2(b) | LDA | 3590 | 921 | 1995 | 538<br>455 | 609 | 342 |
| Fig. 4.2(b) ($H_2O$ removed) | LDA | 3589 | 939 | 2004 | 511<br>505 | 653 | 304 |
| Fig. 4.2(b) | LDA vdW | 3583 | 947 | 2067 | 543<br>531 | 621 | |
| Fig. 4.2(b) ($H_2O$ removed) | LDA vdW | 3572 | 970 | 2024 | 554<br>552 | 648 | 330 |
| Fig. 4.2(b) | GGA | 3600 | 940 | 1991 | 486<br>469 | 559 | 336 |
| Fig. 4.2(b) ($H_2O$ removed) | GGA | 3592 | 956 | 1965 | 500<br>492 | 587 | 313 |
| Fig. 4.2(b) | GGA vdW | 3552 | 951 | 2000 | 504<br>483 | 579<br>538 | 401 |
| Fig. 4.2(b) ($H_2O$ removed) | GGA vdW | 3550 | 961 | 1951 | 516<br>503 | 573 | 328 |
| Fig. 4.2(c) | LDA | 3593<br>3498 | 984<br>909 | | | 677<br>654 | 381 |
| Fig. 4.2(c) ($H_2$ removed) | LDA | 3583<br>3580 | 949<br>932 | | | 676<br>645 | 349 |
| Fig. 4.2(c) | LDA vdW | 3557<br>3555 | 972<br>937 | | | 652<br>612 | 347 |
| Fig. 4.2(c) ($H_2$ removed) | LDA vdW | 3575<br>3566 | 969<br>925 | | | 646<br>613 | 351 |
| Fig. 4.2(c) | GGA | 3577<br>3575 | 969<br>942 | | | 621<br>586 | 340 |
| Fig. 4.2(c) ($H_2$ removed) | GGA | 3611<br>3595 | 955<br>922 | | | 614<br>574 | 337 |
| Fig. 4.2(c) | GGA vdW | 3548<br>3524 | 970<br>942 | | | 587<br>537 | 362 |
| Fig. 4.2(c) ($H_2$ removed) | GGA vdW | 3550<br>3540 | 961<br>929 | | | 606<br>568 | 360 |
| Molecule | LDA | 3713<br>3602 | 1581 | | | | |
| Molecule | LDA vdW | 3677<br>3573 | 1635 | | | | |
| Molecule | GGA | 3709<br>3602 | 1624 | | | | |
| Molecule | GGA vdW | 3624<br>3584 | 1591 | | | | |
| Molecule | Expt | 3942.5<br>3833.2 | 1648.5 | | | | |

# Bibliography


[1] "Covalent radii calculated from the website." http://www.periodictable.com/Properties/A/CovalentRadius.html, 2013. xix, 39, 49

[2] R. Rossmann, H. L. Meyerheim, V. Jahns, J. Wever, W. Moritz, D. Wolf, D. Dornisch, and H. Schulz, "The Ge (001)(2× 1) reconstruction: Asymmetric dimers and multilayer relaxation observed by grazing incidence x-ray diffraction," *Surface Science*, vol. 279, no. 1-2, pp. 199–209, 1992. xix, 39, 49

[3] D. A. Clabo, W. D. Allen, R. B. Remington, Y. Yamaguchi, and H. F. Schaefer, "A systematic study of molecular vibrational anharmonicity and vibrationârotation interaction by self-consistent-field higher-derivative methods. asymmetric top molecules," *Chemical Physics*, vol. 123, no. 2, pp. 187–239, 1988. xix, xxi, 43, 45, 51, 125, 126

[4] B. E. A. Saleh and M. C. Teich, *Fundamentals of Photonics*. John Wiley and Sons, 2007. 1

[5] S. M. Sze and K. K. Ng, *Physics of semiconductor devices*. Wiley, 2007. 2

[6] M. A. Othman, S. N. Taib, M. N. Husain, and Z. A. F. M. Napiah, "Reviews on avalanche photodiode for optical communication technology," *APRN Journal of Engineering and Applied Sciences*, vol. 9, no. 1, 2014. 2

[7] "Avalanche photodiodes theory and applications." http://www.photonicsonline.com/doc/avalanche-photodiodes-theory-and-applications-0001, 2013. 2

[8] M. J. N. Sibley, *Optical Communications*. The Macmillan Press Ltd, 1995. 2

[9] Y. Kang, H.-D. Liu, M. Morse, M. J. Paniccia, M. Zadka, S. Litski, G. Sarid, A. Pauchard, Y.-H. Kuo, H.-W. Chen, *et al.*, "Monolithic germanium/silicon avalanche photodiodes with 340 Ghz gain–bandwidth product," *Nature Photonics*, vol. 3, no. 1, pp. 59–63, 2009. 2, 3

[10] S. Assefa, F. Xia, and Y. A. Vlasov, "Reinventing germanium avalanche photodetector for nanophotonic on-chip optical interconnects," *Nature*, vol. 464, no. 7285, pp. 80–84, 2010. 2

[11] F. Emami and M. F. Tehrani, "Noise in avalanche photodiodes," in *WSEAS International Conference. Proceedings. Mathematics and Computers in Science and Engineering*, no. 12, World Scientific and Engineering Academy and Society, 2008. 2

[12] D. Dai, H.-W. Chen, J. E. Bowers, Y. Kang, M. Morse, and M. J. Paniccia, "Equivalent circuit model of a Ge/Si avalanche photodiode," in *The 6th International Conference on Group IV Photonics, San Francisco, California*, pp. 9–11, 2009. 3

[13] X. Wang, L. Chen, W. Chen, H. Cui, Y. Hu, P. Cai, R. Yang, C.-Y. Hong, D. Pan, K.-W. Ang, *et al.*, "80 GHz bandwidth-gain-product Ge/Si avalanche photodetector by selective Ge growth," in *Optical Fiber Communication Conference*, p. OMR3, Optical Society of America, 2009. 3

[14] N. Duan, T.-Y. Liow, A. E.-J. Lim, L. Ding, and G. Q. Lo, "310 GHz gain-bandwidth product Ge/Si avalanche photodetector for 1550 nm light detection," *Opt. Express*, vol. 20, no. 10, pp. 11031–11036, 2012. 3

[15] M. Bruel, "Silicon on insulator material technology," *Electronics letters*, vol. 31, no. 14, pp. 1201–1202, 1995. 3

[16] H. Kanbe, M. Miyaji, and T. Ito, "Ge/Si heterojunction photodiodes fabricated by low temperature wafer bonding," *Applied physics express*, vol. 1, no. 7, p. 072301, 2008. 3

[17] F. Gity, J. M. Hayes, B. Corbett, and A. P. Morrison, "Modeling the effects of interface traps on the static and dynamic characteristics of Ge/Si avalanche photodiodes," *Quantum Electronics, IEEE Journal of*, vol. 47, no. 6, pp. 849–857, 2011. 3

[18] F. Gity, K. Y. Byun, K.-H. Lee, K. Cherkaoui, J. M. Hayes, A. P. Morrison, C. Colinge, and B. Corbett, "Characterization of germanium/silicon p–n junction fabricated by low temperature direct wafer bonding and layer exfoliation," *Applied Physics Letters*, vol. 100, no. 9, p. 092102, 2012. 3

[19] F. Gity, A. Daly, B. Snyder, F. H. Peters, J. Hayes, C. Colinge, A. P. Morrison, and B. Corbett, "Ge/Si heterojunction photodiodes fabricated by low temperature wafer bonding," *Optics Express*, vol. 21, no. 14, pp. 17309–17314, 2013. 3

[20] P. W. Loscutoff and S. F. Bent, "Reactivity of the germanium surface: Chemical passivation and functionalization," *Annu. Rev. Phys. Chem.*, vol. 57, pp. 467–495, 2006. 3, 4, 34

[21] C. B. Duke, "Semiconductor surface reconstruction: The structural chemistry of two-dimensional surface compounds," *Chemical Reviews*, vol. 96, no. 4, pp. 1237–1260, 1996. 3

[22] M. Houssa, D. Nelis, D. Hellin, G. Pourtois, T. Conard, K. Paredis, K. Vanormelingen, A. Vantomme, M. Van Bael, J. Mullens, *et al.*, "H2S exposure of a (100) Ge surface: Evidences for a (2$\times$ 1) electrically passivated

surface," *Applied Physics Letters*, vol. 90, no. 22, p. 222105, 2007. 4, 5, 35, 37, 86, 103

[23] Y. Chabal, "Infrared spectroscopy of hydrogen on silicon surfaces," *Physica B: Condensed Matter*, vol. 170, no. 1, pp. 447–456, 1991. 4, 35

[24] K. Kita, K. Kyuno, and A. Toriumi, "Growth mechanism difference of sputtered HfO 2 on Ge and on Si," *Applied Physics Letters*, vol. 85, no. 1, 2004. 5

[25] H. Kim, P. C. McIntyre, C. O. Chui, K. C. Saraswat, and M.-H. Cho, "Interfacial characteristics of HfO2 grown on nitrided Ge (100) substrates by atomic-layer deposition," *Applied Physics Letters*, vol. 85, p. 2902, 2004. 5

[26] A. Dimoulas, G. Mavrou, G. Vellianitis, E. Evangelou, N. Boukos, M. Houssa, and M. Caymax, "HfO2 high-kappa gate dielectrics on Ge (100) by atomic oxygen beam deposition," *Applied Physics Letters*, vol. 86, no. 3, 2005. 5

[27] M. Rohlfing, P. Krüger, and J. Pollmann, "Quasiparticle band structures of clean, hydrogen-, and sulfur-terminated Ge (001) surfaces," *Physical Review B*, vol. 54, no. 19, p. 13759, 1996. 5, 28, 29, 31, 32, 34, 35, 37, 86, 87, 93, 100, 110, 116

[28] M. Born and R. Oppenheimer, "Zur quantentheorie der molekeln," *Annalen der Physik*, vol. 389, no. 20, pp. 457–484, 1927. 9

[29] R. M. Martin, *Electronic structure: basic theory and practical methods*. Cambridge university press, 2004. 10, 12, 14, 36, 57

[30] P. Hohenberg and W. Kohn, "Inhomogeneous electron gas," *Physical Review*, vol. 136, no. 3B, p. B864, 1964. 11

[31] M. Levy, "Universal variational functionals of electron densities, first-order density matrices, and natural spin-orbitals and solution of the v-representability problem," *Proceedings of the National Academy of Sciences*, vol. 76, no. 12, pp. 6062–6065, 1979. 11

[32] M. Levy, "Electron densities in search of hamiltonians," *Physical Review A*, vol. 26, no. 3, p. 1200, 1982. 11

[33] M. Levy and J. P. Perdew, "The constrained search formulation of density functional theory," in *Density functional methods in physics*, pp. 11–30, Springer, 1985. 11

[34] E. H. Lieb, A. Shimony, and H. Feshbach, "Physics as natural philosophy," *Essays in Honor of Laszlo Tisza, MIT Press, Cambridge*, p. 111, 1982. 11

[35] E. H. Lieb, "Density functionals for coulomb systems," in *Inequalities*, pp. 269–303, Springer, 2002. 11

[36] E. H. Lieb, "Density functionals for coulomb systems," in *Density Functional Methods in Physics*, pp. 31–80, Springer, 1985. 11

[37] W. Kohn and L. J. Sham, "Self-consistent equations including exchange and correlation effects," *Physical Review*, vol. 140, no. 4A, p. A1133, 1965. 12

[38] D. M. Ceperley and B. Alder, "Ground state of the electron gas by a stochastic method," *Physical Review Letters*, vol. 45, no. 7, p. 566, 1980. 15

[39] J. P. Perdew and Y. Wang, "Accurate and simple analytic representation of the electron-gas correlation energy," *Physical Review B*, vol. 45, no. 23, p. 13244, 1992. 15, 20, 30, 36, 42

[40] R. P. Feynman, "Forces in molecules," *Physical Review*, vol. 56, no. 4, p. 340, 1939. 15, 30, 36

[41] H. J. Monkhorst and J. D. Pack, "Special points for Brillouin-zone integrations," *Physical Review B*, vol. 13, no. 12, p. 5188, 1976. 17, 30, 37, 57, 87

[42] C. Hartwigsen, S. Gœdecker, and J. Hutter, "Relativistic separable dual-space gaussian pseudopotentials from H to Rn," *Physical Review B*, vol. 58, no. 7, p. 3641, 1998. 19, 30, 42, 57

[43] N. Troullier and J. L. Martins, "Efficient pseudopotentials for plane-wave calculations," *Physical Review B*, vol. 43, no. 3, p. 1993, 1991. 19, 30, 36, 42, 57

[44] J. P. Perdew, K. Burke, and M. Ernzerhof, "Generalized gradient approximation made simple," *Physical Review Letters*, vol. 77, no. 18, p. 3865, 1996. 20, 36

[45] V. N. Staroverov, G. E. Scuseria, J. Tao, and J. P. Perdew, "Comparative assessment of a new nonempirical density functional: Molecules and hydrogen-bonded complexes," *The Journal of Chemical Physics*, vol. 119, no. 23, pp. 12129–12137, 2003. 21

[46] V. N. Staroverov, G. E. Scuseria, J. Tao, and J. P. Perdew, "Tests of a ladder of density functionals for bulk solids and surfaces," *Physical Review B*, vol. 69, no. 7, p. 075102, 2004. 21

[47] Y. Andersson, E. Hult, H. Rydberg, P. Apell, B. I. Lundqvist, and D. C. Langreth, "Van der waals interactions in density functional theory," in *Electronic Density Functional Theory*, pp. 243–260, Springer, 1998. 21

[48] J. F. Dobson and B. P. Dinte, "Constraint satisfaction in local and gradient susceptibility approximations: Application to a van der waals density functional," *Physical Review Letters*, vol. 76, no. 11, p. 1780, 1996. 21

[49] W. Kohn, Y. Meir, and D. E. Makarov, "van der waals energies in density functional theory," *Physical Review Letters*, vol. 80, no. 19, p. 4153, 1998. 21

[50] M. Dion, H. Rydberg, E. Schröder, D. C. Langreth, and B. I. Lundqvist, "Van der waals density functional for general geometries," *Physical Review Letters*, vol. 92, no. 24, p. 246401, 2004. 21, 38

[51] T. Thonhauser, V. R. Cooper, S. Li, A. Puzder, P. Hyldgaard, and D. C. Langreth, "Van der waals density functional: Self-consistent potential and the nature of the van der waals bond," *Physical Review B*, vol. 76, no. 12, p. 125112, 2007. 21

[52] D. C. Langreth and B. I. Lundqvist, "Comment on Nonlocal Van Der Waals Density Functional Made Simple," *Physical Review Letters*, vol. 104, no. 9, p. 099303, 2010. 21

[53] O. A. Vydrov and T. Van Voorhis, "Vydrov and van voorhis reply," *Physical Review Letters*, vol. 104, no. 9, p. 099304, 2010. 21

[54] H. Rydberg, M. Dion, N. Jacobson, E. Schröder, P. Hyldgaard, S. Simak, D. C. Langreth, and B. I. Lundqvist, "Van der waals density functional for layered structures," *Physical Review Letters*, vol. 91, no. 12, p. 126402, 2003. 21

[55] D. Langreth, B. I. Lundqvist, S. D. Chakarova-Käck, V. Cooper, M. Dion, P. Hyldgaard, A. Kelkkanen, J. Kleis, L. Kong, S. Li, *et al.*, "A density functional for sparse matter," *Journal of Physics: Condensed Matter*, vol. 21, no. 8, p. 084203, 2009. 21

[56] A. Gulans, M. J. Puska, and R. M. Nieminen, "Linear-scaling self-consistent implementation of the van der waals density functional," *Physical Review B*, vol. 79, no. 20, p. 201105, 2009. 21

[57] A. K. Kelkkanen, B. I. Lundqvist, and J. K. Nørskov, "Density functional for van der waals forces accounts for hydrogen bond in benchmark set of water hexamers," *The Journal of Chemical Physics*, vol. 131, no. 4, p. 046102, 2009. 21

[58] K. Lee, É. D. Murray, L. Kong, B. I. Lundqvist, and D. C. Langreth, "Higher-accuracy van der waals density functional," *Physical Review B*, vol. 82, no. 8, p. 081101, 2010. 21, 22, 38

[59] J. P. Perdew and W. Yue, "Accurate and simple density functional for the electronic exchange energy: Generalized gradient approximation," *Physical Review B*, vol. 33, no. 12, p. 8800, 1986. 21

[60] É. D. Murray, K. Lee, and D. C. Langreth, "Investigation of exchange energy density functional accuracy for interacting molecules," *Journal of Chemical Theory and Computation*, vol. 5, no. 10, pp. 2754–2762, 2009. 21

[61] A. Maradudin, *Theory of lattice dynamics in the harmonic approximation*. Solid state physics: Supplement, Academic Press, 1971. 22

[62] S. D. Kevan and N. G. Stoffel, "Metal-insulator transition on the Ge (001) surface," *Physical Review Letters*, vol. 53, no. 7, p. 702, 1984. 28

[63] S. D. Kevan, "Surface states and reconstruction on Ge (001)," *Physical Review B*, vol. 32, no. 4, p. 2344, 1985. 28

[64] P. Krüger, A. Mazur, J. Pollmann, and G. Wolfgarten, "First-principles electronic structure theory for semi-infinite semiconductors with applications to Ge (001)(2× 1) and Si (001)(2× 1)," *Physical Review Letters*, vol. 57, no. 12, p. 1468, 1986. 28

[65] J. Pollmann, P. Krüger, and A. Mazur, "Self-consistent electronic structure of semi-infinite Si (001)(2× 1) and Ge (001)(2× 1) with model calculations for scanning tunneling microscopy," *Journal of Vacuum Science & Technology B*, vol. 5, no. 4, pp. 945–952, 1987. 28

[66] M. Needels, M. Payne, and J. Joannopoulos, "High-order reconstructions of the Ge (100) surface," *Physical Review B*, vol. 38, no. 8, p. 5543, 1988. 28

[67] P. Krüger and J. Pollmann, "Theory of adsorption: Ordered monolayers from Na to Cl on Si (001) and Ge (001)," *Applied Physics A Solids and Surfaces*, vol. 59, no. 5, pp. 487–502, 1994. 28

[68] R. E. Schlier and H. E. Farnsworth, "Structure and adsorption characteristics of clean surfaces of germanium and silicon," *The Journal of Chemical Physics*, vol. 30, no. 4, pp. 917–926, 1959. 29

[69] J. D. Levine, "Structural and electronic model of negative electron affinity on the Si/Cs/O surface," *Surface Science*, vol. 34, no. 1, pp. 90–107, 1973. 29

[70] D. J. Chadi, "Atomic and electronic structures of reconstructed Si (100) surfaces," *Physical Review Letters*, vol. 43, no. 1, p. 43, 1979. 29

[71] D. J. Chadi, "Si (100) surfaces: Atomic and electronic structures," *Journal of Vacuum Science & Technology*, vol. 16, no. 5, pp. 1290–1296, 1979. 29

[72] D. J. Chadi, "Reexamination of the Si (100) surface reconstruction," *Applied Optics*, vol. 19, no. 23, pp. 3971–3973, 1980. 29

[73] J. A. Kubby, J. E. Griffith, R. S. Becker, and J. S. Vickers, "Tunneling microscopy of Ge (001)," *Physical Review B*, vol. 36, no. 11, p. 6079, 1987. 29

[74] R. J. Culbertson, Y. Kuk, and L. C. Feldman, "Subsurface strain in the Ge (001) and Ge (111) surfaces and comparison to silicon," *Surface Science*, vol. 167, no. 1, pp. 127–140, 1986. 29

[75] C. A. Lucas, C. S. Dower, D. F. McMorrow, G. C. L. Wong, F. J. Lamelas, and P. H. Fuoss, "Order-disorder c (4× 2)-(2× 1) transition on Ge (001): An in situ x-ray scattering study," *Physical Review B*, vol. 47, no. 16, p. 10375, 1993. 29

[76] L. Spiess, A. J. Freeman, and P. Soukiassian, "Ge (100) 2× 1 and c (4× 2) surface reconstructions studied by ab initio total-energy molecular-force calculations," *Physical Review B*, vol. 50, no. 4, p. 2249, 1994. 29

[77] P. Krüger and J. Pollmann, "Dimer reconstruction of diamond, Si, and Ge (001) surfaces," *Physical Review Letters*, vol. 74, no. 7, p. 1155, 1995. 29, 31

[78] E. Landemark, R. I. G. Uhrberg, P. Krüger, and J. Pollmann, "Surface electronic structure of Ge(001)-(2× 1): experiment and theory," *Surface Science*, vol. 236, no. 3, pp. L359–L364, 1990. 29

[79] L. Kipp, R. Manzke, and M. Skibowski, "The surface band gaps of Ge (001) 2× 1," *Surface Science*, vol. 269, pp. 854–859, 1992. 29

[80] E. Landemark, C. J. Karlsson, L. S. O. Johansson, and R. I. G. Uhrberg, "Electronic structure of clean and hydrogen-chemisorbed Ge (001) surfaces studied by photoelectron spectroscopy," *Physical Review B*, vol. 49, no. 23, p. 16523, 1994. 29

[81] W. R. Lambert, P. L. Trevor, M. J. Cardillo, A. Sakai, and D. R. Hamann, "Surface structure of Ge (100) studied by he diffraction," *Physical Review B*, vol. 35, no. 15, p. 8055, 1987. 29

[82] L. Kipp, R. Manzke, and M. Skibowski, "An intrinsic metallic surface state on Ge (001) 2× 1," *Solid State Communications*, vol. 93, no. 7, pp. 603–607, 1995. 29

[83] H. Zandvliet, A. van Silfhout, and M. Sparnaay, "Metallic properties of the ge (001) surface," *Physical Review B*, vol. 39, no. 8, p. 5576, 1989. 29

[84] M. S. Hybertsen and S. G. Louie, "Many-body calculation of surface states: As on Ge (111)," *Physical Review Letters*, vol. 58, no. 15, p. 1551, 1987. 30

[85] X. Gonze, B. Amadon, P.-M. Anglade, J.-M. Beuken, F. Bottin, P. Boulanger, F. Bruneval, D. Caliste, R. Caracas, M. Cote, *et al.*, "Abinit: First-principles approach to material and nanosystem properties," *Computer Physics Communications*, vol. 180, no. 12, pp. 2582–2615, 2009. 30, 42, 57

[86] H. B. Schlegel, "Optimization of equilibrium geometries and transition structures," *Journal of Computational Chemistry*, vol. 3, no. 2, pp. 214–218, 1982. 30, 37, 58

[87] S. Kasap and P. Capper, *Springer handbook of electronic and photonic materials*. Springer Science & Business Media, 2007. 31

[88] J. S. Lee, T. Kaufman-Osborn, W. Melitz, S. Lee, and A. Kummel, "Effect of H2O chemisorption on passivation of Ge (100) surface studied by scanning tunneling microscopy," *Surface Science*, vol. 605, no. 15, pp. 1583–1588, 2011. 34, 35

[89] S. J. Jung, J. Y. Lee, S. Hong, and S. Kim, "Study of adsorption and decomposition of H2O on Ge (100)," *The Journal of Physical Chemistry B*, vol. 109, no. 51, pp. 24445–24449, 2005. 35, 49

[90] V. A. Parsegian, *Van der Waals forces: a handbook for biologists, chemists, engineers, and physicists*. Cambridge University Press, 2005. 35

[91] P. Giannozzi, S. Baroni, N. Bonini, M. Calandra, R. Car, C. Cavazzoni, D. Ceresoli, G. L. Chiarotti, M. Cococcioni, I. Dabo, A. Dal Corso, S. de Gironcoli, S. Fabris, G. Fratesi, R. Gebauer, U. Gerstmann, C. Gougoussis, A. Kokalj, M. Lazzeri, L. Martin-Samos, N. Marzari, F. Mauri, R. Mazzarello, S. Paolini, A. Pasquarello, L. Paulatto, C. Sbraccia, S. Scandolo, G. Sclauzero, A. P. Seitsonen, A. Smogunov, P. Umari, and R. M. Wentzcovitch, "Quantum espresso: a modular and open-source software project for quantum simulations of materials." `http://www.quantum-espresso.org`, 2009. 36

[92] J. Kohanoff, *Electronic structure calculations for solids and molecules: theory and computational methods*. Cambridge University Press, 2006. 36

[93] M. Fuchs and M. Scheffler, "Ab initio pseudopotentials for electronic structure calculations of poly-atomic systems using density-functional theory," *Computer Physics Communications*, vol. 119, no. 1, pp. 67–98, 1999. 36

[94] L. B. Lewis, J. Segall, and K. C. Janda, "Recombinative desorption of hydrogen from the Ge (100)–(2$\times$ 1) surface: A laser-induced desorption study," *The Journal of Chemical Physics*, vol. 102, no. 18, pp. 7222–7228, 1995. 37

[95] A. Teweldeberhan and S. Fahy, "Calculated pressure dependence of the localized vibrational mode of nitrogen in GaN x As 1- x," *Physical Review B*, vol. 72, no. 19, p. 195203, 2005. 42

[96] G. Nilsson and G. Nelin, "Study of the homology between silicon and germanium by thermal-neutron spectrometry," *Physical Review B*, vol. 6, no. 10, p. 3777, 1972. 47

[97] C. Mui, J. P. Senosiain, and C. B. Musgrave, "Initial oxidation and hydroxylation of the Ge (100)-2× 1 surface by water and hydrogen peroxide," *Langmuir*, vol. 20, no. 18, pp. 7604–7609, 2004. 49

[98] A. Föraker and D. J. Doren, "Dissociative adsorption of water on Ge (100)-(2× 1): First-principles theory," *The Journal of Physical Chemistry B*, vol. 107, no. 33, pp. 8507–8510, 2003. 49

[99] J.-H. Cho, L. Kleinman, K.-j. Jin, and K. S. Kim, "Theoretical study of water adsorption on the Ge (100) surface," *Physical Review B*, vol. 66, no. 11, p. 113306, 2002. 49

[100] C. Larsson and A. Flodström, "H2O adsorption on Ge (100): An angle-resolved photoelectron spectroscopy study," *Physical Review B*, vol. 43, no. 11, p. 9281, 1991. 49

[101] S. Goedecker, M. Teter, and J. Hutter, "Separable dual-space gaussian pseudopotentials," *Physical Review B*, vol. 54, no. 3, p. 1703, 1996. 57

[102] C. G. Van de Walle and R. M. Martin, "Theoretical calculations of heterojunction discontinuities in the Si/Ge system," *Physical Review B*, vol. 34, no. 8, p. 5621, 1986. 59

[103] K. Leung, L. Terminello, Z. Hussain, X. Zhang, T. Hayashi, and D. Shirley, "Surface-bonding geometry of (2× 1) S/Ge (001) by the normal-emission angle-resolved photoemission extended-fine-structure technique," *Physical Review B*, vol. 38, no. 12, p. 8241, 1988. 86

[104] K. Newstead, A. Robinson, S. d'Addato, A. Patchett, N. Prince, R. McGrath, R. Whittle, E. Dudzik, and I. McGovern, "An x-ray absorption fine structure study of Ge (001)(2× 1)-S," *Surface Science*, vol. 287, pp. 317–320, 1993. 86

[105] T. Weser, A. Bogen, B. Konrad, R. Schnell, C. Schug, and W. Steinmann, "Photoemission surface core-level study of sulfur adsorption on Ge (100)," *Physical Review B*, vol. 35, no. 15, p. 8184, 1987. 86

[106] T. Weser, A. Bogen, B. Konrad, R. Schnell, C. Schug, W. Moritz, and W. Steinmann, "Chemisorption of sulfur on ge (100)," *Surface Science*, vol. 201, no. 1-2, pp. 245–256, 1988. 86

[107] G. Anderson, M. Hanf, P. Norton, Z. Lu, and M. Graham, "The s-passivation of ge (100)-(1$\times$ 1)," *Applied Physics Letters*, vol. 66, no. 9, pp. 1123–1125, 1995. 86